



## 저작자표시-비영리-변경금지 2.0 대한민국

이용자는 아래의 조건을 따르는 경우에 한하여 자유롭게

- 이 저작물을 복제, 배포, 전송, 전시, 공연 및 방송할 수 있습니다.

다음과 같은 조건을 따라야 합니다:



저작자표시. 귀하는 원저작자를 표시하여야 합니다.



비영리. 귀하는 이 저작물을 영리 목적으로 이용할 수 없습니다.



변경금지. 귀하는 이 저작물을 개작, 변형 또는 가공할 수 없습니다.

- 귀하는, 이 저작물의 재이용이나 배포의 경우, 이 저작물에 적용된 이용허락조건을 명확하게 나타내어야 합니다.
- 저작권자로부터 별도의 허가를 받으면 이러한 조건들은 적용되지 않습니다.

저작권법에 따른 이용자의 권리는 위의 내용에 의하여 영향을 받지 않습니다.

이것은 [이용허락규약\(Legal Code\)](#)을 이해하기 쉽게 요약한 것입니다.

[Disclaimer](#)

Ph.D. Dissertation of Biomedical Sciences

**Mechanistic Understanding and  
Biochemical Modulation of the N-  
Degron Pathway in Selective Autophagy  
against Intracellular Bacteria**

N-데그론 경로가 세포 내 세균에 대한  
선택적 자가포식에서 작용하는  
기전 및 생화학적 조절

August 2022

Department of Biomedical Sciences  
Seoul National University  
College of Medicine

Biomedical Sciences Major

Yoon Jee Lee

의학박사 학위논문

**Mechanistic Understanding and  
Biochemical Modulation of the N-  
Degron Pathway in Selective Autophagy  
against Intracellular Bacteria**

N-데그론 경로가 세포 내 세균에 대한  
선택적 자가포식에서 작용하는  
기전 및 생화학적 조절

2022 년 8 월

서울대학교 대학원  
의과학과 의과학 전공

이 윤 지

N-데그론 경로가 세포 내 세균에 대한  
선택적 자가포식에서 작용하는  
기전 및 생화학적 조절

지도 교수 권 용 태

이 논문을 의학박사 학위논문으로 제출함

2022 년 4 월

서울대학교 대학원

의과학과 의과학 전공

이 윤 지

이윤지의 의학박사 학위논문을 인준함

2022 년 7 월

위 원 장 이 민 재 (인)

부위원장 권 용 태 (인)

위 원 한 도 현 (인)

위 원 염 진 기 (인)

위 원 조 은 경 (인)



# Mechanistic Understanding and Biochemical Modulation of the N-Degron Pathway in Selective Autophagy against Intracellular Bacteria

Advisor Yong Tae Kwon

Submitting a Ph.D. Dissertation of Biomedical Sciences

April 2022

Seoul National University College of Medicine  
Biomedical Sciences Major

Yoon Jee Lee

Confirming the Ph.D. Dissertation written by

Yoon Jee Lee

July 2022

Chair Min Jae Lee (Seal)

Vice Chair Yong Tae Kwon (Seal)

Examiner Dohyun Han (Seal)

Examiner Jinki Yeom (Seal)

Examiner Eun-Kyeong Jo (Seal)

## **Abstract**

# **Mechanistic Understanding and Biochemical Modulation of the N-Degron Pathway in Selective Autophagy against Intracellular Bacteria**

Yoon Jee Lee

Major in Biomedical Sciences

Department of Biomedical Sciences

Seoul National University College of Medicine

Macroautophagy (hereafter autophagy) is the intracellular host defense system that responds to various stresses. Upon bacterial infection, cells recognize bacteria via pathogen-associated molecular patterns (PAMPs) by receptor proteins which initiate appropriate signaling cascades that activate selective autophagy against bacteria. A subpopulation of intracellular bacteria use their unique strategies to manipulate host mechanisms to escape the autophagic degradation pathway. Despite extensive previous studies, the specific mechanism of how bacteria evade autophagy and molecules having an antibacterial effect by regulating selective autophagy against

intracellular bacteria has not been fully investigated.

In this thesis, I show counteractive crosstalk between intracellular bacteria and host autophagy, and the biochemical modulation of the Arg/N-degron pathway in selective autophagy upon bacterial infection. During the counteractive crosstalk, the expression level of autophagy receptors including p62/SQSTM1 (Sequestosome 1) and Optineurin increased and the autophagy receptors associated with *S. Typhimurium* and targeted to autophagosomes. Chemical mimetics of the Nt-Arg that bind to the ZZ domain of p62 were utilized as a host-directed therapeutic to promote autophagic degradation of intracellular bacteria. The p62 ligand activated p62 to facilitate the biogenesis of autophagosomes that were exploited and suppressed by intracellular *S. Typhimurium*. Furthermore, the p62 ligands exhibited antimicrobial effect against intracellular bacteria such as *Salmonella enterica* serovar Typhimurium, *Escherichia coli*, and *Streptococcus pyogenes* as well as *Mycobacterium tuberculosis* (Mtb) via selective autophagy that is independent of the mTOR-mediated autophagy pathway. Consistently, in mice, these chemicals exhibited antimicrobial efficacy against *S. Typhimurium*, Bacillus Calmette–Guérin (BCG), and Mtb as well as multidrug-resistant Mtb and inhibited the production of inflammatory cytokines. This dual mode of action in xenophagy and inflammation significantly protected mice from inflammatory lesions in the lungs and other tissues caused by all the tested bacterial strains. Therefore, this study suggests that the Arg/N-degron pathway plays a pivotal role in the innate immune response against various bacteria via p62-mediated xenophagy, and this mechanism provides a novel therapeutic target for infectious diseases caused by a broad range of pathogens including multidrug-resistant bacteria.

\* This study was published in “Chemical modulation of SQSTM1/p62-mediated xenophagy that targets a broad range of pathogenic bacteria. *Autophagy*, 2022.”

---

**Keywords:** Arg/N-degron pathway, host-directed therapy, inflammation, innate immune response, selective autophagy, *S. Typhimurium*, *M. tuberculosis*, xenophagy.

**Student number:** 2014-21995

# Contents

<b>Abstract .....</b>	<b>i</b>
<b>Contents.....</b>	<b>iv</b>
<b>List of figures.....</b>	<b>xi</b>
<b>List of Abbreviations.....</b>	<b>xvi</b>
<b>Introduction .....</b>	<b>1</b>
<b>Material and Methods.....</b>	<b>16</b>
Plasmids and reagents .....	16
Antibodies .....	16
Cell culture .....	17
Mice .....	18
Bacterial strains and culture .....	19
Bacterial infection.....	20
Mouse <i>Sqstm1</i> lentiviral short hairpin RNA (shRNA) production and transduction .....	21
Generation of a tandem LC3B (mCherry-EGFP-LC3B) retroviral vector .....	21
RNA extraction and qRT-PCR analysis.....	21
Chemical synthesis and analytical data of p62 ligands .....	23

Immunofluorescence analysis.....	33
Colony-forming unit (CFU) assay .....	34
RNA interference assay .....	35
Immunoblotting analysis .....	35
Molecular docking studies.....	36
Affinity-isolation assays of YT-6-2.....	37
Transmission electron microscopy (TEM) .....	38
Histology .....	38
Immunocytochemistry.....	39
Flow cytometry.....	39
MTT assay.....	40
Quantification and statistical analysis .....	40
<b>Results .....</b>	<b>41</b>
Counteractive crosstalk between <i>S. Typhimurium</i> and host cells via autophagy .....	41
Development of small molecule agonists that exert antimicrobial efficacy ....	42
p62 agonists rescue autophagic activities from suppression by <i>S. Typhimurium</i> .....	44
p62 agonists exert antimicrobial efficacy by binding to the ZZ domain of p62 .....	45
p62 agonists induce xenophagy of <i>S. Typhimurium</i> by facilitating the target of the pathogens to the autophagosome.....	48
p62 agonists enhance host innate immunity against Mtb and other pathogens via	

p62-mediated xenophagy .....	49
p62 agonists enhance xenophagy mediated host defense against pathogens in mice.....	50
The p62 agonists inhibit the production of proinflammatory mediators <i>in vitro</i> and <i>in vivo</i> . ....	52
<b>Discussion .....</b>	<b>128</b>
<b>References .....</b>	<b>134</b>
<b>Abstract in Korean.....</b>	<b>144</b>

# List of figures

Figure 1. Two major mechanisms regulate the degradation of intracellular proteins: the ubiquitin-proteasome system (UPS) and the autophagy-lysosomal pathway (ALP). .....	11
Figure 2. A schematic diagram of autophagy-lysosome pathway .....	12
Figure 3. A schematic diagram of the mammalian N-degron pathway in the UPS and autophagy.....	14
Figure 4. <i>S. Typhimurium</i> infection decreases protein level of LC3B of host cell MOI and time-dependently .....	54
Figure 5. Lipopolysaccharide (LPS) activates host cell autophagy.....	56
Figure 6. <i>S. Typhimurium</i> infection decreases LC3B protein level and autophagic flux.....	57
Figure 7. Autophagy-related genes are upregulated by <i>S. Typhimurium</i> infection .....	58
Figure 8. Intracellular <i>S. Typhimurium</i> is associated with p62 and LC3B .....	59
Figure 9. autophagy receptors are associated with intracellular <i>S. Typhimurium</i>	60
Figure 10. p62 is required for growth inhibition of intracellular <i>S.</i> <i>Typhimurium</i> .....	61
Figure 11. autophagosome biogenesis is required for growth inhibition of intracellular <i>S. Typhimurium</i> .....	62



Figure 12. Increase in the p62 and Optineurin protein level upon <i>S. Typhimurium</i> infection .....	63
Figure 13. Relative fold change in mRNA level of autophagy receptors in uninfected and <i>S. Typhimurium</i> -infected HeLa cells.....	64
Figure 14. Structure of five p62 ligands that show antimicrobial efficacy against intracellular <i>S. Typhimurium</i> .....	65
Figure 15. Concentration, time, and MOI dependent antimicrobial effect against intracellular <i>S. Typhimurium</i> by p62 ligand.....	67
Figure 16. Antimicrobial effect of p62 ligand against intracellular <i>S. Typhimurium</i> in various macrophage cell lines.....	69
Figure 17. Antimicrobial effect against intracellular <i>S. Typhimurium</i> by p62 ligand in various epithelial cell lines .....	70
Figure 18. p62 agonists do not directly inhibit the growth of <i>S. Typhimurium</i> ...	71
Figure 19. Cell viability assay with p62 agonists.....	72
Figure 20. p62 agonists do not affect bacterial entry.....	73
Figure 21. Schematic diagram of p62 ZZ domain and pull-down assay .....	74
Figure 22. p62 agonists accelerate autophagosome biogenesis and autophagic flux.....	76
Figure 23. p62 agonists induce p62 oligomerization that induces autophagosome biogenesis.....	78
Figure 24. p62 agonist YTK2205 induces autophagolysosome formation.....	80
Figure 25. p62 agonist rescue autophagic activities from suppression by <i>S. Typhimurium</i> .....	81
Figure 26. Canonical autophagy activator rapamycin cannot rescue autophagic	

activities from suppression by <i>S. Typhimurium</i> .....	83
Figure 27. The antimicrobial effect of p62 agonist is p62 ZZ domain-dependent	84
Figure 28. p62 agonists facilitate the association of p62 with intracellular <i>S.</i> <i>Typhimurium</i> .....	86
Figure 29. p62 agonist YTK-A76 facilitates the association of p62 with intracellular <i>S. Typhimurium</i> via the ZZ domain of p62.....	88
Figure 30. The p62 agonist-induced p62 association with intracellular <i>S.</i> <i>Typhimurium</i> requires PB1 and UBA domain.....	90
Figure 31. Association of p62 with intracellular <i>S. Typhimurium</i> requires ubiquitination of the pathogen.....	92
Figure 32. The antimicrobial effect of p62 agonist YTK-A76 requires ubiquitination of intracellular <i>S. Typhimurium</i> .....	94
Figure 33. The antimicrobial effect of p62 agonist against <i>S. Typhimurium</i> strains with mutations in SPI-1.....	95
Figure 34. p62 agonist increases association of LC3B with intracellular <i>S.</i> <i>Typhimurium</i> .....	96
Figure 35. The antimicrobial effect of p62 agonist YTK-A76 requires autophagic activity.....	98
Figure 36. The p62 agonist accelerates targeting of <i>S. Typhimurium</i> to autophagosomes.....	100
Figure 37. Canonical autophagy inducer rapamycin has no antimicrobial effect against intracellular <i>S. Typhimurium</i> .....	102
Figure 38. Rapamycin does not induce targeting of <i>S. Typhimurium</i> to autophagosomes.....	104

Figure 39. Resveratrol does not inhibit the growth of intracellular bacteria.....	105
Figure 40. Antimicrobial effect of p62 agonists against intracellular <i>Mycobacterium tuberculosis</i> .....	106
Figure 41. p62 agonists do not show host or bacterial cell toxicity and do not affect bacterial entry .....	108
Figure 42. p62 agonists facilitate the association of p62 with intracellular Mtb-EFRP.....	110
Figure 43. p62 agonist YTK-2205 accelerates targeting of intracellular <i>M. tuberculosis</i> to autophagosomes .....	112
Figure 44. p62 agonists increase lysosome targeted intracellular <i>M. tuberculosis</i> .....	114
Figure 45. p62 agonist YTK-2205 accelerates the targeting of intracellular <i>M. tuberculosis</i> to autophagosomes .....	115
Figure 46. Antimicrobial effect of YTK-A76 against intracellular <i>E. coli</i> and <i>S. pyogenes</i> .....	117
Figure 47. p62 agonists reduce bacterial burden and inflammation in the liver and spleen of <i>S. Typhimurium</i> -infected mice .....	118
Figure 48. p62 agonist YT-6-2 reduces bacterial burden and inflammation in lung of <i>M. tuberculosis</i> -infected mouse.....	120
Figure 49. YTK-2205 reduces bacterial burden and inflammation in the lung of BCG-infected mice. ....	122
Figure 50. YTK-6-2 reduces bacterial burden in the lung of multidrug-resistant <i>M. tuberculosis</i> -infected mouse.....	123
Figure 51. YTK-A76 reduces mRNA expression of inflammatory cytokines that	

are induced by <i>S. Typhimurium</i> infection .....	124
Figure 52. p62 agonists reduce mRNA expression of inflammatory cytokines that are induced by <i>M. tuberculosis</i> infection .....	125
Figure 53. YTK-2205 reduces inflammatory cytokine <i>Tnfa</i> in the lung of BCG- infected mouse.....	126
Figure 54. Graphical overview of the activation of p62-mediated xenophagy by p62 agonists.....	127

# List of abbreviations

AICAR: Acadesine/AICA riboside

AMPK: AMP-activated protein kinase

ANOVA: Analysis of variance

Arg: Arginine

ARIH1: Ariadne RBR E3 Ubiquitin Protein Ligase 1

ATE1: Arginyltransferase 1

ATG: Autophagy-related genes

ATP: Adenosine triphosphate

BCG: Bacillus Calmette–Guérin

cDNA: Complementary DNA

CFU: Colony-forming unit

BMDM: Bone marrow-derived macrophages

BSA: Bovine serum albumin

Degron: Degradation signal

DMEM: Dulbecco's modified eagle medium

DMSO: Dimethyl sulfoxide

DRAM1: DNA damage regulated autophagy modulator 1

*E. coli*: *Escherichia coli*

EGFP: Enhanced green fluorescent protein

ESX-1: ESAT-6 secretion system 1

FBS: Fetal bovine serum

HOIP: HOIL-1-interacting protein

ICC: Immunocytochemistry

kDa: Kilo Dalton

LC3: Light chain 3

LIR: LC3-interacting region

LPS: Lipopolysaccharide

LRSAM1: Leucine-rich repeat and sterile alpha motif-containing protein 1

Mtb: *Mycobacterium tuberculosis*

mTOR: Mechanistic target of rapamycin

NBR1: Neighbor of BRACA1 gene 1

Nt: N-terminal

OPTN: Optineurin

PAMP: Pathogen-associated molecular pattern

PB1: Phox and Bem1

PBS: Phosphate-buffered saline

PCR: Polymerase chain reaction

PE: Phosphatidylethanolamine

RFP-GFP: Red Fluorescent Protein – Green Fluorescent Protein

RT-PCR: Reverse transcription-polymerase chain reaction

SCV: Salmonella-containing vacuole

SDS: Sodium dodecyl sulfate

SDS-PAGE: Sodium dodecyl sulfate-polyacrylamide gel electrophoresis

siRNA: Small interfering RNA

SIRT1: Sirtuin 1

*S. pyogenes*: *Streptococcus pyogenes*

p62: Sequestosome 1

*S. Typhimurium*: *Salmonella enterica* serovar Typhimurium

TAX1BP1: Tax1 Binding Protein 1

TEM: Transmission electron microscopy

TMEM74: Transmembrane protein 74

*Tnfa*: Tumor necrosis factor- $\alpha$

Ub: Ubiquitin

UBA: Ubiquitin associated

ULK1: Unc-51 like autophagy activating kinase 1

UPS: Ubiquitin-proteasome system

UTR: Untranslated region

WIPI1: WD repeat domain phosphoinositide-interacting protein 1

WT: Wild-type

XID: Xenophagy-inducing drugs

# Introduction

All living creatures respond to external stimuli to actively maintain stable internal, physical, and chemical conditions optimal for survival, which is called 'homeostasis' [1]. The infection of pathogens such as viruses, bacteria, and fungi is one of the unfavorable stimuli that disturb delicately regulated homeostasis in the body [1]. Upon their infection, the immune system recognizes the invading microorganisms and maintains the homeostasis by eliminating or neutralizing the pathogens via well-organized systemic responses: an innate immune and antigen-specific adaptive immune response [2]. The innate immune system is an evolutionarily conserved host defense system that acts as the first line of defense against pathogens entering the body. It responds in the same mechanisms against all types of foreign substances by four pre-existing barriers such as physical (e.g., skin, mucous membrane, etc.), physiological (e.g., lysozyme), cellular (e.g., neutrophils, monocytes, macrophages), and cytokine barriers [2, 3]. By contrast, the adaptive immune system, also known as the acquired immune system, is highly specific to each particular invading pathogen. There are two types of adaptive responses: the cell-mediated immune response, which is performed by T cells, and the humoral immune response, which is controlled by activated B cells and antibodies [3, 4].

Innate immune cells, such as phagocytes including macrophages and dendritic cells represent the first line of defense and are key players in clearing the



invading pathogens [5]. Phagocytes recognize bacteria via pathogen-associated molecular patterns (PAMPs) by surface exposed, vesicular, or cytoplasmic pattern recognition receptors (PRRs) [6]. Surface PRRs include C-type lectins, mannose receptor (MR), dectin 1, dectin 2, Mincle, MCL, DC-SIGN, and scavenger receptors such as SR-A and MARCO, which not only recognize but also initiate appropriate signaling cascades that activate defense mechanisms in phagocytes themselves [6, 7]. Macrophages have evolved a myriad of defense strategies to combat infection with bacteria such as *M. tuberculosis* and *S. Typhimurium* [8]. The strategies include induction of toxic anti-microbial effectors, stimulation of microbe intoxication mechanisms, restriction of the microbe's access to essential nutrients, production of anti-microbial peptides or cytokines, or induction of autophagy to eliminate the intracellular pathogens [9].

The autophagy-lysosome pathway (ALP) has evolved as a stress response that allows unicellular organisms to survive during stressful conditions by regulating protein and organelle quality control (Figure 1) [10, 11]. This machinery is known to dispose of cytoplasmic material, including defective organelles and misfolded protein aggregates that are too large to be degraded by the other cellular degradation system called ubiquitin-proteasome system (UPS) (Figure 1) [11-14]. There are at least three types of autophagy: chaperone-mediated autophagy, micro-autophagy, and macro-autophagy [15, 16]. In chaperone-mediated autophagy (CMA), targeted proteins are translocated across the lysosomal membrane in a complex with chaperone proteins (such as Hsc-70) that are recognized by the lysosomal membrane receptor lysosomal-associated membrane protein 2A (LAMP-2A) [17]. In micro-autophagy, cytosolic components are directly taken up by the lysosome itself through

invagination of the lysosomal membrane [18]. In contrast, macro-autophagy (hereafter autophagy) delivers cytoplasmic cargo to a double membrane-bound vesicle called autophagosome, which outer membrane fuses with the lysosome to form an autolysosome [11, 15]. Autophagosomes can also fuse with endosomes or multivesicular bodies and major histocompatibility complex (MHC)- class-II-loading compartments [19]. The autophagosome membrane is generated through nucleation, elongation, and sealing of a small cisterna termed phagophore at a specific location known as the omegasome on the endoplasmic reticulum (ER) [15]. ALP is induced by various cellular stresses including nutrient deprivation, oxidative stress, hypoxia, radiation, and infection which stimulate cell signalings that trigger autophagy initiation, followed by phagophore formation, expansion, fusion with the lysosome, and degradation as a series of processes (Figure 2) [15]. This well-organized system is activated through inhibition of the mammalian target of rapamycin (mTOR), resulting in activation and translocation of ULK1 complex (ULK1/2, ATG13, FIP200, and ATG101) and the class III phosphatidylinositol-3-OH kinase (PI(3)K) complex including VPS34, VPS15, beclin1 and ATG14 to ER. The PI(3)K complex produces phosphatidylinositol-3-phosphate (PtdIns(3)P), which recruits effectors such as double FYVE-containing protein 1 (DFCP1) and WD-repeat domain phosphoinositide-interacting (WIPI) family proteins [15, 20]. Among the four WIPI1 isoforms, WIPI2 and DFCP1 to the autophagosome formation site to generate ER-associated  $\Omega$ -like structures termed omegasomes. At the final step of autophagosome formation, elongation of the isolation membrane and/or completion of enclosure requires two ubiquitin-like conjugates [20]. The first is the ATG12-ATG5 conjugate, which is produced by the ATG7 (E1-like) and ATG10 (E2-like)

enzymes, and functions as a dimeric complex together with ATG16L1. The second is the phosphatidylethanolamine (PE)-conjugated ATG8 homologues-LC3, GATE16, and GABARAP-which are produced by the ATG7 and ATG3 (E2-like) enzymes (Figure 2). Autophagy was originally considered as a non-selective bulk degradation system. However, it is now clear that autophagosomes can degrade substrates in a selective manner [10].

While bulk autophagy generates energy and amino acids during nutritional insufficiency, selective autophagy removes damaged, cytotoxic, or unwanted material [10, 21]. In selective autophagy, substrates are recognized by specific receptors such as p62/SQSTM1, NBR1 (NBR1 autophagy cargo receptor), OPTN (Optineurin), TAX1BP1, and CALCOCO2/NDP52 [22-24]. These autophagy receptors possess ubiquitin-associated (UBA) and MAP1LC3/LC3-interacting region (LIR) domains that bind ubiquitin chains assembled on cargoes and LC3 anchored on phagophores respectively [25, 26]. In addition to protein aggregates, selective autophagy mediates the degradation of subcellular organelles such as mitochondria, endoplasmic reticulum, and peroxisomes [10].

Recent studies show that invading pathogens such as viruses and bacteria can also be targeted by selective autophagy for lysosomal degradation [27-32]. This process, called xenophagy, involves various types of polyubiquitin chains that recruit autophagic receptors such as p62 and NBR1 [24, 25, 33]. When an extracellular pathogen is phagocytosed into a mammalian host cell, an arms race between the pathogen and the host begins. Once the bacteria internalized into the host cells, the bacteria reside within phagosomes for intracellular replication niche, escaping from the surveillance of host defense systems. A subpopulation of bacteria escapes into

the cytoplasm or damage vacuolar membrane compartments by type III secretion system (T3SS) effectors or ESX-1 type VII secretion system (T7SS) on the bacterial membrane that secretes bacterial effector proteins to modulate the functions of host cells [34-37]. Once cells sense bacteria in the cytosol, specific proteins on bacterial membranes are assembled with ubiquitin chains. Several E3 ligases were identified to ubiquitinate specific receptors on bacterial membranes, including PRKN/parkin that mediates K63-linked ubiquitination to target *Mycobacterium tuberculosis* (Mtb) to autophagic membranes via p62 and CALCOCO2 [38] and SMURF1 that mediates K48-linked ubiquitination for Mtb and *Listeria monocytogenes* [39]. In addition, the ubiquitination of *Salmonella enterica* serovar Typhimurium (*S. Typhimurium*) involves the cooperative activities of LRSAM1, ARIH1, and RNF31/HOIP (ring finger protein 31) [40-42]. Each type of bacteria may be marked with distinct ubiquitin codes, which are defined by the biochemical specificity of the E3 enzyme [42, 43]. Ubiquitinated bacteria are recognized by autophagy receptors to be targeted to autophagosomes for degradation [44]. Consistent with the previous studies, I found that cells require an increase in the level of autophagy-related genes and the protein level of autophagy receptors including p62 and Optineurin upon *S. Typhimurium* infection.

Pathogens have evolved to gain unique strategies to evade the host defense system or even hijack the autophagy machinery to survive and proliferate within host cells [45]. Bacteria such as *Salmonella Typhimurium*, *Mycobacterium tuberculosis*, *Streptococcus pyogenes*, *Legionella pneumophila*, *Shigella flexneri*, and *Francisella tularensis* have been reported to escape autophagy and each species of the bacteria

developed their own delicate strategies to inhibit autophagy [34, 46]. Intracellular bacteria manipulate autophagy by inhibiting autophagy-initiation signaling or autophagosome formation, evading autophagy recognition by masking the bacterial surface, blocking autophagosome fusion with the lysosome, or hijacking autophagy [47, 48]. *S. Typhimurium* inhibits autophagy initiation via regulation of the AMPK-dependent activation pathway of mTOR by inducing lysosomal degradation of Sirt1, LKB1, and AMPK [36]. In addition, SseF and SseG effector proteins secreted by the bacteria suppress autophagy initiation by activating host Rab1A GTPase through direct interaction followed by inhibition of the recruitment and activation of ULK1 [49]. Moreover, *M. tuberculosis* secretes not only Eis effector protein that mediates acetylation and activation of a JNK-specific phosphatase mitogen-activated protein kinase phosphatase-7 (MKP-7) to inactivate autophagy initiation but also SapM that hinders Rab5-Rab7 exchange to suppress autophagosome maturation [50, 51]. Furthermore, in this study, I found that *S. Typhimurium* suppresses the protein level of LC3B, autophagosome biogenesis, and autophagic flux by post-translational modulation.

To eradicate invading pathogens that escaped killing by autophagy and thrive, several generations of antibiotics such as penicillins, cephalosporins, and fluoroquinolones have been developed [52, 53]. Antibiotics, also known as antibacterials, are substances that destroy or slow down the growth of bacteria by directly binding and inhibiting bacterial cellular systems such as cell walls, nucleic acid, and protein synthesis [53]. However, due to the fast-growing bacterial nature, the pathogens evolved to gain resistance to the antibiotics and threaten our lives [54]. Therefore, it is important and urgent to develop fundamentally different approaches

to bacterial infectious diseases. There are several anti-microbial strategies such as phage therapy, vaccines, antibodies, probiotics, antimicrobial peptides, and host-directed therapy [53, 55, 56]. Host-directed therapeutics utilize small molecule drugs or proteins to suppress bacterial growth by a host-mediated response to pathogens rather than by acting directly on the pathogens [57]. These therapeutics provide an antimicrobial and beneficial effect by interfering with host mechanisms exploited by the pathogen, boosting host immune response, reducing exacerbated inflammation, or modulating host factors at the site of infection.

Among host-directed therapies, the biochemical modulation of autophagy is emerging as a universal means to eradicate intracellular bacteria using lysosomal hydrolases [57, 58]. To develop xenophagy-inducing drugs, several chemicals were identified to inhibit the infectivity of intracellular bacteria by activating autophagy. Rapamycin enhances colocalization of Mtb with LC3 and acidification of mycobacterial phagosomes *in vitro* at 50  $\mu$ M 2 h after infection in a manner independent of autophagy [59, 60]. In another study, however, rapamycin facilitated the infectivity of Mtb when treated at 1  $\mu$ M for 3 days *in vitro* [59]. The antidiabetic drug metformin upregulates lipidated LC3 form and shows an antimicrobial effect *in vitro* at 1 mM and in mice at 500 mg/kg (q.o.d. injection, i.p.) [61]. The AMPK activator AICAR inhibits the infectivity of Mtb *in vitro* at 50-100  $\mu$ M and in mice at 500 mg/kg i.p. by activating autophagic pathways [62]. Resveratrol, a SIRT1 (sirtuin 1) activator, shows moderate efficacy against Mtb *in vitro* at 10-100  $\mu$ M [63]. AR-12, triclosan, and D61 also exhibit antimicrobial effects against *S. Typhimurium* *in vitro* at various concentrations [64, 65]. To date, there are no known xenophagy-

inducing drugs with satisfactory efficacy via a clear mode of action.

The N-degron pathway is a proteolytic system in which the protein half-life is determined by destabilizing N-terminal (Nt) residues, called N-degrons [66-68]. The N-degrons are generated by Met aminopeptidases or at the internal residues by endopeptidases, such as caspases, separases, and signal peptide peptidases: positively charged (Arg, Lys and His; type 1) and bulky hydrophobic (Phe, Tyr, Trp, Leu, and Ile; type 2) N-terminal residues. Among these, the Nt-Arg can be generated by post-translational conjugation of the amino acid L-Arg to Nt-Asp or Nt-Glu by ATE1-encoded R-transferases (Figure 3) [66]. These N-degrons are recognized by the E3 enzymes called N-recognins UBR1, UBR2, UBR4, and UBR5 that mediate substrate ubiquitination for proteasomal degradation via the ubiquitin-proteasome system (UPS) (Figure 3) [69]. The ubiquitination of substrates requires an E1-E2-E3 enzymatic cascade. E1 uses ATP to activate ubiquitin, E2 carries the ubiquitin, and E3 recognizes substrates and catalyzes isopeptide bond formation between ubiquitin and the substrates [12, 13, 70]. The substrates tagged by ubiquitin chains are recognized and degraded by the subunits of multicatalytic protease complexes called proteasomes [12]. To date, proteins that are degraded through the N-degron pathway are known as RGS4, RGS5, RGS16 (regulator of G protein signaling), GNG2 (G protein subunit  $\gamma$ 2), IAP1 (inhibitor of apoptosis protein 1), and SCC1 (sister chromatid cohesin 1) [71-74].

Among the N-degrons, Nt-Arg serves as a pivotal regulator of autophagic proteolysis under cellular stresses (Figure 3) [75-78]. Upon proteasomal and ER stress, the misfolded protein aggregates induce both relocation of ER-resident proteins such as BiP/GRP78, calreticulin, and protein disulfide isomerase proteins

to the cytoplasm and their Nt-arginylation by ATE1 [76]. Under binding of the cytosolic Nt-Arg to the ZZ domain of p62, the autophagy receptor undergoes a conformational change, exposing its PB1 and LC3-interacting domains which facilitates its self-polymerization in complex with cargo proteins and targeting to autophagosomes [76]. In addition, Arg N-degron and its chemical mimetics induce autophagosome biogenesis by activating p62 leading to the degradation of misfolded protein aggregates in neurodegeneration and the autophagic turnover of the ER [77, 78]. Although the autophagic Arg/N-degron pathway is well studied, physiological relevance, including pharmacological regulation of the mechanism, has not yet been fully investigated.

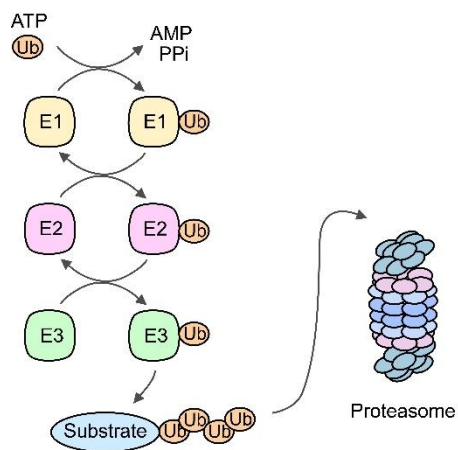
In this study, I present counteractive crosstalk between invading bacteria and selective autophagy. Host cells increase the level of autophagy-related genes and the protein level of autophagy receptors including p62 and Optineurin as a host defense mechanism against *S. Typhimurium* infection. Among the autophagy receptors, p62 played a pivotal role in the recognition and targeted degradation of the intracellular bacteria via the autophagy-lysosomal pathway. On the other hand, intracellular *S. Typhimurium* suppressed the autophagy activity by repressing the protein level of LC3B, autophagosome biogenesis, and autophagic flux.

Furthermore, I show that intracellular bacteria can be eradicated by the biochemical activation of mTOR-independent selective autophagy. Although antibiotics are developed to deal with bacterial infection, the fast-growing nature of bacteria allowed them to gain resistance to conventional antibiotics [52-54]. Here, as a host-directed therapeutic, I used chemical Nt-Arg mimetics that facilitate mTOR-independent autophagosome biogenesis via the ZZ domain of p62.



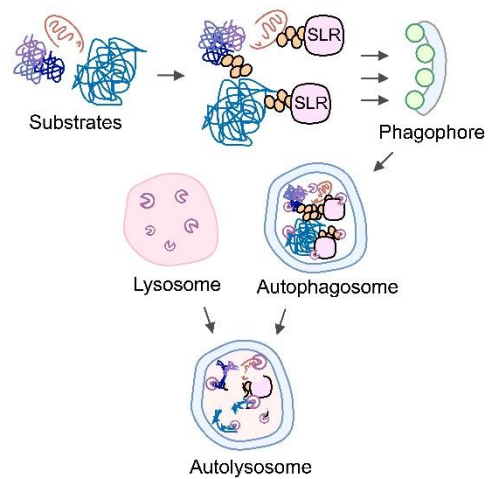
Fortunately, the p62 ligands showed an antimicrobial effect against intracellular *S. Typhimurium* or *M. tuberculosis* by promoting not only the recognition of the bacteria by p62 but also targeting the bacteria to the autophagosomes via the autophagy receptor. These xenophagy modulators also showed potent antimicrobial efficacy against even multidrug-resistant Mtb. Furthermore, the xenophagy-inducing drugs (XIDs), suppressed excessive production of inflammatory cytokines upon bacterial infection *in vitro* and *in vivo*. These results suggest the therapeutic potential of the autophagic Arg/N-degron pathway in selective autophagy against a broad spectrum of bacterial infectious diseases.

### Ubiquitin Proteasome System (UPS)



Soluble, misfolded, or unfolded protein substrates

### Autophagy



Insoluble & aggregated proteins or damaged organelles

**Figure 1. Two major intracellular degradation pathways: the ubiquitin-proteasome system (UPS) and the autophagy-lysosomal pathway (ALP).**

① Initiation      ② Nucleation      ③ Phagophore elongation      ④ Maturation & fusion      ⑤ Degradation

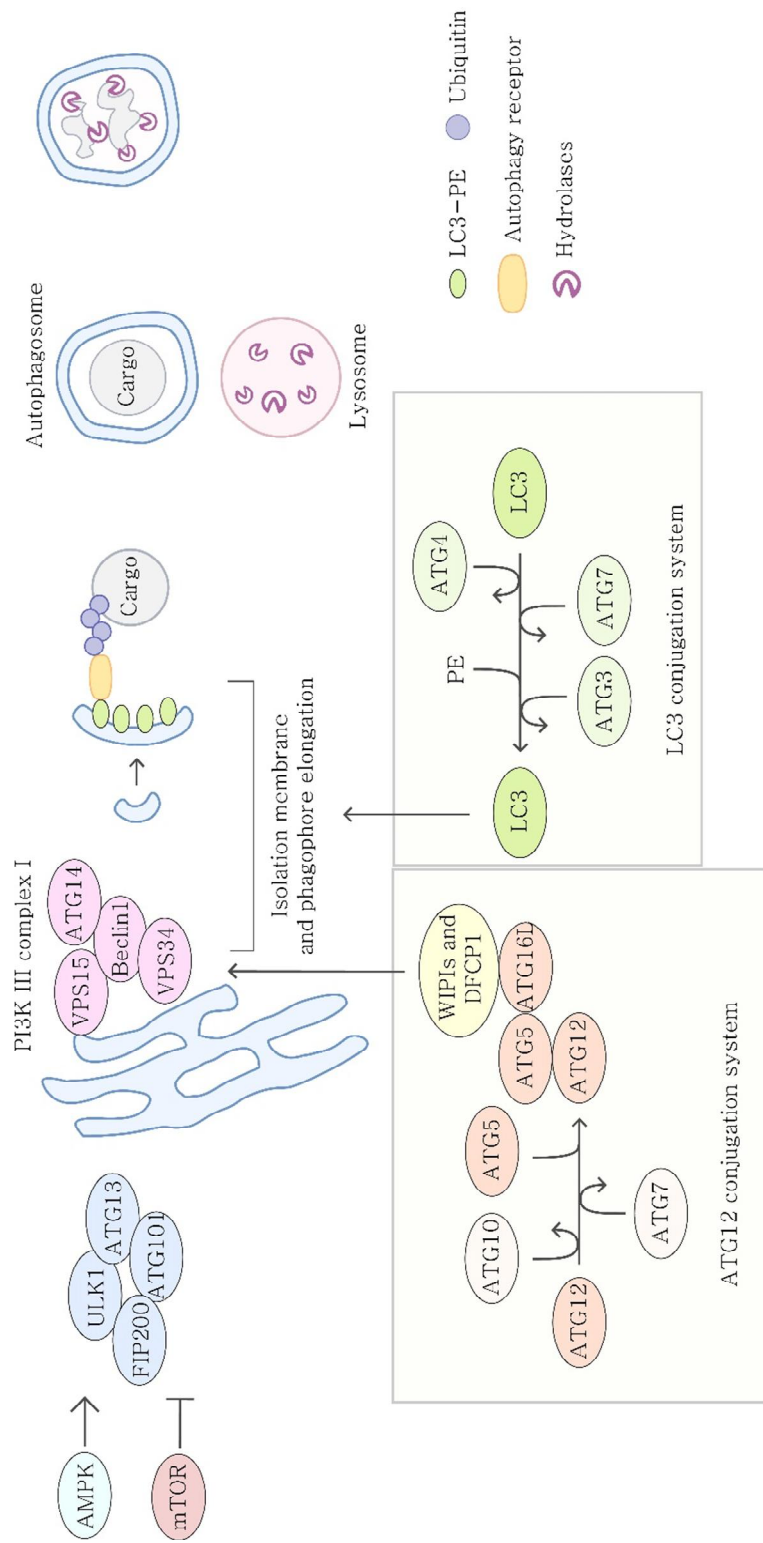


**Figure 2. A schematic of the stages of the autophagy-lysosomal pathway.**

Nutrient deprivation lead to AMPK activation and inhibition of mTOR whereas growth signals activate mTOR through PI3K-AKT signaling pathway. Inhibition of mTOR results in activation of ULK complex by hypophosphorylation of ATG13, which can then interact with ULK1 and FIP200. ULK functions in complex with FIP200, ATG13, and ATG 101, which phosphorylate Beclin-1, leading to VPS34 activation and initiation of phagophore formation. Nucleation and phagophore elongation require activity of phosphoinositide-3-kinase (PI3K) complex I (ATG 14, ATG15, Beclin-1, and VPS34), which generates the phosphatidylinositol 3-phosphate required to recruit other factors involved in phagophore elongation such as ATG12 and LC3 conjugation systems. Phosphatidylethanolamine modification at the C-terminus of the LC3 is induced by ubiquitination analogous conjugation cascade including ATG7 (E1-like), ATG10 (E2-like), and ATG12-ATG5-ATG6 complex (E3-like). As a result of this membrane expansion, cargo destined for autophagy is surrounded and engulfed into a double-membrane vesicle containing LC3-II and autophagy receptors called the autophagosome. The outer autophagosomal membrane fuse with the outer membrane of lysosome and cargoes contained in autophagic body are degraded by lysosomal hydrolases.



**Figure 3. A schematic diagram of the mammalian N-degron pathway in the UPS and autophagy.**

The N-degrons are generated by Met aminopeptidases or at the internal residues by endopeptidases, such as caspases, separases, and signal peptide peptidases. The degrons can be subdivided as tertiary, secondary, and primary. The tertiary destabilizing Nt-Asn and Gln are deamidated by two distinct enzymes, NTAN1 and NTAQ1 into Asp and Glu, respectively. The secondary destabilizing N-terminal residues Asp and Glu are arginylated by ATE1 R-transferase isoforms produced through alternative splicing of ATE1. The Nt-Cys requires its oxidation prior to arginylation by ATE1. C\* denotes oxidized Nt-Cys residue, either Cys-sulfinic acid [CysO<sub>2</sub>(H)] or Cys-sulfonic acid [CysO<sub>3</sub>(H)]. In proteasomal proteolysis, Nt-Arg and the other type 1 and type 2 residues directly bind to the UBR box of the N-recognins including UBR1, UBR2, UBR4, and UBR5. Following the recognition, the substrates are ubiquitinated for proteasomal degradation. In autophagic proteolysis, the accumulated cytosolic misfolded proteins trigger Nt-arginylation and cytosolic relocation of ER-residing chaperones such as BiP and PDI. Among Nt-arginylated ER proteins, R-BiP binds to the autophagic receptor p62 that induce self-oligomerization of p62 and biogenesis of autophagosomes.

# Material and Methods

## Plasmids and reagents

The recombinant p62 plasmids were constructed as previously described (Chamolstad et al., 2017). PCR amplification of a full-length human p62 cDNA fragment from the hMU012675 clone (21C Frontier Human Gene Bank) was followed by subcloning into the pcDNA3.1/myc-His plasmid (Thermo Fisher Scientific) at EcoRI/XhoI sites. The DPB1 and DUBA domain p62 mutants were generated identically. Full-length p62-EGFP and the ZZ domain mutant p62-EGFP plasmids were subcloned as described above but into the pEGFP-N1 plasmid (Clontech) at EcoRI/XhoI sites. These plasmids were transiently transfected with Lipofectamine 2000 reagent following the manufacturer's instructions (Invitrogen). Normal goat serum (ab7481) was obtained from Abcam. Hoechst 33342 (H21492) was obtained from Invitrogen. 4',6-Diamidino-2-phenylindole dihydrochloride (DAPI; D8417) was obtained from Sigma. Vectashield antifade mounting medium (H1000) was from the Vector lab. Other reagents used in this study were bafilomycin A1 (Santa Cruz, SC-201550A), and NH<sub>4</sub>Cl (Sigma, A9434).

## Antibodies

mouse monoclonal anti-p62 (Abcam, ab56416, 1:40,000), rabbit polyclonal anti-Optineurin (Abcam, ab23666, 1:1,000), mouse monoclonal anti-FK2 specific to Ub-

conjugated proteins (Enzo Life Science, BML-PW8810, 1:5,000), rabbit polyclonal anti-LC3 (Sigma, L7543, 1:40,000), rabbit polyclonal anti-LC3A/B (Medical & Biological Laboratories International, PM036, 1:500), rabbit polyclonal anti- $\beta$ -actin (BioWorld, Cat#, 1:10,000), rabbit polyclonal anti-Salmonella (Abcam, ab35156, 1:1000), rat monoclonal anti-LAMP1 (Santa Cruz Biotechnology, sc-19992, 1:400), rabbit polyclonal anti-NDP52 (Abcam, ab68588, 1:1,000), mouse monoclonal anti-NBR1 (Abcam, ab55474, 1:1,000), rabbit monoclonal anti-TAX1BP1 (Cell signaling, 5105S, 1:1,000) and rabbit polyclonal anti-Myc (Santa Cruz, sc-764, 1:400). The following secondary antibodies are Alexa fluor 488 goat anti-rabbit IgG (Invitrogen, A11029, 1:500), Texas Red goat anti-mouse IgG (Invitrogen, T6390, 1:500), anti-rabbit IgG-HRP (Cell Signaling, 7074, 1:10,000), and anti-mouse IgG-HRP (Cell Signaling, 7076, 1:10,000).

## **Cell culture**

RAW264.7, J774A.1, THP-1, and HCT116 cells were purchased from the Korean Cell Line Bank. CCL2 HeLa cells were purchased from the American Type Culture Collection (ATCC). RAW264.7, J774A.1, and THP-1 cells were cultured in Rosewell Park Memorial Institute (RPMI). HeLa cells were cultured in Dulbecco's Modified Eagle's Medium (DMEM; Gibco, 10566016). HCT116 cells were cultured in McCoy's 5a Medium (GIBCO # 16600). All of the media were supplemented with 10% FBS and 100 units/mL penicillin/streptomycin. Primary BMDMs were isolated from C57BL/6 mice and cultured in DMEM. BMDMs were differentiated for 3–5 days in the presence of macrophage colony-stimulating factor (M-CSF; R&D



Systems). For the preparation of PMs, each mouse was injected (i.p.) with 1 ml of 3% thioglycollate and after 3 days the peritoneal fluid was collected in ice-cold PBS containing 3% FBS. The collected cell suspension was centrifuged and the cells were counted. All the cell lines were determined to be negative in a mycoplasma test using a MycoAlert detection kit (Lonza, LT07-118). All the culture plates and the cell lines were maintained at 37°C and 5% CO<sub>2</sub> in a humidified incubator.

## **Mice**

C57BL/6 mice (sex-matched) aged 6–8 weeks with a wild-type (WT) background were purchased from Samtako Bio Korea (Gyeonggi-do, Korea). Mice were maintained under specific pathogen-free conditions. All mice experiments and maintenance were done in adherence to guidelines set forth by the Institutional Animal Care and Use Committee, Seoul National University (SNU-190531-2-1) and Chungnam National University School of Medicine (202009A-CNU-155, CNUH-A0044-1), and the Korean Food and Drug Administration. For the Salmonella model, C57BL/6 mice aged 8 weeks were given  $1 \times 10^6$  *S. Typhimurium* and p62 agonist (20 mg/kg) by i.p. injection. The mice were given p62 agonist (20 mg/kg) by i.p. daily for 6 days and at which point they were killed, the liver and spleen removed, homogenized, resuspended in PBS, and plated on Luria Broth agar plates. The plates were incubated overnight at 37°C and colonies were counted. For the Mtb model, C57BL/6 aged 8 weeks were given  $5 \times 10^4$  Mtb by intranasal injection and the p62 agonist (10-20 mg/kg) by i.p. injection. After infection, the mice were i.p. injected with YTK-2205 q.o.d. 5 times and harvested at day 10 and YT-6-2 t.i.w. for 28 days.

For the MDR-TB infection model, C57BL/6 aged 8 weeks were given  $5 \times 10^3$  Mtb by intranasal injection and the YT-6-2 (20 mg/kg) by i.p. injection. After infection, the mice were i.p. injected with YT-6-2 t.i.w. for 28 days and the lung was removed, homogenized, and resuspended in PBS and plated on 7H10 agar. Mtb and MDR-TB infection model was conducted in cooperation with co-researcher Young Jae Kim from professor Jo's laboratory (Chungnam National University).

### **Bacterial strains and culture**

*S. Typhimurium* was kindly provided by Eun Jin Lee (Korean University, Seoul, Korea). *S. Typhimurium* was cultured at 37°C in LB broths with shaking. For the analysis of replication rates of *S. Typhimurium*, the absorbance of bacterial suspension at 600 nm wavelength was measured. Mtb H37Rv was kindly provided by Dr. R. L. Friedman (University of Arizona, Tucson, AZ, USA). *M. Bovis* BCG and MDR-Mtb (KMRC 00116-00150) were obtained from the Korean Institute of Tuberculosis (Osong, Korea). Mtb and BCG were grown at 37°C with shaking in Middlebrook 7H9 broth (Difco, 271310) supplemented with 0.5% glycerol, 0.05% Tween-80 (Sigma-Aldrich), and oleic albumin dextrose catalase (OADC; BD Biosciences, 212240). For Mtb-expressing enhanced red fluorescent protein (ERFP) strains were grown in Middlebrook 7H9 medium supplemented with OADC and 50 µg/ml kanamycin (Sigma-Aldrich, 60615). All mycobacterial suspensions were aliquoted and stored at -80°C. For all experiments, mid-log-phase bacteria (absorbance 0.4) were used. Representative vials were thawed and CFUs enumerated by serially diluting and plating on Middlebrook 7H10 agar (Difco, 262710). *E.coli*

(KCCM 21052) and *S.pyogenes* (KCCM 11814) were obtained from the Korean Culture Center of Microorganisms (Seoul, Korea).

## **Bacterial infection**

*S. Typhimurium* was inoculated at 2 mL LB broth and cultured at 37°C overnight. 100 µl suspension of *S. Typhimurium* was subcultured in 10 mL LB for 3 h. The absorbance of bacterial suspension was measured and diluted suspension of *S. Typhimurium* was inoculated to cultured cells with indicated MOI for 30 min. After the incubation, the cells were washed with Dulbecco's Phosphate Buffered Saline (DPBS; Thermo Fisher Scientific, 14040133), and the cells were treated with media containing 100 µg/ml gentamycin (Thermo Fisher Scientific, 15710064) for one hour and the media was exchanged with fresh medium including 10 µg/ml gentamycin. Cells were infected with indicated MOI of Mtb for 2 h. Extracellular bacteria were washed with PBS and infected cells were further cultured in fresh media for the indicated time. For *in vivo* infection, frozen Mtb or BCG were thawed and inoculated intranasally (Mtb;  $5 \times 10^4$  CFU/mice, BCG;  $1 \times 10^7$  CFU/mice, MDR-Mtb;  $5 \times 10^3$  CFU/mice). To measure the bacterial burden, lungs were harvested after sacrificing the mice after 10 days of Mtb infection, 7 days of BCG, and 10 or 28 days of MDR-Mtb infection. Lungs were homogenized in PBS and serial dilutions of the homogenates were plated in 7H10 agar plates. After 2-3 weeks, colonies were counted. Mtb and BCG related experiments were conducted in cooperation with co-researchers Jin Kyung Kim and Young Jae Kim from professor Jo's laboratory (Chungnam National University).

## **Mouse *Sqstm1* lentiviral short hairpin RNA (shRNA) production and transduction**

To produce shRNA, packaging plasmids (pRSVRev, pMD2.VSV-G, and pMDLg/pRRE purchased from Addgene) and pLKO.1-based target shRNA plasmids (m*Sqstm1*, TRCN0000238133 purchased from Sigma-Aldrich) were cotransfected into HEK293T cells using Lipofectamine 3000 (Invitrogen). Then, 48 h later, the virus-containing supernatant was collected and filtered. For lentivirus infection, BMDMs in DMEM containing 10% FBS were seeded into 24-well plates and infected with lentiviral vectors (MOI of 10), according to the manufacturer's protocol. After 3 days, the samples were analyzed for transduction efficiency.

## **Generation of a tandem LC3B (mCherry-EGFP-LC3B) retroviral vector**

Phoenix amphotropic cells (ATCC, CRL-3213) were seeded and co-transfected with 0.75 µg of packaging plasmid pCL-Eco (Addgene, 12371), 0.25 µg of envelope plasmid pMDG (Addgene, 12259), and 1 µg of pBABE puro mCherry-EGFP-LC3B plasmid (Addgene, 22418) using Lipofectamine 2000. After 6 h, the medium was replaced with a fresh culture medium. The retrovirus-containing medium was harvested at 24 h post-transfection and filtered through a 0.45-µm syringe filter.

## **RNA extraction and qRT-PCR analysis**

Total RNA from homogenized lung or cell was isolated using TRIzol reagent (Thermo Fisher Scientific, 15596-026), following the manufacturer's instructions.

After RNA quantitation, cDNA was synthesized by reverse transcription using the reverse transcriptase premix (Elpis Biotech, EBT-1515). Real-time PCR (qRT-PCR) was performed using SYBR green master mix (Qiagen) and primers for indicated genes, in Rotor-Gene Q 2plex system (Qiagen). Data were analyzed using  $2^{-\Delta\Delta}$  threshold cycle (Ct) method where mouse Gapdh was used for normalization. Data are expressed as relative fold changes. Primers sequences (mouse) were as follows: SQSTM1 forward: 5'-CCTCTGGGCATTGAAGTTG-3', reverse: 5'-TATCCGACTCCATCTGTTCCCTC-3'; NBR1 forward: 5'-GGAAGCAGAAGAA GACCTGAGTG-3', reverse: 5'-CCAGAGTCTGTGAGGTCGTGAG-3'; OPTN forward: 5'-AGCAAACCATTGCCAAGC-3', reverse: 5'-TTTCAGCATGAAAAT CAGAACAG-3'; NDP52 forward: 5'-GCCCATTGACCTAAACAACAAA-3', reverse: 5'-CACACCATCCTCATCCACATAG-3'; TAX1BP1 forward: 5'-ACAA AGGCCACCTGTCAGAG-3', reverse: 5'-GGCACATTCTCATCTTCTTTGC-3'; Il1b forward: 5'-TGACGGACCCCAAAAGATGA-3', reverse: 5'-AAAGACAC AGGTAGCTGCCA-3'; Il6 forward: 5'-ACAAAGCCAGAGTCCTTCAGA-3', reverse: 5'-TGGTCCTTAGCCACTCCTTC-3'; Cxcl5 forward: 5'-GCACTCG CAGTGGAAAGAAC-3', reverse: 5'-CGTGGGTGGAGAGAATCAGC-3'; Tnfa forward: 5'- CCCACGTCGTAGCAAACCAC-3', reverse: 5'- GCAGCCTTGT CCCTTGAAGA-3'; Gapdh forward: 5'-TGGCAAAGTGGAGATTGTTGCC-3', reverse: 5'-AAGATGGTGATGGGCTTCCCG-3'. The mRNA expression level of autophagy-related genes was analyzed by using the AccuTarget™ qPCR screening kit (Bioneer, SH-0017-10).

## Chemical synthesis and analytical data of p62 ligands

Ligands to the p62-ZZ domain – YTK-A76, YT-6-2, YOK-1204, YTK-2205, and YOK-1109 as well as the negative control ligand ATB1095 – were synthesized as follows.

### Scheme 1. Synthesis of 2-(2-((3,4-bis(benzyloxy)benzyl)amino)ethoxy)ethan-1-ol (YTK-A76)

#### 1.1. Synthesis of 3,4-bis(benzyloxy)benzaldehyde (A2)

To a solution of A1 (0.5 g, 3.62 mmol) in dimethylformamide was added  $K_2CO_3$  (1.5 g, 10.86 mmol) and (bromomethyl)benzene (0.92 mL, 7.96 mmol) at RT. The mixture was stirred at 60°C for 4 h. The reaction mixture was cooled at room temperature and extracted with ether and water. The organic layer was washed with brine, dried over anhydrous  $MgSO_4$ , filtered and concentrated. The residue was purified by column chromatography on silica gel to afford A2 (3,4-bis(benzyloxy)benzaldehyde, 1.04 g, 90%).  $^1H$ -NMR ( $CDCl_3$ , 300 MHz)  $\delta$  (ppm) 9.81 (s, 1H), 7.49-7.31 (m, 12H), 7.04 (d,  $J$  = 8.3 Hz, 1H), 5.27 (s, 2H), 5.22 (s, 2H) LCMS; Mass Calcd.: 318.33; MS Found: 319.13 [MS+1].

#### 1.2. Synthesis of 2-(2-((3,4-bis(benzyloxy)benzyl)amino)ethoxy)ethan-1-ol (YTK-A76)

A mixture of A2 (20 g, 62.8 mmol) added in MeOH (500 mL) and tetrahydrofuran (200 mL), Then added 2-(2-aminoethoxy)ethanol (13.2 g, 126 mmol) and sodium

triacetoxyborohydrid (40 g, 189 mmol) at room temperature. The mixture reaction was stirred overnight at RT. The reaction mixture was quenched by the addition of saturated aqueous  $\text{NH}_4\text{Cl}$  (200 mL). The aqueous layer was extracted with ethyl acetate, and concentrated. The crude was added PE and stirred for 1 h, then filtered to give YTK-A76 (2-(2-((3,4-bis(benzyloxy)benzyl)amino)ethoxy)ethan-1-ol, 10 g, 39.1%) as a white solid.  $^1\text{H-NMR}$  ( $\text{CDCl}_3$ , 400 MHz)  $\delta$  (ppm) 9.57 (s, 1H), 7.48 (d,  $J = 7.2$  Hz, 2H), 7.27-7.41 (m, 9H), 6.99-7.02 (m, 1H), 6.84 (d,  $J = 8.4$  Hz, 1H), 5.25 (s, 2H), 5.09 (s, 2H), 4.06 (s, 1H), 3.65-3.70 (m, 4H), 3.46-3.48 (m, 2H), 2.87 (t,  $J = 4.8$  Hz, 2H) LCMS; Mass Calcd.:407.21; MS Found: 408.90 [ $\text{MS}+1$ ].

**Scheme 2. Synthesis of (R)-1-(3,4-bis((4-fluorobenzyl)oxy)phenoxy)-3-((2-hydroxyethyl)amino)propan-2-ol (YT-6-2)**

2.1. Synthesis of 3,4-bis((4-fluorobenzyl)oxy)benzaldehyde (B1)

To a solution of A1 (100 g, 724.6 mmol) in ACN (1 L) were added 1-(bromomethyl)-4-fluorobenzene (301.3 g, 1.59 mol) and  $\text{K}_2\text{CO}_3$  (300 g, 2.17 mol). The mixture was stirred at  $80^\circ\text{C}$  for 16 h. Then the reaction was concentrated, the residue was purified by silica gel, eluted with EA/PE (1:15~1:8) to afford B1 (3,4-bis((4-fluorobenzyl)oxy)benzaldehyde, 187 g, 72.8%) as a white solid.  $^1\text{H-NMR}$  ( $\text{DMSO-d}_6$ , 400 MHz)  $\delta$  (ppm) 9.83 (s, 1H), 7.55-7.48 (m, 6H), 7.3-7.2 (m, 5H), 5.25 (s, 2H), 5.19 (s, 2H).

2.2. Synthesis of 3,4-bis((4-fluorobenzyl)oxy)phenol (B2)

To a solution of B1 (187 g, 526.7 mmol) in DCM (2 L) was added m-CPBA (126 g, 730.4 mmol). The mixture was stirred at RT for 16 h. Then the reaction was washed

with saturated sodium bicarbonate solution, concentrated under vacuum. Then the crude product is added to methanol (1.5 L) and water (200 mL) was added KOH (58.9 g, 1.05 mol). The mixture was stirred at RT for 3 h. Then the reaction was filtered and the solid to dryness under vacuum. The crude compound was purified by silica gel, eluted with EA/PE (1:15~1:5) to afford B2 (3,4-bis((4-fluorobenzyl)oxy)phenol, 151 g, 83.7 %) as an off-white solid. <sup>1</sup>H-NMR (DMSO-d<sub>6</sub>, 400 MHz) δ (ppm) 7.50-7.41 (m, 4H), 7.24-7.15 (m, 4H), 6.82 (d, J = 8.4 Hz, 1H), 6.49 (d, J = 2.4 Hz, 1H), 6.25 (dd, J = 8.8, 2.8 Hz, 1H), 5.04 (s, 2H), 4.95 (s, 2H).

### 2.3. Synthesis of (R)-2-((3,4-bis((4-fluorobenzyl)oxy)phenoxy)methyl)oxirane (B3)

To a solution of B2 (45.8 g, 134 mmol) in EtOH (500 mL) were added water (25 mL) and KOH (17.2 g, 307 mmol). Then (R)-2-(chloromethyl)oxirane (37 g, 400 mmol) was added to the reaction. The resulting mixture was stirred at RT for 16 h. Then the reaction was quenched by addition water, extracted with EA. The organic layer was washed with brine, dried over Na<sub>2</sub>SO<sub>4</sub>, filtered and concentrated. The residue was purified by silica gel, eluted with EA/PE (1:15~1:10) to afford B3 ((R)-2-((3,4-bis((4-fluorobenzyl)oxy)phenoxy)methyl)oxirane, 26 g, 48.7%) as a white solid. <sup>1</sup>H-NMR (DMSO-d<sub>6</sub>, 400 MHz) δ (ppm) 7.51-7.43 (m, 4H), 7.25-7.16 (m, 4H), 6.94 (d, J = 9.2 Hz, 1H), 6.73 (d, J = 2.8 Hz, 1H), 6.45 (dd, J = 8.8, 2.8 Hz, 1H), 5.10 (s, 2H), 5.00 (s, 2H), 4.24 (dd, J = 11.2, 2.8 Hz, 1H), 3.75 (dd, J = 11.2, 6.4 Hz, 1H), 3.30-3.28 (m, 1H), 2.83 (t, J = 5.2 Hz, 1H), 2.68 (dd, J = 5.2, 2.8 Hz, 1H).

### 2.4. Synthesis of (R)-1-(3,4-bis((4-fluorobenzyl)oxy)phenoxy)-3-((2-hydroxyethyl)



### amino)propan-2-ol (YT-6-2)

To a solution of B3 (10 g, 25.1 mmol) and 2-aminoethanol (3.07 g, 50.3 mmol) in MeOH (100 mL) was stirred overnight at 50°C. The mixture was concentrated. Another 20 g batch was carried out as the above procedure. The crude was purified by prep-HPLC, then concentrated to remove acetonitrile, and added the NaHCO<sub>3</sub> saturated solution to adjust pH to 7-8. The solution was filtered and washed by water 3 times to give YT-6-2 ((R)-1-(3,4-bis((4-fluorobenzyl)oxy)phenoxy)-3-((2-hydroxyethyl)amino)propan-2-ol, 10 g, 86.7%) as a white solid. <sup>1</sup>H-NMR (CDCl<sub>3</sub>, 400 MHz) δ (ppm) 7.4-7.33 (m, 4H), 7.06-6.99 (m, 4H), 6.83 (d, J = 8.8 Hz, 1H), 6.57 (d, J = 2.8 Hz, 1H), 6.38 (dd, J = 9.2, 3.2 Hz, 1H), 5.04 (s, 2H), 4.99 (s, 2H), 4.07 (brs, 1H), 3.9 (d, J = 4.4 Hz, 2H), 3.7 (s, 2H), 2.88-2.77 (m, 7H); ESI-MS Calcd m/z for C<sub>25</sub>H<sub>27</sub>F<sub>2</sub>NO<sub>5</sub> [M+H]<sup>+</sup> 459.18 Found 460.90.

### **Scheme 3. Synthesis of (R)-1-(4-(benzyloxy)-3-phenethoxyphenoxy)-3-(isopropylamino)propan-2-ol (YOK-1204)**

#### 3.1. Synthesis of 4-(benzyloxy)-3-hydroxybenzaldehyde (C1)

To a solution of 3,4-dihydroxybenzaldehyde (A1, 20 g, 145 mmol) and (bromomethyl)benzene (24.8 g, 145 mmol) in acetonitrile (400 mL) was add NaHCO<sub>3</sub> (14.6 g, 174 mmol) at 25°C. The mixture was stirred overnight at 80°C. The reaction was concentrated. The residue was quenched with 1N HCl and extracted with ethyl acetate. The organic layer was washed with brine, dried over Na<sub>2</sub>SO<sub>4</sub>, filtered and concentrated. The residue was purified by column chromatography on silica gel, eluted with ethyl acetate/petroleum ether (1:20~1:10) to afford 4-(benzyloxy)-3-hydroxybenzaldehyde (C1, 10 g, 30%) as a white solid.

<sup>1</sup>H-NMR (DMSO-*d*<sub>6</sub>, 400 MHz)  $\delta$  (ppm) 9.76 (s, 1H), 9.66 (s, 1H), 7.49-7.48 (m, 2H), 7.42-7.34 (m, 4H), 7.29 (d, *J* = 2.0 Hz, 1H), 7.20 (d, *J* = 8.4 Hz, 1H), 5.23 (s, 2H); ESI-MS Calcd *m/z* for C<sub>14</sub>H<sub>12</sub>O<sub>3</sub> [M+H]<sup>+</sup> 229.20 Found 229.08.

### 3.2. Synthesis of 4-(benzyloxy)-3-phenethoxybenzaldehyde (C2)

To a solution of 4-(benzyloxy)-3-hydroxybenzaldehyde (C1, 10 g, 43.9 mmol) and (2-bromoethyl)benzene (9.71 g, 52.6 mmol) in dimethylformamide (100 mL) was added Cs<sub>2</sub>CO<sub>3</sub> (43 g, 132 mmol). The mixture was stirred at 80°C overnight. The mixture was added water and extracted with ethyl acetate. The organic layer was washed with brine, dried over Na<sub>2</sub>SO<sub>4</sub>, filtered and concentrated. The residue was purified by column chromatography on silica gel, eluted with ethyl acetate/petroleum ether (20:1~10:1) to afford 4-(benzyloxy)-3-phenethoxybenzaldehyde (C2, 3.7 g, 25%). <sup>1</sup>H-NMR (CDCl<sub>3</sub>, 400 MHz)  $\delta$  (ppm) 9.83 (s, 1H), 7.46-7.25 (m, 12H), 7.02 (d, *J* = 7.6 Hz, 1H), 5.22 (s, 2H), 4.31 (t, *J* = 6.8 Hz, 2H), 3.18 (t, *J* = 6.8 Hz, 2H); ESI-MS Calcd *m/z* for C<sub>22</sub>H<sub>20</sub>O<sub>3</sub> [M+H]<sup>+</sup> 333.20 Found 333.14.

### 3.3. Synthesis of 4-(benzyloxy)-3-phenethoxyphenol (C3)

To a solution of 4-(benzyloxy)-3-phenethoxybenzaldehyde (C2, 3.7 g, 11.1 mmol) in dichloromethane (40 mL) was added meta-chloroperoxybenzoic acid (2.9 g, 16.7 mmol) in portions. The mixture was stirred at RT for 2 h. The mixture was washed with saturated NaHCO<sub>3</sub> solution, and concentrated. The mixture was dissolved in methanol (25 mL) and added 5 N KOH (2.5 mL, 12.3 mmol). The mixture was stirred at RT for 1 h. The mixture was added ice water and filtered. The solid was concentrated to afford 4-(benzyloxy)-3-phenethoxyphenol (C3, 3.4 g, 96%). <sup>1</sup>H-

NMR (DMSO-d<sub>6</sub>, 400 MHz)  $\delta$  (ppm) 9.01 (s, 1H), 7.37-7.21 (m, 10H), 6.80 (d, J = 8.8 Hz, 1H), 6.43 (s, 1H), 6.22 (dd, J = 2.4, 8.4 Hz, 1H), 4.87 (s, 2H), 4.14 (t, J = 6.8 Hz, 2H), 3.03 (t, J = 6.4 Hz, 2H); ESI-MS Calcd m/z for C<sub>21</sub>H<sub>20</sub>O<sub>3</sub> [M+H]<sup>+</sup> 321.80 Found 321.14.

#### 3.4. Synthesis of (R)-2-((4-(benzyloxy)-3-phenethoxyphenoxy)methyl)oxirane (C4)

To a solution of 4-(benzyloxy)-3-phenethoxyphenol (C3, 3.4 g, 10.6 mmol) in ethanol (50 mL) was added KOH (0.7 g, 12.8 mmol) and H<sub>2</sub>O (5 mL). The mixture was added (R)-2-(chloromethyl)oxirane (2.9 g, 31.9 mmol). The mixture was stirred at 30°C overnight. The mixture was added water and filtered. The solid was concentrated to give (R)-2-((4-(benzyloxy)-3-phenethoxyphenoxy)methyl)oxirane (C4, 3.6 g, 90%). <sup>1</sup>H-NMR (DMSO-d<sub>6</sub>, 400 MHz)  $\delta$  (ppm) 7.41-7.19 (m, 10H), 6.9 (d, J = 8.8 Hz, 1H), 6.65 (d, J = 2.8 Hz, 1H), 6.42 (dd, J = 2.4, 8.8 Hz, 1H), 4.93 (s, 2H), 4.26-4.18 (m, 3H), 3.77-3.72 (m, 1H), 3.3-3.27 (m, 1H), 3.04 (t, J = 6.4 Hz, 2H), 2.82 (t, J = 4.8 Hz, 1H), 2.69-2.67 (m, 1H); ESI-MS Calcd m/z for C<sub>24</sub>H<sub>24</sub>O<sub>4</sub> [M+H]<sup>+</sup> 377.10 Found 377.17.

#### 3.5. Synthesis of (R)-1-(4-(benzyloxy)-3-phenethoxyphenoxy)-3-(isopropylamino)propan-2-ol (YOK-1204)

The mixture of (R)-2-((4-(benzyloxy)-3-phenethoxyphenoxy)methyl)oxirane (C4, 3.6 g, 9.6 mmol) and propan-2-amine (2.8 g, 47.9 mmol) in methanol (100 mL) was stirred overnight at 50°C. The reaction mixture was concentrated and purified by chromatography (dichloromethane/methanol=15/1) to give (R)-1-(4-(benzyloxy)-3-phenethoxyphenoxy)-3-(isopropylamino)propan-2-ol (YOK-1204, 1 g, 24%). <sup>1</sup>H-

NMR (DMSO-d<sub>6</sub>, 500 MHz)  $\delta$  (ppm) 7.37 – 7.25 (m, 9H), 7.21 (ddd,  $J$  = 7.2, 3.7, 2.1 Hz, 1H), 6.82 (d,  $J$  = 8.8 Hz, 1H), 6.56 (d,  $J$  = 2.8 Hz, 1H), 6.39 (dd,  $J$  = 8.8, 2.8 Hz, 1H), 4.91 (s, 2H), 4.13 (t,  $J$  = 6.7 Hz, 2H), 4.03 (t,  $J$  = 6.8 Hz, 1H), 3.86 (q,  $J$  = 7.2 Hz, 2H), 3.77 (q,  $J$  = 5.5 Hz, 2H), 3.00 (t,  $J$  = 6.7 Hz, 2H), 2.66 (m, 2H), 2.52 (dd,  $J$  = 10, 5 Hz, 1H), 0.96 (dd,  $J$  = 6.2, 2.8 Hz, 6H); <sup>13</sup>C-NMR (DMSO-d<sub>6</sub>, 125 MHz)  $\delta$  (ppm) 153.85, 149.66, 141.88, 138.56, 137.67, 129.07, 128.25, 128.20, 127.61, 127.49, 126.22, 116.28, 104.88, 101.91, 71.17, 71.08, 68.80, 68.30, 49.93, 48.29, 35.04, 22.75; HRMS Calcd  $m/z$  for C<sub>27</sub>H<sub>33</sub>NO<sub>4</sub> [M+H]<sup>+</sup> 436.2482 Found 436.2482.

#### **Scheme 4. Synthesis of 4-(3,4-bis(benzyloxy)phenyl)butan-1-ol (ATB1095)**

##### 4.1. Synthesis of methyl 4-(3,4-dimethoxyphenyl)butanoate (D1)

To a solution of 4-(3,4-dimethoxyphenyl)butanoic acid (1 g, 4.46 mmol) in MeOH (20 mL) was added H<sub>2</sub>SO<sub>4</sub> (0.5 mL) by dropwise manner. The mixture was refluxed for 8 hours. After the reaction was completed, the resulting mixture was cooled and evaporated to remove MeOH. The residue was dissolved in H<sub>2</sub>O (20 mL), added saturated NaHCO<sub>3</sub> aqueous solution to adjust pH 7 and extracted by dichloromethane (50 mL x 2). Organic layer was washed with 1 N NaOH aqueous solution, dried over anhydrous MgSO<sub>4</sub> and concentrated in vacuo to give D1 (methyl 4-(3,4-dimethoxyphenyl)butanoate, 1 g, 4.2 mmol, yield: 94%).

##### 4.2. Synthesis of methyl 4-(3,4-dihydroxyphenyl)butanoate (D2)

To a solution of D1 (1 g, 4.2 mmol) in dichloromethane (40 mL) was added 1 M BBr<sub>3</sub> in dichloromethane (21 mL, 21 mmol) at 0°C by dropwise manner. The mixture

was stirred at 0°C for 2 h. After reaction was completed, ice (30 g) was slowly added to the mixture and the mixture was stirred at room temperature for overnight. Organic layer was washed with brine, dried over anhydrous  $\text{MgSO}_4$  and concentrated under reduced pressure. The residue was purified by flash column chromatography (n-hexane/ethyl acetate = 5/1) to give D2 (methyl 4-(3,4-dihydroxyphenyl)butanoate, 0.34 g, 1.62 mmol, yield: 39%). ESI-MS Calcd  $m/z$  for  $\text{C}_{11}\text{H}_{14}\text{O}_4$   $[\text{M}+\text{H}]^+$  211.10 Found 211.

#### 4.3. Synthesis of methyl 4-(3,4-bis(benzyloxy)phenyl)butanoate (D3)

To a solution of D2 (0.34 g, 1.62 mmol) in anhydrous DMF (8 mL) were added benzyl bromide (0.58 mL, 4.86 mmol) and  $\text{K}_2\text{CO}_3$  (1.01 g, 7.29 mmol). The mixture was stirred at 80°C for 4 h. After the reaction was completed, the mixture was cooled and poured into  $\text{H}_2\text{O}$  (50 mL). The resulting solid was collected and dissolved with dichloromethane (30 mL). The organic layer was washed with 10% NaOH aqueous solution (30 mL x 2), dried over anhydrous  $\text{MgSO}_4$  and concentrated in vacuo to give D3 (methyl 4-(3,4-bis(benzyloxy)phenyl)butanoate, 0.39 g, 1 mmol, yield: 62%). ESI-MS Calcd  $m/z$  for  $\text{C}_{25}\text{H}_{26}\text{O}_4$   $[\text{M}+\text{H}]^+$  391.19 Found 391.

#### 4.4. Synthesis of 4-(3,4-bis(benzyloxy)phenyl)butan-1-ol (ATB1095)

To a solution of D3 (0.39 g, 1 mmol) in anhydrous THF (5 mL) was added 2.5 M  $\text{LiAlH}_4$  in THF (0.6 mL, 1.5 mmol) at 0°C by dropwise manner. The mixture was stirred at 0°C for 2 h. After the reaction was completed, the mixture was quenched by  $\text{H}_2\text{O}$  (0.1 mL), 2 N NaOH (0.1 mL) and  $\text{H}_2\text{O}$  (0.3 mL) sequentially added. The resulting mixture was dried over anhydrous  $\text{MgSO}_4$  and celite® filtered. The residue

was purified by flash column chromatography (n-hexane/ethyl acetate = 2/1) to give ATB1095 (4-(3,4-bis(benzyloxy)phenyl)butan-1-ol, 0.22 g, 0.61 mmol, yield: 61%) as a colorless oil. <sup>1</sup>H-NMR (DMSO-d<sub>6</sub>, 600 MHz) δ (ppm) 1.37-1.41 (m, 2H), 1.51-1.56 (m, 2H), 2.46-2.48 (m, 2H), 3.37-3.40 (m, 2H), 4.37 (t, J = 5.4 Hz, 1H), 5.07 (s, 2H), 5.10 (s, 2H), 6.68 (dd, J = 7.8 Hz, 1.8 Hz, 1H), 6.91 (d, J = 1.8 Hz, 1H), 6.93 (d, J = 7.8 Hz, 1H), 7.29-7.33 (m, 2H), 7.35-7.39 (m, 4H), 7.42-7.46 (m, 4H). ESI-MS Calcd m/z for C<sub>19</sub>H<sub>25</sub>FN<sub>2</sub>O<sub>3</sub> [M+H]<sup>+</sup> 362.19 Found 363.00, [M-OH]<sup>+</sup> + 345.

## **Scheme 5. Synthesis of 2-((3,4-diphenethoxybenzyl)amino)ethan-1-ol (YTK-2205)**

### 5.1. Synthesis of 3,4-diphenethoxybenzaldehyde (E1)

To a solution of A1 (3,4-dihydroxybenzaldehyde, 20.0 g, 144 mmol) in THF (200 mL) was added 2-phenylethanol (43.9 g, 360 mmol) and PPh<sub>3</sub> (94.4 g, 360 mmol). DIAD (81.5 g, 403 mmol) was added to the solution at 0°C under N<sub>2</sub>. The mixture was stirred overnight at 65°C. The reaction mixture was added to water (100 mL) and extract with EA (100 mL x3). The combined organic layers were dried over Na<sub>2</sub>SO<sub>4</sub> and concentrated. The crude was purified by column chromatography on silica gel (PE/EA=30:1) to give E1 (3,4-diphenethoxybenzaldehyde, 46 g, 92.2% yield) as a yellow oil. <sup>1</sup>H-NMR (DMSO-d<sub>6</sub>, 400 MHz) δ (ppm) 9.81 (s, 1H), 7.53-7.17 (m, 13H), 4.28-4.20 (m, 4H), 3.08-3.04 (m, 4H).

### 5.2. Synthesis of 2-((3,4-diphenethoxybenzyl)amino)ethan-1-ol (YTK-2205)

To a solution of E1 (20 g, 57.8 mmol) in MeOH (200 mL) was added 2-aminoethanol (3.9 g, 63.9 mmol). The mixture was stirred for 2 h at 65°C. NaBH<sub>4</sub> (2.41 g, 63.9

mmol) was added at RT. The reaction mixture was stirred overnight at 50°C. The above solution was poured into water. The solution was extracted with EtOAc (100 mL x 3). The combined organic layers were washed with brine, dried over Na<sub>2</sub>SO<sub>4</sub>, and concentrated. The crude was purified by column chromatography on silica gel (DCM/MeOH=20:1) to give YTK-2205 (2-((3,4-diphenethoxybenzyl)amino)ethanol, 17 g, 75% yield) as a yellow solid. <sup>1</sup>H-NMR (DMSO-d<sub>6</sub>, 400 MHz): δ 7.21-7.35 (m, 10 H), 6.78-6.95 (m, 3 H), 4.43-4.43 (br, 1 H), 4.09-4.14 (m, 4 H), 3.61 (s, 2 H), 3.44-3.47 (m, 2 H), 2.99-3.04 (m, 4 H), 2.53-2.56 (m, 2 H); ESI-MS Calcd m/z for C<sub>25</sub>H<sub>29</sub>NO<sub>3</sub> [M+H]<sup>+</sup> 392.2 Found 391.9 and 392.9.

**Scheme 6. Synthesis of (R)-1-(2-((3-(3,4-bis(benzyloxy)phenoxy)-2-hydroxypropyl)amino)ethyl)guanidine (YOK-1109)**

6.1. Synthesis of tert-butyl (R)-2-((3-(3,4-bis(benzyloxy)phenoxy)-2-hydroxypropyl)amino)ethyl)carbamate (F2)

To a solution of F1 ((R)-2-((3,4-bis(benzyloxy)phenoxy)methyl)oxirane, 500 mg, 1.38 mmol) in MeOH (10 mL) were added tert-butyl 2-aminoethylcarbamate (442 mg, 2.76 mmol). The mixture was stirred at 50°C for 10 h. Then the reaction was concentrated to afford F2 (tert-butyl (R)-2-((3-(3,4-bis(benzyloxy)phenoxy)-2-hydroxypropyl)amino)ethyl)carbamate, 0.6 g) as a yellow solid without further purification.

6.2. Synthesis of (R)-1-((2-aminoethyl)amino)-3-(3,4-bis(benzyloxy)phenoxy)propan-2-ol (F3)

To a solution of F2 (600 mg, 1.15 mmol) in MeOH (6 mL) was added MeOH/HCl (3 mL, 3N). The mixture was stirred at room temperature for 4 hrs. Then the solution was removed solvent by evaporated in a vacuum. The residue was diluted with 10% MeOH in DCM and washed with aq. NaHCO<sub>3</sub>. The organic layer was dried over MgSO<sub>4</sub>, and concentrated to afford crude F3 ((R)-1-((2-aminoethyl)amino)-3-(3,4-bis(benzyloxy)phenoxy)propan-2-ol, 400 mg) as an off-white solid, which was used directly for next step.

### 6.3. Synthesis of (R)-1-(2-((3-(3,4-bis(benzyloxy)phenoxy)-2-hydroxypropyl)amino)ethyl)guanidine (YOK-1109)

To a solution of F3 (400 mg, 0.95 mmol) in DMF (5 mL) were added 1H-Pyrazole-1-carboxamide hydrochloride (553 mg, 3.8 mmol) and DIEA (0.3 g, 2.4 mmol). The mixture was stirred at 30°C for 12 h. Then the solution was removed solvent by evaporated in a high vacuum, and the residue was purified by pre-HPLC to afford YOK-1109 ((R)-1-(2-((3-(3,4-bis(benzyloxy)phenoxy)-2-hydroxypropyl)amino)ethyl)guanidine, 22 mg 5% yield) as a white solid. <sup>1</sup>H-NMR (DMSO-d<sub>6</sub>+D<sub>2</sub>O, 400 MHz): δ 7.43-7.36 (m, 10H), 6.98-6.96 (m, 1H), 6.67 (s, 1H), 6.46-6.45 (m, 1H), 5.12 (s, 2H), 5.05 (s, 2H), 4.08 (m, 1H), 3.89 (m, 2H), 3.48 (m, 2H), 3.20-3.06 (m, 4H); ESI-MS Calcd m/z for C<sub>26</sub>H<sub>32</sub>N<sub>4</sub>O<sub>4</sub> [M+H]<sup>+</sup> 465.5 Found 465.0 and 466.0

### **Immunofluorescence analysis**

Cells were cultured on coverslips and infected with Mtb-ERFP as described above. After the appropriate infection, cells were washed three times with PBS, fixed with



4% paraformaldehyde for 15 min, permeabilized with 0.25% Triton X-100 (Sigma-Aldrich) for 10 min, and incubated with primary antibodies for 2 h at room temperature or overnight at 4°C. Cells were washed with PBS to remove excess primary antibodies and then incubated with secondary antibodies for 1 h at room temperature. Each experiment was completed on duplicate coverslips and the results are expressed as the mean and standard deviation. Images of dynamic cell co-localization were recorded as vertical z-stacks. LAS X small 2.0 and Adobe Photoshop 7 (Adobe Systems) were used for image processing.

### **Colony-forming unit (CFU) assay**

Wild type (WT) strain of *Salmonella enterica* serovar Typhimurium (*S. Typhimurium*) strains was utilized for the study. A single colony of *S. Typhimurium* was grown overnight at 37°C in the shaking incubator. Secondary culture (5% inoculum) was grown for three hours in microaerophilic conditions. HeLa or RAW264.7 cell lines were infected at a multiplicity of infection (MOI) of 10 for 30 minutes. The infected cells were washed with DPBS and the cells were treated with media containing 100 µg/ml gentamycin (Thermo Fisher Scientific, 15710064) for one hour to exterminate the extracellular bacteria. The media was exchanged with fresh medium including 10 µg/ml gentamycin. The cells were further cultured with and without the chemical p62 ligand and incubated for the indicated time in figure legends. Finally, the mammalian cells were lysed using lysis buffer (0.1% Triton X-100, 1X Phosphate Buffered Saline (PBS; Welgene, LB 204-01)). The intracellular *S. Typhimurium* containing lysates were serially diluted and spread on the Luria broth (LB) agar plate.

After overnight incubation at 37°C, the CFU was determined. For intracellular bacterial viability, cells were infected with Mtb for 4 h. Cells were washed with PBS and lysed in distilled water to release the intracellular bacteria. The harvested bacteria were then plated in Middlebrook 7H10 agar with OADC and incubated for 2-3 weeks, and colonies were counted.

### **RNA interference assay**

Reagents for siRNA silencing were purchased from Life Technologies. Transfection was performed at a final concentration of 40 nM using Lipofectamine RNAiMAX reagent (Invitrogen, 13778150) according to the manufacture's protocol. Approximately 48 h after siRNA silencing, cells were harvested for immunoblotting and immunocytochemical analyses. The sequences of pre-designed siRNAs against *SQSTM1* (Bioneer, 4392420; ID 23628) and *UBB* (Bioneer) are as follows: si*SQSTM1* (sense, 5'-GCCUGUUCGAAAGCGCAAA-3'; antisense, 5'-UUUGCGCUUUCGAA CAGGC-3'), si*UBB* (sense, 5'-CCAGCAGAGGCUCAUCUUU-3'; antisense, 5'-AAAGAUGAGCCUCUGCUGG-3'). The sequences of *ATG5* and *MAP1LC3B* siRNAs (Genolution) are as follows: *ATG5* (sense, 5'-CAGUAUCAGACACGAUCAU-3'; antisense, 5'-AUGAUCGUGUCUGA UACUG-3'), *MAP1LC3B* (sense, 5'-CCAAGAUGCCAGUGAUUUAUUU-3'; antisense, 5'-AUAAUCACUGGGAUCUUGGUU-3').

### **Immunoblotting analysis**

Cells were washed with cold PBS and lysed directly with 1X Laemmli sample buffer (Bio-Rad, 161-0737) or with RIPA buffer (50 mM Tris-HCl, 150 mM NaCl, 1% NP-40, 1% sodium deoxycholate, and 0.1% SDS; Biosesang, RC2002) containing freshly prepared protease inhibitor cocktail (Sigma-Aldrich, P8340) and phosphatase inhibitor (Sigma-Aldrich, 31167051-1). Lysates were centrifuged at 18,500 x g for 20 min at 4°C, and the supernatants were used for immunoblotting. Protein concentrations were measured using the BCA protein assay kit (Pierce, 23225). The samples were diluted with 4X Laemmli sample buffer (65.8 mM Tris-HCl, pH 6.8, 26.3% [w:v] glycerol, 2.1% SDS, 0.01% bromophenol blue; Bio-Rad, 161-0737) or in lithium dodecyl sulfate (LDS) sample buffer (Invitrogen, NP0007) with a reducing reagent, followed by heating for 5 min at 95°C. Whole-cell lysates were separated by sodium dodecyl sulfate (SDS)-polyacrylamide gel electrophoresis and transferred to polyvinylidene difluoride membranes (Millipore, IPVH00010). Blocking was done using PBS-T (20 mM Tris-HCl, pH 7.5, 150 mM NaCl, and 0.05% [v:v] Tween 20 [Bio-Rad, 170-6531]) containing 5% BSA (Biosesang, AC1025) for 1 h at room temperature, and the membrane was incubated with primary antibodies diluted with the blocking solution for overnight at 4°C. Secondary IgG-HRP antibodies were incubated for 1 h at room temperature.

### **Molecular docking studies**

For the docking study, five novel compounds were generated and optimized in Cresset Flare software. The available crystal structure of the p62 ZZ domain (PDB ID: 6MIU) was downloaded from Protein Data Bank (<https://www.rcsb.org>). Protein

preparation was carried out in Cresset module Flare software. Hydrogen and 3D protonation were carried out on the target protein and minimized for the active site residues. Docking experiments were performed by using Cresset Flare software in accurate mode and default settings.

### **Affinity-isolation assays of YT-6-2**

Plasmids expressing p62 wild type and ZZ point mutant (D147K) constructs were transiently transfected into p62<sup>-/-</sup> HeLa cells using Lipofectamine 2000. After 24 h, trypsinized cells were collected in a growth medium and centrifuged. The cell pellets were resuspended in a hypotonic buffer (10 mM HCl, 1.5 mM MgCl<sub>2</sub>, 10 mM HEPES, pH 7.9) and incubated in ice for 30 min. The cell suspensions were subjected to ten freeze-thaw cycles, followed by centrifugation at 12,000 × g at 4°C for 15 min. For the affinity-isolation assay, biotinylated YT-6-2 was incubated with streptavidin agarose resin (272 µg of compound per ml settled resin; Thermo Fisher Scientific, 20359). The X-peptide beads were diluted in five volumes of PBS and incubated overnight at 4°C. The beads were centrifuged at 1000 × g for 3 min and washed three times in an equal volume of PBS. Soluble p62<sup>-/-</sup> HeLa cell extracts containing 500 µg of total protein were diluted in 500 µl binding buffer (0.05% Tween 20, 10% glycerol, 0.2 M KCl, 20 mM HEPES, pH 7.9) and mixed with YT-6-2 conjugated beads (30 µl packed volume). The mixtures were incubated at 4°C for 1 h with gentle rotation. The beads were pelleted by centrifugation at 1000 × g for 3 min, washed five times with 500 µl of binding buffer at 4°C for 10 min, resuspended in 30 µl SDS sample buffer, and heated at 100°C for 5 min. Analysis was performed by SDS-

PAGE and immunoblotting.

### **Transmission electron microscopy (TEM)**

RAW264.7 cells were infected with *S. Typhimurium* for 30 min followed by incubation with 5  $\mu$ M YTK-A76 for 4 h. BMDMs were infected with Mtb for 4 h and treated with 5  $\mu$ M YTK-2205 for 18 h. The cells were scraped from the culture dish and pelleted by centrifugation at 3000 x g for 5 min. Pellets were resuspended in 2.5% glutaraldehyde in 0.1 M phosphate (pH 7.4) overnight at 4°C. Subsequently, 50 nm sections were cut and stained with uranyl acetate and lead citrate using the Reichert Ultracut S Ultramicrotome (Leica Microsystems) and FEI Vitrobot Mark IV (Thermo Scientific), respectively. Cell sections were examined using the JEOL JEM-1400 series 120 kV Transmission Electron Microscope at the Seoul National University Hospital Biomedical Research Institute.

### **Histology**

For histopathology, liver and lung tissues were fixed in 10% formalin and embedded in paraffin wax. The tissues were sectioned with 4  $\mu$ m thickness. Paraffin-embedded slides were freshly treated with Neo-Clear twice for 10 min each, followed by gradual rehydration in EtOH (100%, 90%, 80%, and 70%; 6 min each) and water for 20 min. The tissues were then stained with hematoxylin and eosin (H&E). H&E-stained sections were scanned with an Aperio digital pathology slide scanner (Leica) and imaged using an Aperio ScanScope® CS System.

## **Immunocytochemistry**

Autoclaved 22 mm<sup>2</sup> coverslips were placed in 24-well plates. HeLa cells were seeded  $2.5 \times 10^5$  cells/well and cultured overnight for further experiments. Cells were infected with *S. Typhimurium* S14028 with an MOI of 10. Cells were fixed in 4% PFA in PBS, for 15 min at room temperature. After washing twice with PBS, the cells were incubated for 1 h in blocking solution (5% bovine serum albumin and 0.3% Triton X-100 in PBS). The samples were incubated with primary antibodies overnight at 4°C and secondary antibodies were incubated at room temperature. After washing out secondary antibodies with PBS, the samples were mounted on a cover slide with the mounting solution. Confocal images were taken with a Zeiss LSM 700 laser scanning confocal microscope equipped with Zeiss C-Apochromat 60x (1.2 NA) and 40x (1.2 NA) water immersion lens and analyzed using ZEN (black edition) 2012 SP5 software (Zeiss). Using the ZEN software, z-stacks of images covering the entire cell thickness were acquired and projected maximally. Image processing and annotation were done with Adobe Photoshop, Adobe Illustrator, and Fiji software.

## **Flow cytometry**

BMDMs were analyzed by flow cytometry for phagocytosis using an ACEA NovoCyte flow cytometer as indicated by the manufacturer. BMDMs were infected with Mtb-ERFP for 2 hours and treated with the p62 agonist. Flow cytometry data were collected and analyzed using De Novo software (CA, Glendale, USA).

## **MTT assay**

BMDMs were seeded in 96 well plates and treated with p62 agonists for 72 h treated with 3-(4,5-dimethylthiazol-2-yl)-2,5-diphenyltetrazolium bromide (MTT; Sigma-Aldrich, M5655) solution and incubated for 2 h. The medium was removed and cells were added DMSO to solubilize the crystals. The absorbance was measured with a reader spectrophotometer (Bio-Tek Synergy TH, Winooski, VT, USA) at 570 nm, using 690 nm as a reference.

## **Quantification and statistical analysis**

All experiments were repeated at least three times and all data are presented as the mean  $\pm$  SD or  $\pm$  SED. In most data, two-tailed unpaired t-test (for parametric data) or Mann–Whitney U-test (for nonparametric data) were used for comparisons of two groups, and one-way analysis of variance (ANOVA; Dunnett’s test) was performed for comparisons of multiple groups. For comparison of the magnitude of changes in different conditions, two-way ANOVA with Bonferroni post-test was used. Statistical significance was determined as values of  $p < 0.05$  (\* $p < 0.05$ , \*\* $p < 0.01$ , \*\*\* $p < 0.001$ , \*\*\*\* $p < 0.0001$ , ns: not significant). For each experiment, sample size (n) was determined as stated in the figure legends. All statistical analyses were performed with Prism 8.2 software (GraphPad).

# Results

## **Counteractive crosstalk between *S. Typhimurium* and host cells via autophagy**

Several studies have characterized autophagic pathways in cells infected with bacteria [48], yet the role of p62-dependent selective autophagy as a host defense system remains poorly understood. As an initial step to explore autophagy as a target for antimicrobial drugs, I assessed autophagic flux in RAW264.7 and HeLa cells infected with the Gram-negative bacteria *S. Typhimurium*. Immunoblotting analyses showed that the synthesis of LC3 and its lipidation into LC3-II (Figure 4A) were strikingly suppressed in a manner depending on the multiplicity of infection (MOI) (Figure 4B and 4C) and time during 1-6 h post-infection (Figure 4D). In contrast to bacteria, host cells could robustly induce the synthesis and lipidation of LC3 (Figure 5A) and the formation of LC3-positive puncta (Figure 5B) in response to lipopolysaccharide (LPS), a pathogen-associated molecular pattern (PAMP). When cells were infected with *S. Typhimurium*, the activity of LC3 was tightly blocked at a basal level as evidenced by insensitivity to bafilomycin A<sub>1</sub>, an inhibitor of the lysosomal V-ATPase (Figure 6A). In addition, the basal autophagy flux of host cells was dramatically reduced when the cells were infected with bacteria (Figure 6B). These results suggest that the suppression of autophagic pathways is essential for the life cycle of *S. Typhimurium*.



Next, I further monitored the remaining autophagic activities in cells infected with *S. Typhimurium*. Quantitative real-time PCR (RT-qPCR) showed increased transcription of autophagy-related genes such as ATG9B, WIPI1, TMEM74, ULK2, and DRAM1 (Figure 7). When visualized using immunostaining analyses, bacterial membranes were associated with LC3-positive autophagic membranes (Figure 8) as well as various autophagic receptors such as p62, NBR1, OPTN, and CALCOCO2 with distinct spatiotemporal patterns (Figure 9). Consistently, the intracellular growth of *S. Typhimurium* was markedly facilitated by knockdown of SQSTM1 (Figure 10), LC3B, or ATG5 (Figure 11). Moreover, the protein level of p62 and OPTN increased upon bacterial infection as compared with TAX1BP1, and CALCOCO2 (Figure 12). A similar induction was observed with mRNA expression of autophagy receptors including p62 and OPTN (Figure 13). These results suggest that the infected cells retain residual autophagic activities to degrade intracellular bacteria, providing p62-dependent selective autophagy as a drug target against a broad range of pathogenic bacteria.

### **Development of small molecule agonists that exert antimicrobial efficacy**

Previous studies show small-molecule ligands including YTK-1105 and YOK-1104 that bind to the ZZ domain of p62 [77, 78]. To screen antimicrobial agents with high selectivity and efficacy, I used approximately 30 derivatives of those initial compounds that confirmed by 3D structure modeling of the p62 ZZ domain associated with SAR (structure-activity relationship). The optimization processes first focused on the activity to induce self-oligomerization of p62 and to induce the

synthesis and lipidation of LC3. Following the initial screening, I assessed the antimicrobial efficacy of the resulting derivatives in the macrophage RAW264.7 and HeLa cells infected with *S. Typhimurium* by using colony-forming unit (CFU) assays. This screening yielded five compounds (YTK-A76, YT-6-2, YOK-1204, YTK-2205, and YOK-1109) with high antimicrobial efficacy in cultured cells (Figure 14). In CFU assays of RAW264.7 cells, these agonists exhibited antimicrobial efficacy in a manner depending on the dose, time, and MOI (Figure 15). The efficacy was reproduced in various cell lines such as J774A.1, THP-1, and BMDMs macrophage cell (Figure 16) as well as the HCT116 and HeLa epithelial cancer cells (Figure 17).

To rule out the possibility that p62 agonists directly kill intracellular bacteria, I performed disk diffusion assays (Figure 18A). As expected, antibiotics such as ampicillin, kanamycin, and gentamicin effectively killed *S. Typhimurium*, and the zone of inhibition became larger in a dose-dependent manner. In contrast, p62 agonists did not form such a zone of inhibition (Figure 18A). Moreover, bacteria normally grew in the growth medium containing as high as 15  $\mu$ M of p62 agonists (Figure 18B). During these experiments, the viability of host cells also was not significantly affected at the concentrations used for CFU assays (Figure 19). Finally, to rule out the possibility that p62 agonists affect bacterial entry, I measured the number of intracellular bacteria at 1 hpi following pretreatment of p62 agonists. No difference was observed (Figure 20). These results confirm that p62 agonists exert antimicrobial efficacy by modulating the function of host cells.

In the docking simulation study, the identified compounds located in the position where the first and second residues of N-degron bound (Figure 21A). The

binding mode of YT-6-2 showed a hydrogen bond between the oxygen attached to the chiral center of YT-6-2 and the side chain of Asp147, which I speculated that plays an important role in the binding. To determine the direct binding of the p62 agonist to the p62 ZZ domain, I performed pulldown assays using biotinylated YT-6-2 and full-length p62 (Figure 21B). The result showed that biotinylated YT-6-2 bound wild-type p62 and that the binding was significantly reduced when a point mutation was introduced within the ZZ domain (D147K) (Figure 21B). To further support the selectivity of p62 agonists, I synthesized ATB1095 which lacks the essential amine group required for a hydrogen bond with the side chain of Asp147 (Figure 21C). As expected, this compound showed no antimicrobial effect (Figure 21D). These results suggest that p62 agonists exert their antimicrobial efficacy through specific hydrogen bonds to the ZZ domain of p62.

### **p62 agonists rescue autophagic activities from suppression by *S. Typhimurium***

To characterize the mode of action of p62 agonists, I assessed their activities to induce degradative flux via p62-dependent selective autophagy. Immunoblotting analyses showed that YTK-A76, YT-6-2, YTK-1204, YTK-2205, and YOK-1109 enhanced the synthesis and lipidation of LC3 via non-canonical pathway (Figure 22A) associated with the increases in LC3<sup>+</sup> autophagic membranes, most of which colocalized with p62<sup>+</sup> puncta (Figure 23). Cells treated with p62 agonists produced excessive lipidated LC3 which was attributed to the activation of autophagic flux (Figure 22B). As an alternative assay, I also monitored the ratio of autophagosomes

and autolysosomes in the macrophage BMDMs using a retrovirus expressing the mCherry-EGFP-LC3B fusion. The treatment of p62 agonists markedly increased the number of autolysosomes (mCherry<sup>+</sup> EGFP<sup>+</sup>, red) (Figure 24). When the cells were co-treated with p62 agonists and bafilomycin A<sub>1</sub>, autophagosomes (mCherry<sup>+</sup> EGFP<sup>+</sup>, yellow) failed to turn into autolysosomes (Figure 24). These results demonstrate that p62 agonists enhance the degradative flux of autophagic cargoes.

Next, I determined whether p62 agonists are capable to rescue autophagic flux from suppression by *S. Typhimurium*. Indeed, p62 agonists restored the synthesis and lipidation of LC3 to normal levels in HeLa cells (Figure 25A) and BMDMs (Figure 25B) infected with *S. Typhimurium*. Autophagic flux assays using NH<sub>4</sub>Cl showed that the LC3 induction is attributed to the activation of autophagic flux (Figure 25C). In sharp contrast, rapamycin, an inducer of mTOR (mammalian target of rapamycin)-modulated core autophagic pathways, exhibited no such efficacy (Figure 26). These results suggest that p62 agonists exert antimicrobial efficacy via a non-canonical pathway and are independent of rapamycin-modulated bulk autophagy.

### **p62 agonists exert antimicrobial efficacy by binding to the ZZ domain of p62**

To further validate the selectivity of p62 agonists in therapeutic efficacy, I examined the activity of autophagy with ATB1095. Indeed, ATB1095 exhibited no detectable activity to induce the synthesis and lipidation of LC3 (Figure 21E). Moreover, CFU assays showed that ATB1095 and another negative control compound, ATB1094,

failed to inhibit the infectivity of *S. Typhimurium* in RAW264.7 cells (Figure 21D). These results verify the chemical selectivity of p62 agonists in therapeutic efficacy.

Next, I determined the binding specificity of YTK-A76 to the ZZ domain of p62. CFU assay with *S. Typhimurium* showed that the p62 agonist lost their efficacy when p62 was depleted using siRNA (Figure 27A). The p62 agonist regained antimicrobial efficacy when SQSTM1 knockdown HeLa cells were transfected to express wild-type p62 but not mutant p62 lacking ZZ domain that showed comparable transfection efficiency (Figure 27B). Furthermore, the activity of the p62 agonist to induce autophagosome biogenesis was dependent on the ZZ domain of p62 (Figure 24C).

I also tested whether p62 agonists induced the recruitment of p62 to *S. Typhimurium* using colocalization assays. Immunostaining analyses showed that colocalization of p62 with DAPI-positive *S. Typhimurium* markedly increased when cells were treated with p62 agonists (Figure 28). To test whether the activity to recruit p62 to the bacterial surface is dependent on the p62 ZZ domain, HeLa cells were depleted of p62 using siRNA to the 3'-untranslated region (3'-UTR) and subsequently engineered to express p62-EGFP or p62-ZZΔ-EGFP. When the cells were treated with YTK-A76, the colocalization between p62 and bacteria was ~70% with p62-EGFP and ~30% with p62-ZZΔ-EGFP (Figure 29). These results demonstrate that p62 agonists induce the recruitment of p62 to the membrane of intracellular *S. Typhimurium* through their binding to the p62 ZZ domain.

It is known that p62 undergoes self-polymerization via the PB1 domain and interacts with ubiquitin chains on cargoes via the UBA domain. To determine whether p62 oligomerization is required for the recruitment of p62 to ubiquitinated

bacterial membranes, p62 was depleted in HeLa cells using siRNA targeting its 3'-UTR, followed by transient expression of wild type p62-MYC and p62-PB1 $\Delta$ -MYC. Immunostaining analyses of the cells infected with *S. Typhimurium* showed that YTK-A76 induced the association of wild-type p62, but not p62-PB1 $\Delta$ -MYC, with bacteria (Figure 27). Likewise, mutant p62 lacking the UBA domain (p62-UBA $\Delta$ -MYC) failed to associate with bacteria (Figure 30). Consistently, when ubiquitin was depleted using siRNA targeting the *UBB* mRNA, YTK-A76 almost lost its ability to accelerate the p62 recruitment on the bacteria (Figure 31). This inability of p62 to associate with bacteria in both the absence and presence of p62 agonists was attributed to the loss of antimicrobial efficacy as determined by CFU assays (Figure 32). *S. Typhimurium* require the T3SS encoded by Salmonella pathogenicity island 1 (SPI-1) to deliver their effector proteins to cytosol of host. SPI-1 T3SS has been proposed to damage the Salmonella-containing vacuole (SCV) and allow subpopulation of *S. Typhimurium* to translocate from the vacuole to cytosol [79]. In order to find out whether the activated p62 recognize *S. Typhimurium* containing phagosome or cytosolic *S. Typhimurium*, RAW264.7 cells were infected with *S. Typhimurium* including WT,  $\Delta invG$ ,  $\Delta prgH$ ,  $\Delta prgJ$ , and  $\Delta prgK$ . While the p62 agonist induced 5-fold decrease in the number of intracellular WT, the compound induced less than 2-fold decrease in the number of the mutant strains (Figure 33). The result indicate that cytosolic fraction of *S. Typhimurium* are more likely to be recognized by the activated p62. These results suggest that p62 agonists facilitate the recruitment of p62 to the cytosolic bacteria through self-polymerization via the PB1 domain and the interaction with ubiquitin chains via the UBA domain.

## **p62 agonists induce xenophagy of *S. Typhimurium* by facilitating the target of the pathogens to the autophagosome**

To determine whether p62 agonists act as xenophagy-inducing drugs, I characterized the autophagic flux of host cells infected with *S. Typhimurium* (Figure 25). Immunostaining analyses of cells treated with p62 agonists revealed that the majority of p62-positive bacteria were also positive for LC3-positive autophagic membranes (Figure 8). The colocalization of p62<sup>+</sup> LC3<sup>+</sup> autophagic membranes with DAPI-positive *S. Typhimurium* markedly increased by p62 agonists (Figure 34). Moreover, the ability of p62 agonists to eradicate bacteria was almost completely blocked by the lysosomal inhibitor NH<sub>4</sub>Cl (Figure 35A). Consistently, knockdown of either ATG5 or LC3B abolished the activity of p62 agonists to induce degradation of intracellular bacteria (Figure 35B). The indispensable role of autophagy was further confirmed by the finding that the antimicrobial efficacy of p62 agonists was not significantly impaired when proteolytic flux via the UPS was inhibited by using the proteasome inhibitor MG132 (Figure 35C and 35D). Next, to obtain the decisive evidence for xenophagy, I performed transmission electron microscopy (TEM) in RAW264.7 cells. A significantly increased portion of bacteria were sequestered within autophagosomes in cells treated with YTK-A76 (Figure 36). These results demonstrate that p62 agonists induce the targeting of intracellular bacteria to autophagic membranes, leading to lysosomal degradation.

It is known that mTOR is a master regulator of various signaling pathways including bulk autophagy, the cell cycle, immune responses, and metabolism [80,

81]. I, therefore, tested whether pharmaceutical activation of autophagy using rapamycin also inhibits intracellular bacterial growth. In sharp contrast to p62 agonists, rapamycin exhibited no antimicrobial effect (Figure 37). Furthermore, unlike p62 agonists, rapamycin failed to enhance p62 recruitment of intracellular bacteria and bacterial targeting to autophagosomes (Figure 38). Resveratrol, a SIRT1 activator, also showed no antimicrobial activity against *S. Typhimurium* in RAW264.7 cells at 10-100  $\mu$ M (Figure 39). These results suggest that p62 agonists exert antimicrobial efficacy via selective autophagy and are independent of rapamycin-modulated canonical autophagic pathways.

### **p62 agonists enhance host innate immunity against Mtb and other pathogens via p62-mediated xenophagy**

Although xenophagy has been implicated in the lysosomal degradation of Mtb, it has not been fully understood about the underlying mechanisms and xenophagy-inducing reagents against Mtb [32]. To investigate whether the p62 agonists have anti-mycobacterial activities, I treated Mtb-infected BMDMs with YTK-A76, YT-6-2, YTK-2205, and YOK-1109. CFU assays showed that the growth rate of Mtb was dramatically inhibited at 5-10  $\mu$ M (Figure 40A). Silencing of *p62* in BMDMs significantly abrogated the antimicrobial response induced by YTK-2205 during Mtb infection (Figure 40B). During these experiments, the viability of both host cells and bacteria was not significantly influenced by p62 agonists at the concentrations used in this study (Figure 41A and 41B). Likewise, no difference was observed in the entry, i.e., phagocytosis of the Mtb in the absence and presence of p62 agonists



(Figure 41C). These results demonstrate the efficacy of p62 agonists to inhibit the infectivity of Mtb.

Next, I examined whether p62 agonists induce the autophagic targeting of Mtb. Co-immunostaining analyses showed that p62 agonists induced the colocalization of p62 and Mtb (Figure 42). Moreover, YTK-2205 treatment of Mtb-infected BMDMs led to a significant increase in colocalization between Mtb phagosomes and autophagosomes as compared with the control (Figure 43). Treatment of Mtb-infected BMDMs with YTK-2205 significantly upregulated the colocalization between Mtb phagosomes and lysosomes (Figure 44) suggesting that p62 agonists enhance the targeting of Mtb to autophagosomes that fuse with lysosomes for degradation. Furthermore, whereas mycobacteria were mostly detected within phagosomal structures in control cells, a significant portion of Mtb was sequestered in morphologically heterogeneous double-membrane vesicles that appeared to be autophagosomes in YTK-2205-treated BMDMs (Figure 45). Collectively, these data strongly suggest that p62 agonist-induced xenophagic flux is required for antimicrobial responses against Mtb infection.

Next, I also determined whether p62 agonists have antimicrobial efficacy against other bacteria including Gram-negative *E. coli* and the Gram-positive *S. pyogenes*. CFU assays (MOI of 10) showed that p62 agonists efficiently inhibited the growth of both strains (Figure 46). These results suggest that p62 has the potential as a drug target for a broad range of pathogenic bacteria.

**p62 agonists enhance xenophagy mediated host defense against**

## **pathogens in mice**

To validate the efficacy of p62 agonists in xenophagy, I orally infected C57BL/6 male mice with *S. Typhimurium* ( $10^6$  per mice), followed by i.p. injection of 20 mg/kg YTK-A76 or YTK-2205 once daily for 6 days. On day 7, the liver and spleen were harvested, and their extracts were used for CFU assays. When compared with the vehicle-treated group, mice injected with YTK-2205 showed approximately a 100-fold reduction in the number of bacteria (Figure 47A). Although the relative efficacy was weaker, a similar inhibition of bacterial infection was observed with YTK-A76 (Figure 47A). Histological examination of H&E-stained paraffin sections from livers revealed inflammation-associated damaged tissues in control mice. Such damages were barely observed in mice injected with YTK-2205 (Figure 47B). These results suggest that p62 agonists inhibit the infectivity of *S. Typhimurium* and reduce inflammation caused by bacterial infection.

Next, I investigated whether the administration of YTK-2205 or YT-6-2 promotes host antimicrobial defense during *Mtb* infection in mice. I infected mice with *Mtb* intranasally ( $5 \times 10^4$  CFU), followed by i.p. injection of 10 mg/kg YTK-2205 per 2 days (total 5 injections; for Figure 48A left) or 20 mg/kg YT-6-2 thrice per week (total 11 injections; for Figure 48A right). Notably, CFU assays of lung extracts showed that the bacterial burden was significantly reduced in mice treated with YTK-2205 or YT-6-2. Histopathological analyses also revealed significant decreases in the area of lung inflammation in mice treated with YT-6-2 (Figure 48B and 48C). Similarly, I infected mice with BCG ( $1 \times 10^7$  CFU) and administered YTK-2205 by i.p. injection. Treatment with YTK-2205 resulted in reduced BCG

burdens in the lungs (Figure 48A) and the number of granulomatous lung lesions and inflamed areas decreased (Figure 49B and 49C). Additionally, to explore whether p62 agonist amplified the host defense against multidrug-resistant (MDR) strain of Mtb, mice were infected with MDR-Mtb ( $5 \times 10^3$  CFU) and then treated with YT-6-2. Relative to a vehicle, injection of YT-6-2 significantly reduced the MDR-Mtb growth in the lungs (Figure 50). These results demonstrate the efficacy of p62 agonists to decrease bacterial load in the lungs and pulmonary inflammation in mice.

### **The p62 agonists inhibit the production of proinflammatory mediators *in vitro* and *in vivo*.**

Host defense against bacterial infection depends on the coordinated responses of inflammatory responses induced by innate and adaptive immune cells [82, 83]. Because p62 agonists reduced tissue pathology and enhanced host immune responses in *S. Typhimurium*– and Mtb-infected mice, I sought to evaluate the possible beneficial effects of the drugs on chronic inflammation associated with *S. Typhimurium* and Mtb disease. I, therefore, determined whether p62 agonists have efficacy to reduce the excessive production of cytokines in HeLa cells infected with *S. Typhimurium*. RT-qPCR analyses showed that YTK-A76 efficiently counteracted the mRNA induction of IL1B (interleukin 1 beta) and IL6 (Figure 51). Furthermore, to examine the role of p62 agonists in the modulation of inflammatory responses during Mtb infection, BMDMs infected with Mtb were treated with YTK-A76. The p62 agonists efficiently suppressed Mtb-induced upregulation of pro-inflammatory cytokines (Il6 and Il1b) and chemokine (Cxcl5) (Figure 52A). Consistently, in

peritoneal macrophages (PMs) and BMDMs infected with Mtb, YTK-2205 at 5  $\mu$ M inhibited Mtb-induced upregulation of the pro-inflammatory cytokines and chemokine (Figure 52B and 52C). Furthermore, BCG-infected mice injected i.p. with YTK-2205 produced a reduced level of Tnfa mRNA in the lung tissues compared to those in the vehicle group (Figure 53). Collectively, these results indicate that p62 agonists inhibit the expression of inflammatory mediators during pathogenic bacterial infections.

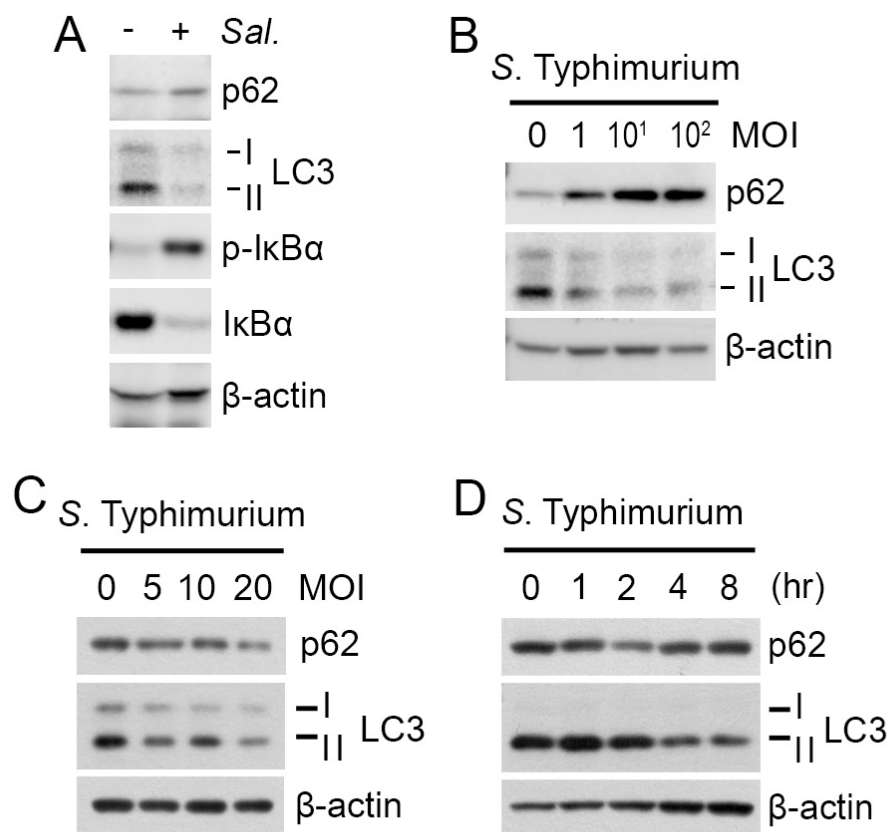


**Figure 4. *S. Typhimurium* infection decreases the protein level of LC3B of host cell MOI and time-dependently.**

While p62 protein level increased, LC3-I and II protein level were decreased upon *S. Typhimurium* infection. (A) RAW264.7 cells were infected with *S. Typhimurium* of MOI 10 for 6 h and the protein levels were analyzed by immunoblotting. (B) RAW264.7 cells were infected with *S. Typhimurium* of an indicated multiplicity of infection (MOI) for 6 h. (C) HeLa cells were infected with *S. Typhimurium* (MOI 10) for indicated time periods and analyzed by immunoblotting.

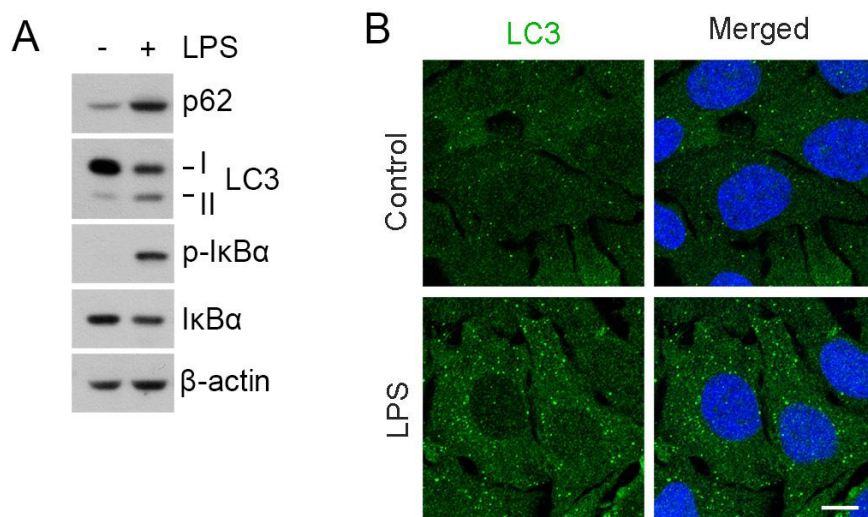


**Figure 5. Lipopolysaccharide (LPS) activates host cell autophagy.**

(A) RAW264.7 cells were treated with 100 ng/mL LPS for 6 h and subjected to immunoblotting analysis. LC3B-II and p62 protein levels were increased following LPS treatment. (B) Puncta formation assay of LC3 (green) in HeLa cells treated with 100 ng/mL LPS for 6 h. Scale bar: 10  $\mu$ m.

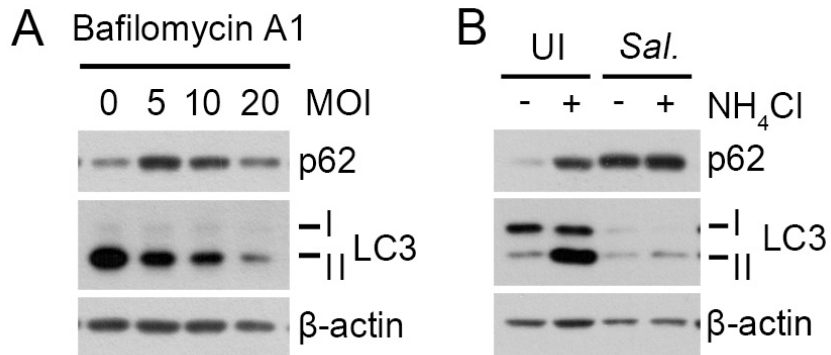


**Figure 6. *S. Typhimurium* infection decreases LC3B protein level and autophagic flux.**

(A) RAW264.7 cells were infected with *S. Typhimurium* of indicated MOI and the cells were treated with 100 nM bafilomycin A<sub>1</sub> for 4 h at 2 phi. (B) RAW264.7 cells were infected with *S. Typhimurium* for 5 h followed by 1 h 20 mM NH<sub>4</sub>Cl treatment for autophagy flux analysis.



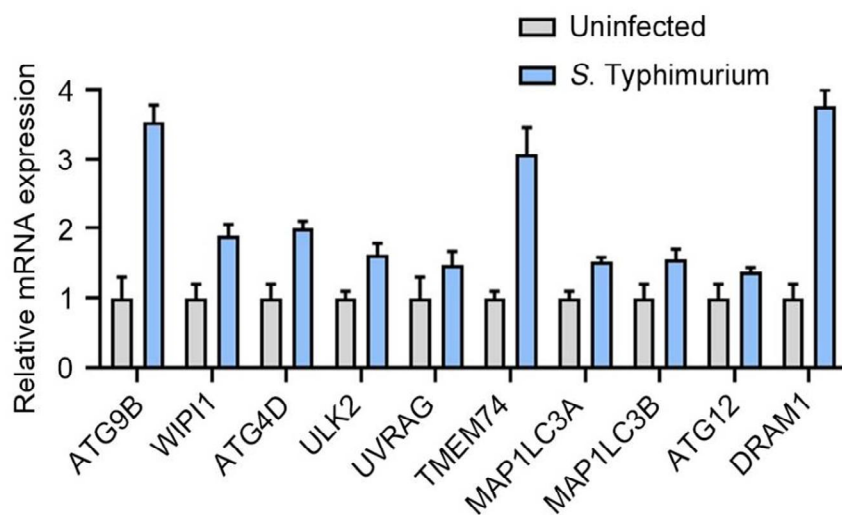


**Figure 7. Autophagy-related genes are upregulated by *S. Typhimurium* infection.**

Relative fold change in mRNA level of autophagy-related genes in uninfected and 6 h *S. Typhimurium*-infected HeLa cells were analyzed by RT-qPCR.

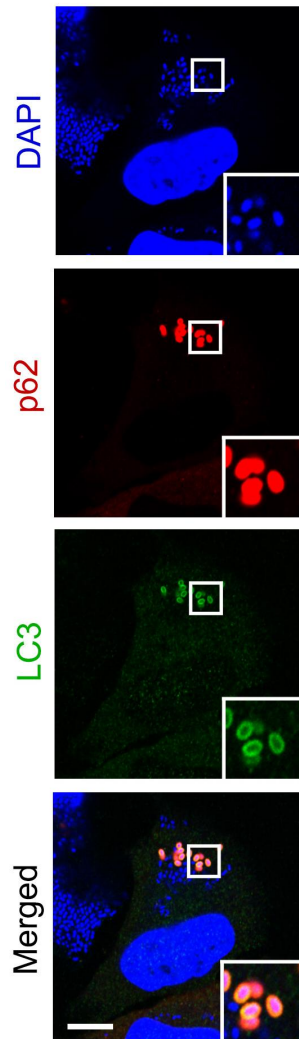


**Figure 8. Intracellular *S. Typhimurium* is associated with p62 and LC3B.**

Colocalization analysis between *S. Typhimurium* (blue), p62 (red), and LC3 (green) in HeLa cells infected with *S. Typhimurium* (MOI 10) for 6 h. The cytosolic DAPI signal represents intracellular *S. Typhimurium*. Scale bar: 10  $\mu$ m.

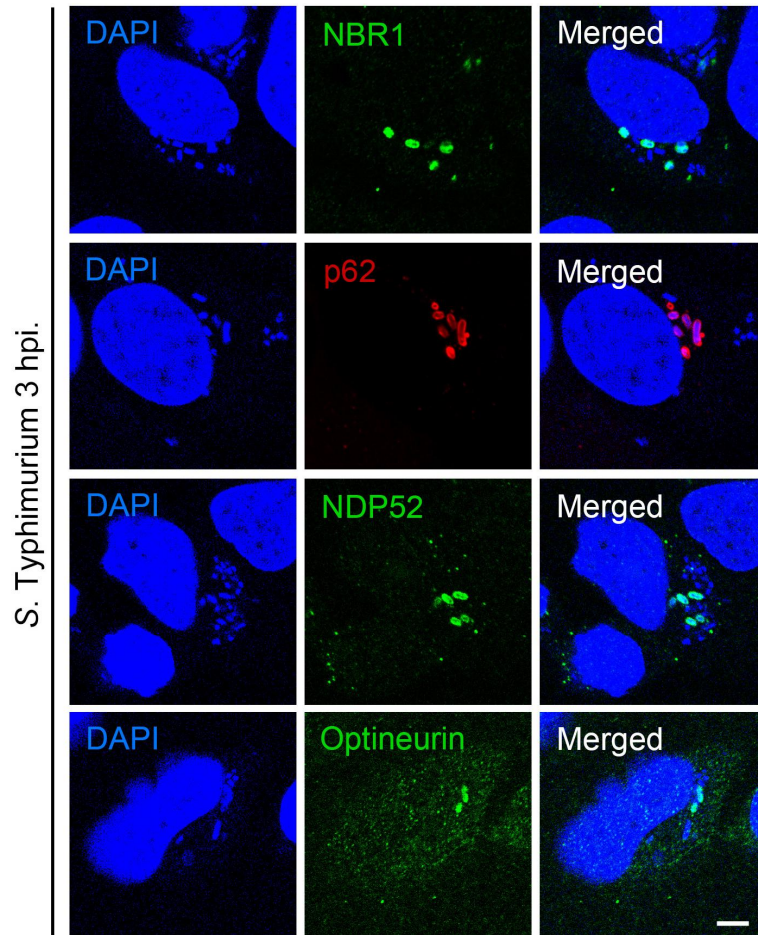


**Figure 9. Autophagy receptors are associated with intracellular *S. Typhimurium*.**

HeLa cells were infected with *S. Typhimurium* MOI of 10 for 3 h. After cell fixation, intracellular localization of autophagy receptors is analyzed by immunostaining. HeLa cells were stained with DAPI, anti-NBR1, anti-p62, anti-NDP52, and anti-Optineurin. Scale bar: 5  $\mu$ m.

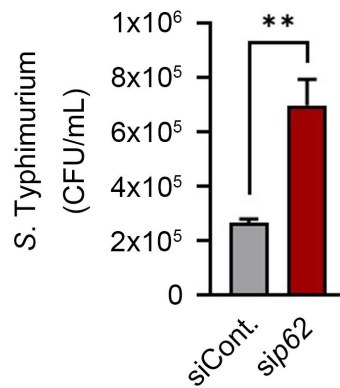


**Figure 10. p62 is required for growth inhibition of intracellular *S. Typhimurium*.**

A graph of CFU indicating the number of intracellular *S. Typhimurium* in HeLa cells transfected with siRNA control or siRNA targeting *SQSTM1*. HeLa cells were transfected with control or *SQSTM1* siRNA for 48 h followed by *S. Typhimurium* infection (MOI 10) for 6 h. Cell lysates were diluted and subjected to colony-forming unit assay.

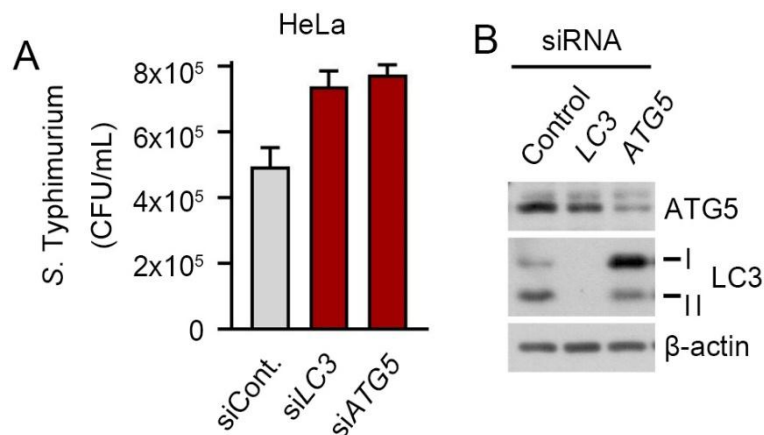


**Figure 11. Autophagosome biogenesis is required for growth inhibition of intracellular *S. Typhimurium*.**

(A) A Graph of CFU indicating intracellular *S. Typhimurium* in HeLa cells transfected with siRNA control or siRNA targeting *LC3* or *ATG5*. *S. Typhimurium* survived more in LC3 and ATG5 knockdown HeLa cells compared to those in control cells. (B) Immunoblotting analysis of siRNA-transfected cells for validation of protein depletion.



**Figure 12. Increase in the p62 and Optineurin protein level upon *S. Typhimurium* infection.**

HeLa cells were infected with *S. Typhimurium* MOI of 10 for 6 h. Cell lysates were subjected to immunoblotting with anti-p62, anti-NDP52, anti-Optineurin, anti-TAX1BP1, and anti-β-actin.

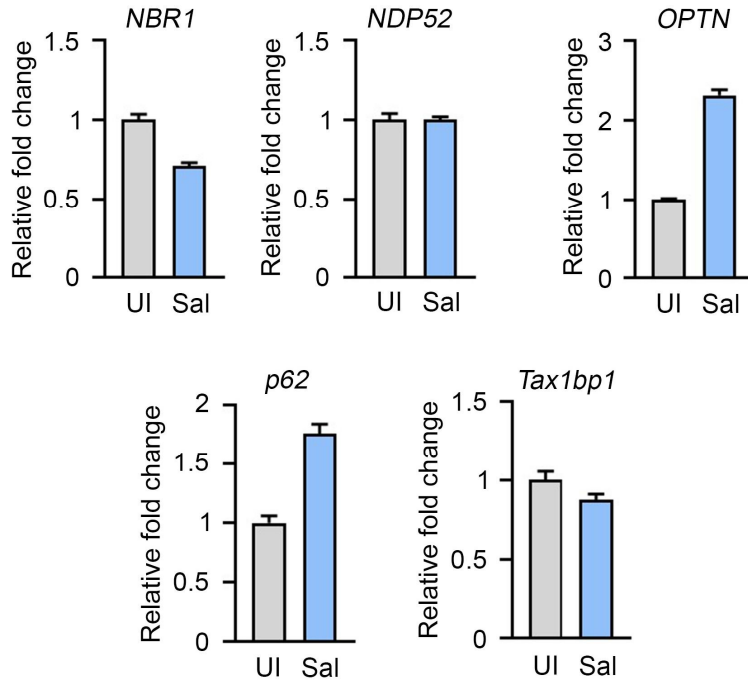


**Figure 13. Relative fold change in mRNA level of autophagy receptors in uninfected and *S. Typhimurium*-infected HeLa cells.**

HeLa cells were infected with *S. Typhimurium* MOI of 10 for 6 h and cell mRNA levels were analyzed by RT-qPCR. While mRNA levels of *NBR1*, *CALCOCO2*, and *TAX1BP1* decreased or showed no changes in *S. Typhimurium*-infected cells, those of *SQSTM1* and *Optineurin* increased compared to those of control cells.

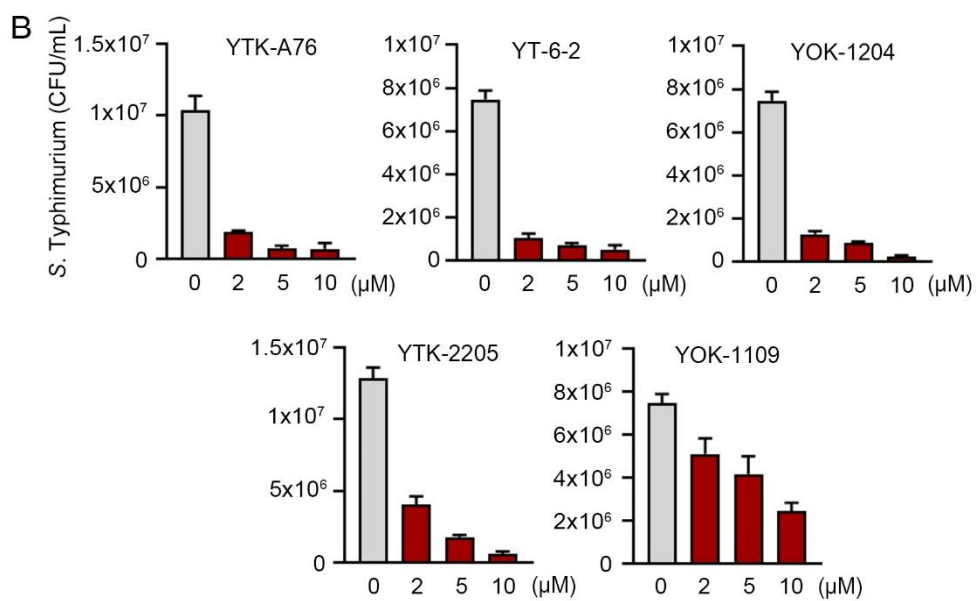
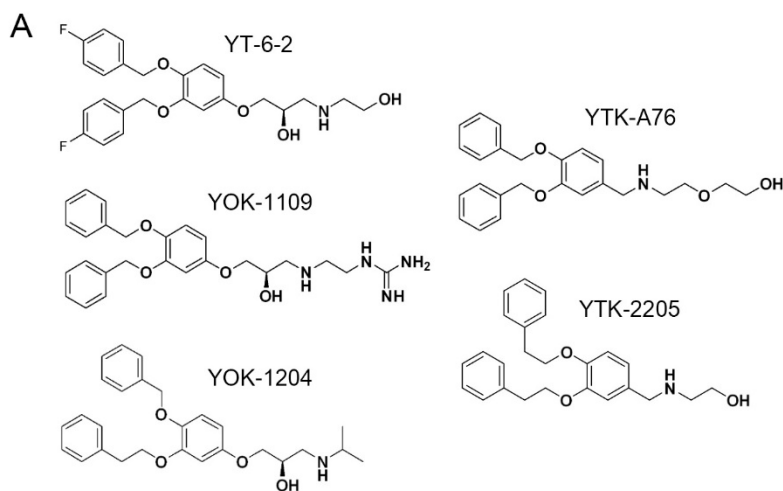




**Figure 14. Structure of five p62 ligands that show antimicrobial efficacy against intracellular *S. Typhimurium*.**

(A) Schematic diagram of five p62 ligands (YTK-A76, YT-6-2, YTK-2205, YOK-1109, and YOK-1204). (B) Quantitative graphs that show the number of intracellular *S. Typhimurium* in RAW264.7 cells. The cells were infected with *S. Typhimurium* MOI of 10 for 30 min followed by incubation of p62 ligands at indicated concentrations for 6 h. Cell lysates were diluted and subjected to colony-forming unit assay.

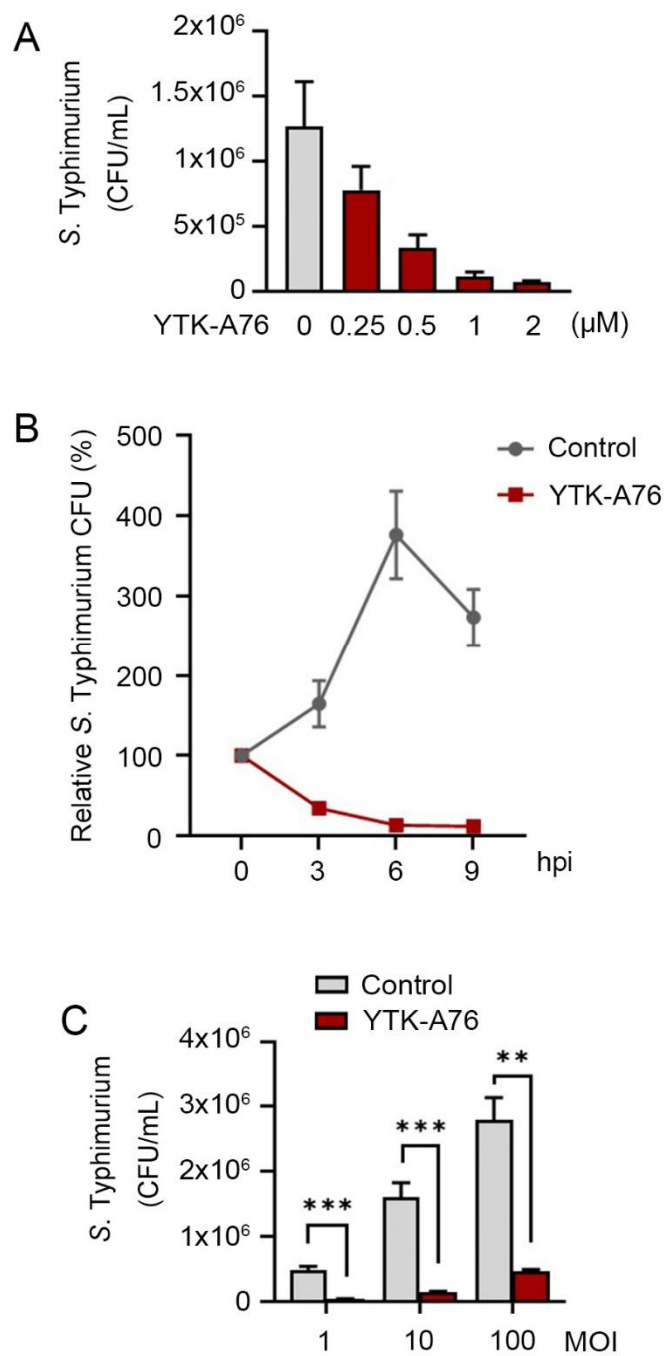


**Figure 15. Concentration, time, and MOI-dependent antimicrobial effect against intracellular *S. Typhimurium* by p62 ligand.**

(A) Graph of CFU indicating the number of intracellular *S. Typhimurium* in RAW264.7 cells treated with indicated concentrations of YTK-A76 for 6 h. (B) RAW264.7 cells were infected with *S. Typhimurium* MOI of 10 and the cells were incubated with or without YTK-A76 (5  $\mu$ M) for indicated time points. (C) RAW264.7 cells were infected with indicated MOI of *S. Typhimurium* for 30 min followed by 10  $\mu$ M YTK-A76 treatment for 6 h and measured intracellular *S. Typhimurium* by CFU assay.

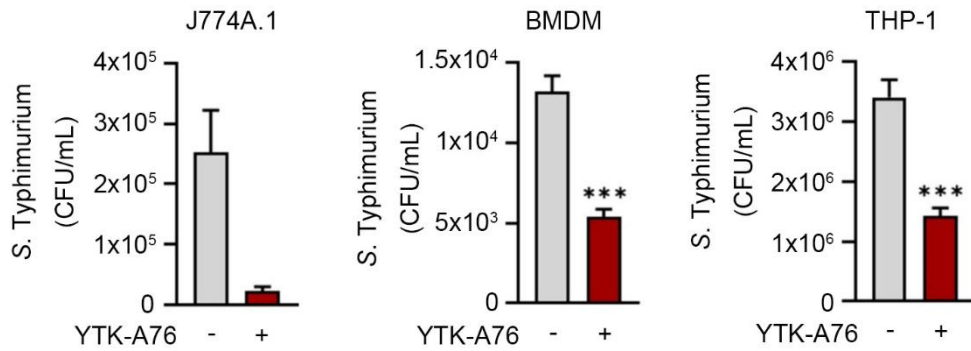


**Figure 16. Antimicrobial effect of p62 ligand against intracellular *S. Typhimurium* in various macrophage cell lines.**

Graphs of CFU indicating the number of intracellular *S. Typhimurium* in J774A.1, bone marrow-derived macrophages (BMDMs), and THP-1 cells treated with p62 agonists at 10  $\mu$ M for 6 h following 30 min of *S. Typhimurium* infection (MOI 10).

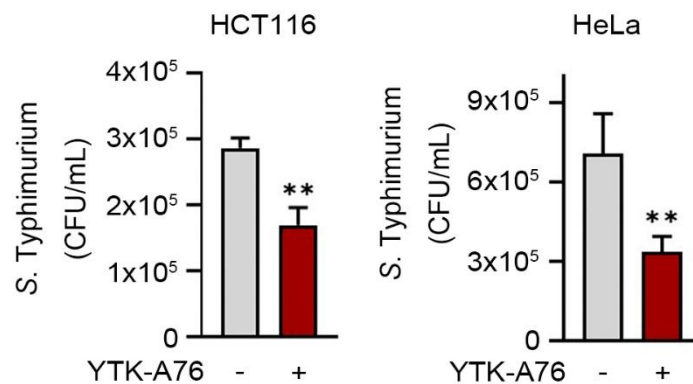


**Figure 17. Antimicrobial effect against intracellular *S. Typhimurium* by p62 ligand in various epithelial cell lines.**

A Graph of the colony-forming unit (CFU) indicates the number of intracellular *S. Typhimurium* in HCT116 and HeLa cells treated with 10  $\mu$ M YTK-A76 for 6 h.

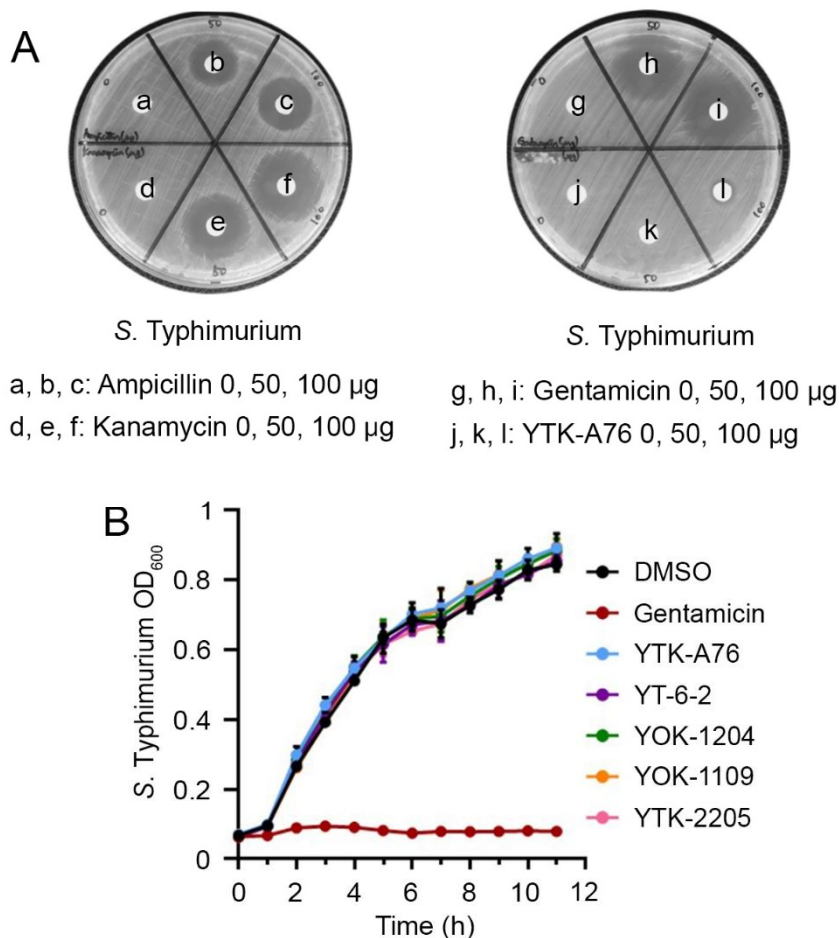


**Figure 18. p62 agonists do not directly inhibit the growth of *S. Typhimurium*.**

(A) Disc diffusion assay with *S. Typhimurium*. The bacteria spread LB plates were incubated with YTK-A76 and antibiotics including ampicillin, kanamycin, and gentamicin at indicated quantities. (B) *S. Typhimurium* was cultured in LB culture media with p62 agonists (15  $\mu$ M) or gentamicin (30  $\mu$ M) at 37°C. The OD<sub>600</sub> was measured every hour until 12 h.

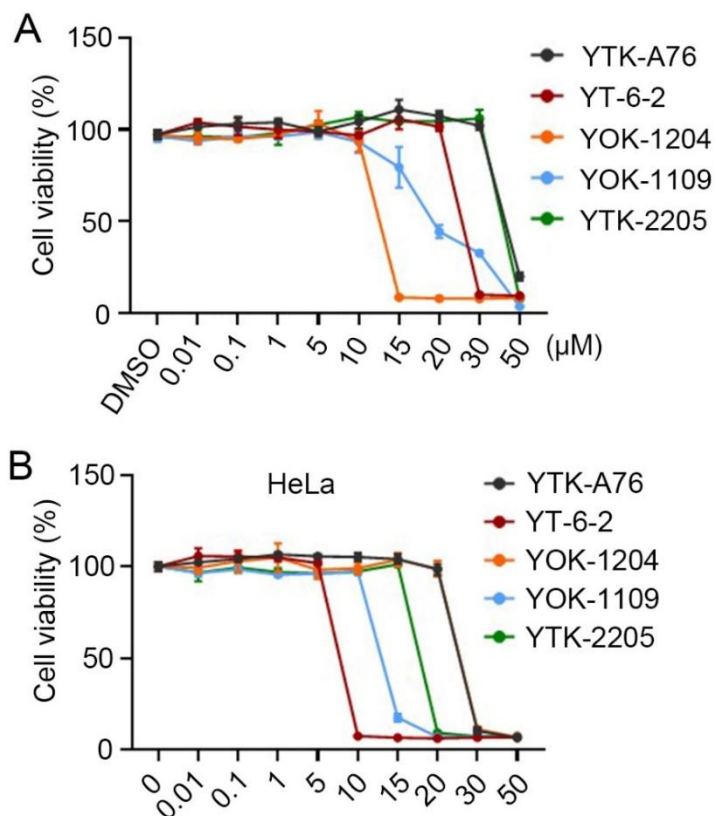


**Figure 19. Cell viability assay with p62 agonists.**

RAW264.7 (A) and HeLa (B) cells were incubated with p62 agonists at indicated concentrations for 72 h and cell viability was measured by WST assay.

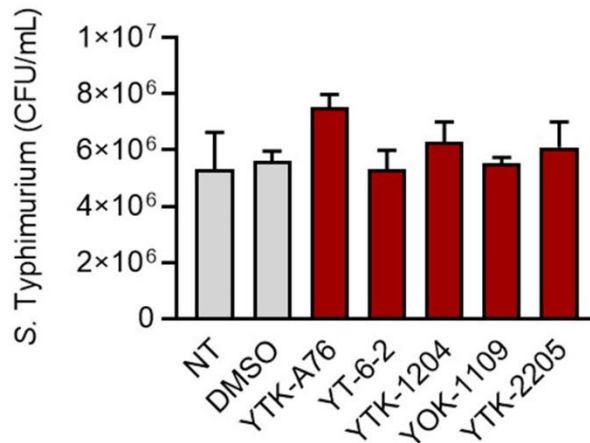
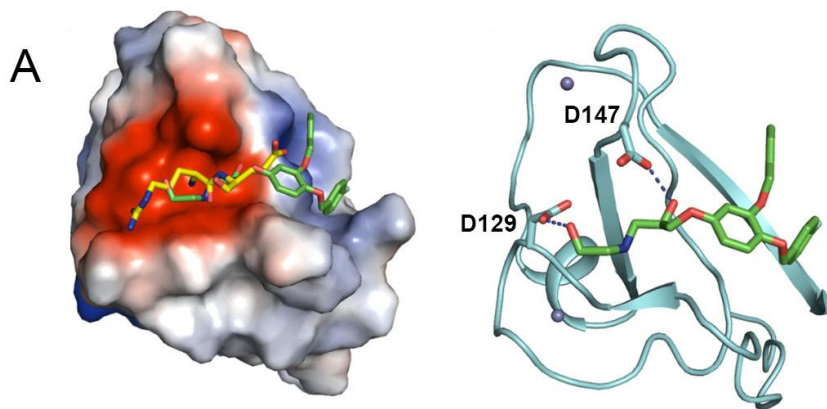


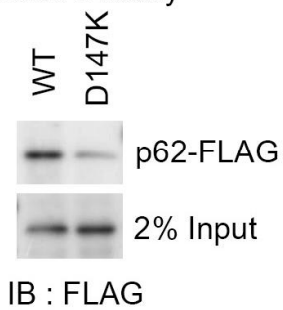
**Figure 20. p62 agonists do not affect bacterial entry.**

RAW264.7 cells were pre-treated with p62 agonists for 3 h followed by *S. Typhimurium* infection (MOI 10) for 1 h. Cell lysates were serially diluted and subjected to CFU assay. There are no changes in the number of intracellular bacteria between p62 agonist treated or untreated cells.





**B** YT-6-2-Biotin  
pulldown assay



**C**

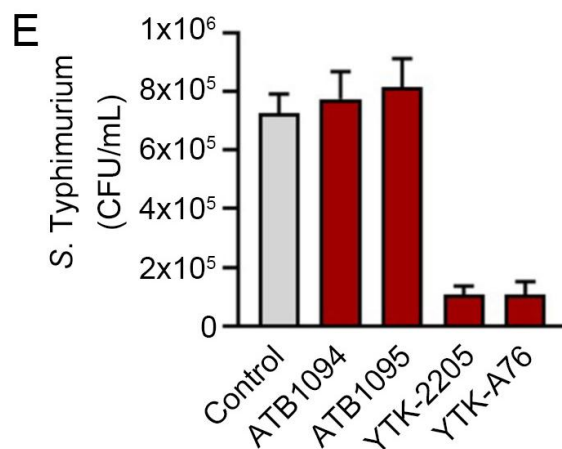
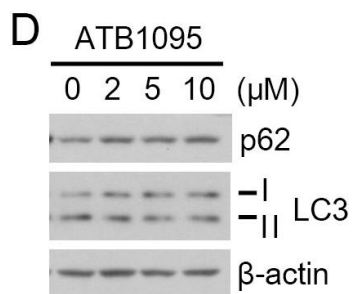
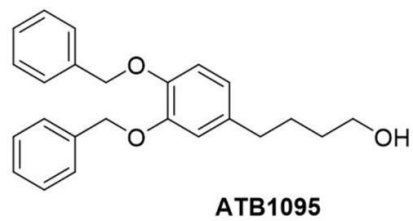


**Figure 21. Schematic diagram of p62 ZZ domain and pull-down assay.**

(A) Surface electrostatic potential of p62 ZZ domain in complex with Arg-Glu peptide (PDB ID: 6MIU). Docked YT-6-2 compound (green) was superimposed with Arg-Glu peptide (yellow) as substrate (left panel). The predicted binding mode of YT-6-2 showing the binding site of YT-6-2 to p62 ZZ domain was expected to overlap the substrate-binding site of p62 (right panel). (B) Pulldown assay using biotinylated YT-6-2 and p62 wild type or p62 ZZ point mutant (D147K) plasmids expressed in *p62*<sup>-/-</sup> HeLa cells. 500  $\mu$ g of total protein was used in the pulldown assay, and p62 was detected by immunoblotting analysis using an anti-Flag antibody. (C) A structure of negative control compound that lacks the essential amine group required for hydrogen bond with the side chain of Asp147. (D) HeLa cells were treated with ATB1095 at indicated concentrations for 6 h. (E) *S. Typhimurium*-infected RAW264.7 cells were treated with negative control compound (ATB10094 and ATB10095) or positive compound (YTK-2205 and YTK-A76) at 10  $\mu$ M for 6 h.

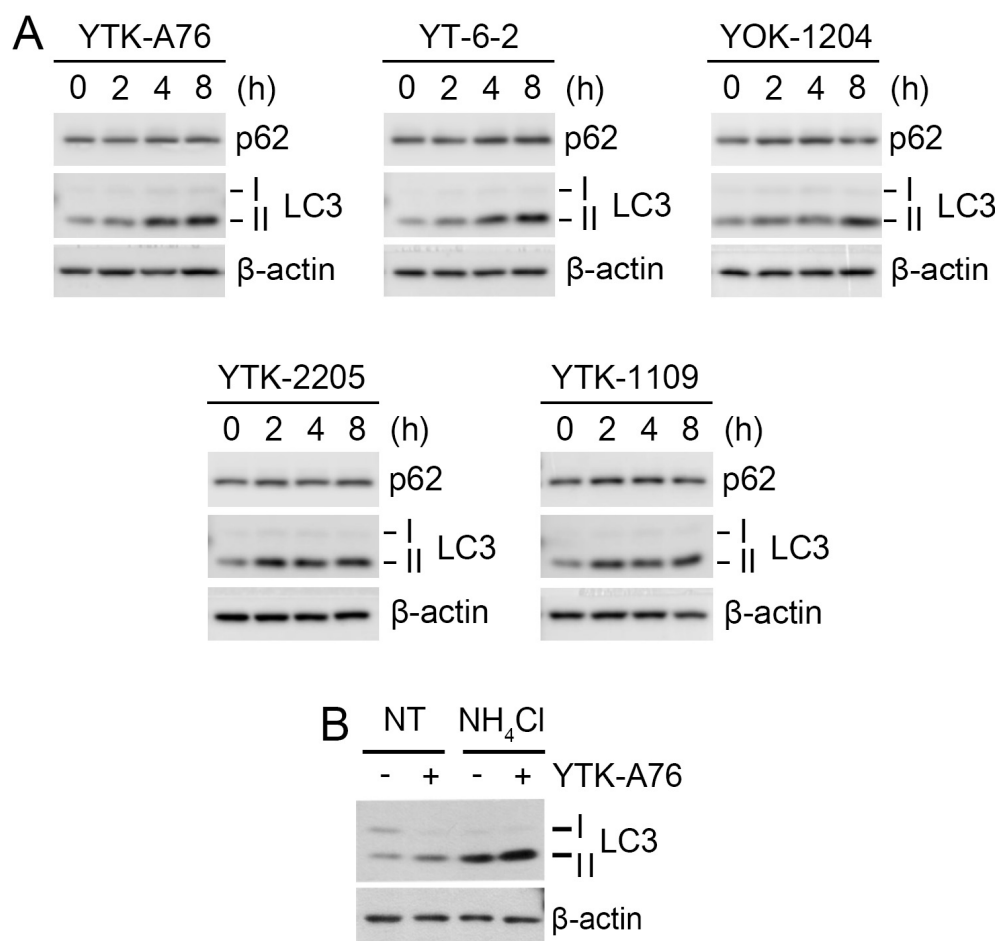


**Figure 22. p62 agonists accelerate autophagosome biogenesis and autophagic flux.**

(A) HeLa cells were treated with p62 agonists (YTK-A76, YT-6-2, YOK-1204, YTK-2205, and YTK-1109) for indicated time points at 5  $\mu$ M. Lipidation of LC3B was analyzed by immunoblotting assay. (B) HeLa cells were treated with 5  $\mu$ M YTK-A76 alone or with 20 mM  $\text{NH}_4\text{Cl}$  for 6 h for autophagy flux analysis.

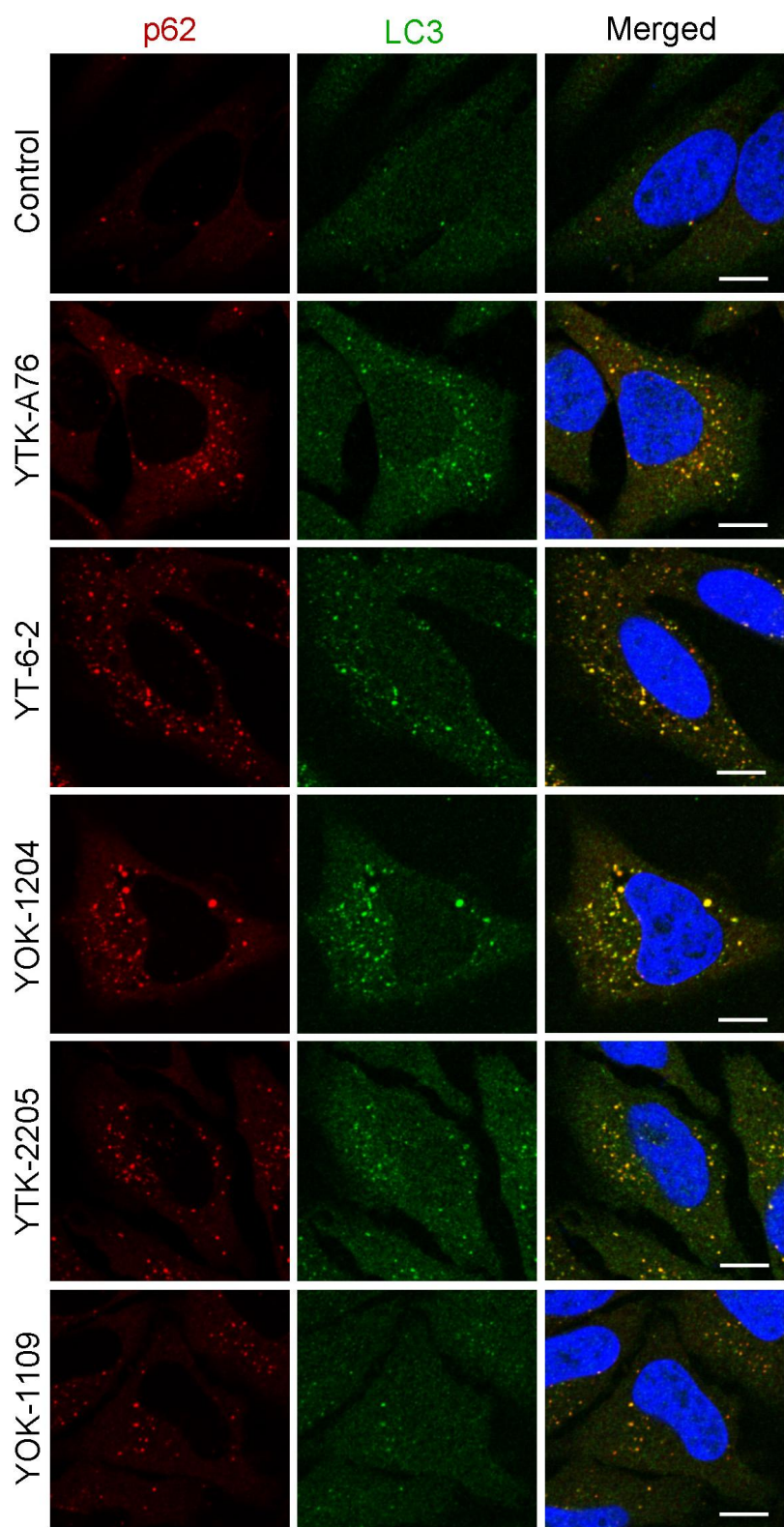


**Figure 23. p62 agonists induce p62 oligomerization that induces autophagosome biogenesis.**

HeLa cells were treated with p62 agonists (YTK-11A76, YT-6-2, YOK-1204, YTK-2205, and YOK-1109) for 6 h at 5  $\mu$ M. Following cell fixation, cells were immunostained with anti-p62 and anti-LC3B. Scale bar: 10  $\mu$ m.

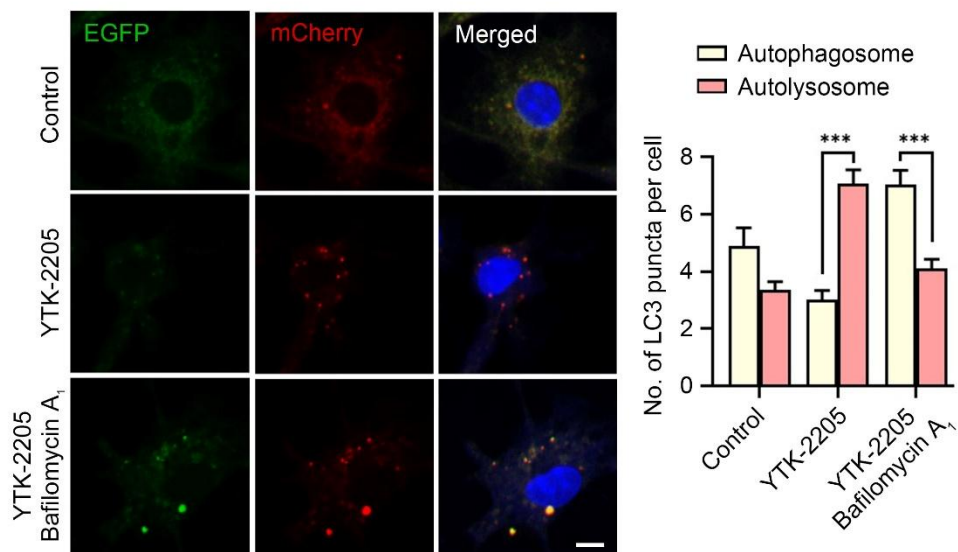


**Figure 24. p62 agonist YTK2205 induces autophagolysosome formation.**

BMDMs were transduced with retrovirus expressing mCherry-EGFP-LC3B plasmid. Cells were analyzed by fluorescent confocal microscopy for measuring autophagic flux upon YTK-2205 (5 μM) treatment in the absence or presence of bafilomycin A1 (200 nM; 2 h). Scale bar, 5 μm (left panel). The number of LC3 dots per cell was quantified (right panel).

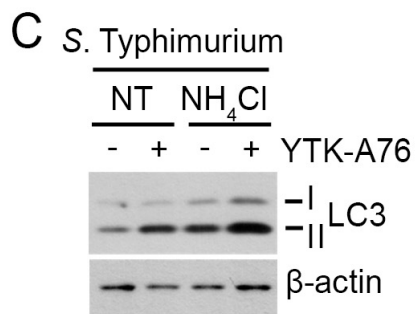
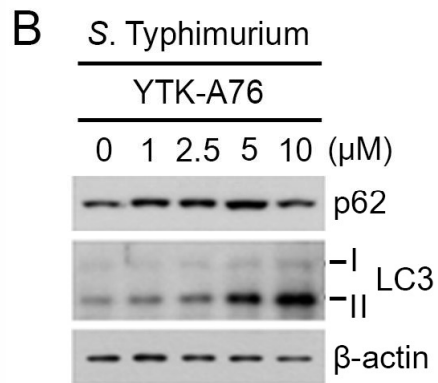
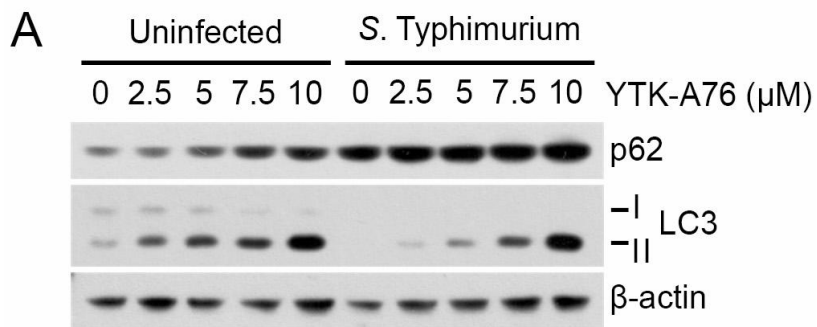




**Figure 25. p62 agonist rescue autophagic activities from suppression by *S. Typhimurium*.**

(A) HeLa cells were infected with *S. Typhimurium* at MOI 10 and p62 ligand was treated at indicated concentrations for 6 h and LC3B lipidation was analyzed by immunoblotting. (B) BMDMs were infected with *S. Typhimurium* MOI of 10 and YTK-A76 were treated dose-dependently at indicated concentrations for 6 h. (C) *S. Typhimurium* infected HeLa cells were treated with 10  $\mu$ M YTK-A76 alone or with 20 mM  $\text{NH}_4\text{Cl}$  for 6 h and cell lysates were subjected to immunoblotting to analyze autophagic flux.

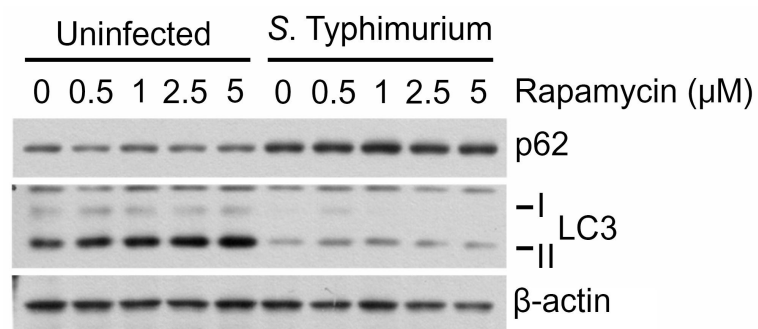


**Figure 26. Canonical autophagy activator rapamycin cannot rescue autophagic activities from suppression by *S. Typhimurium*.**

Uninfected and *S. Typhimurium* (MOI 10) infected HeLa cells were treated with rapamycin at indicated concentrations for 6 h. Cell lysates were subjected to immunoblotting.

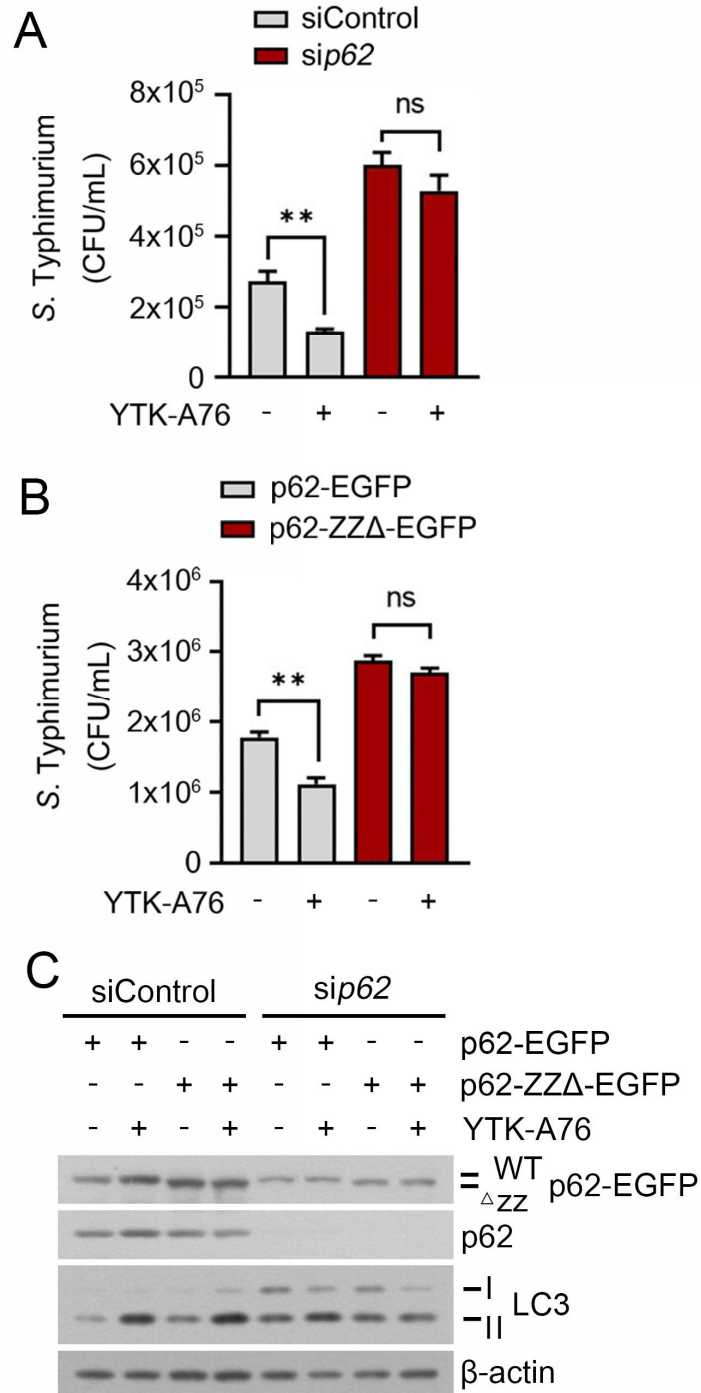


**Figure 27. The antimicrobial effect of p62 agonist is p62 ZZ domain dependent.**

(A) HeLa cells were transfected with control or p62 siRNA for 48 h followed by 5 h of *S. Typhimurium* (MOI 10) infection. Cell lysates were diluted and subjected to colony-forming unit assay. The number of intracellular *S. Typhimurium* increased in p62 knockdown cells compared to those in control cells. When siControl cells were treated with p62 agonist, the number of intracellular *S. Typhimurium* was reduced, whereas there was no difference in the number of those in si*SQSTM1* cells. (B) HeLa cells were knockdown by 3'UTR si*SQSTM1* for 24 h followed by 24 h transfection of p62-EGFP or p62-ZZΔ-EGFP. After the transfection of p62 plasmids, cells were infected with *S. Typhimurium* MOI of 10 for 5 h. When p62-EGFP overexpressed cells were treated with p62 agonist, the number of intracellular *S. Typhimurium* was reduced, whereas there was no difference in the number of those in p62-ZZΔ-EGFP overexpressed cells. (C) The same experiments were performed as in figure B and the cell lysates were subjected to immunoblotting analysis.

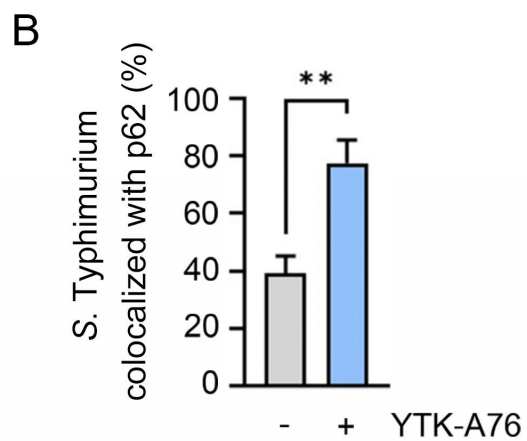
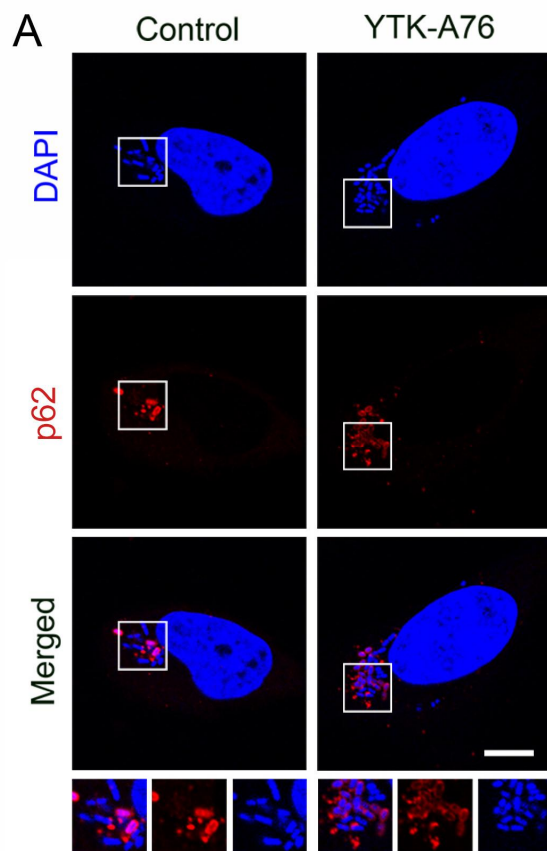


**Figure 28. The p62 agonist facilitates the association of p62 with intracellular *S. Typhimurium*.**

(A) Co-localization analysis of p62 (Red) and *S. Typhimurium* (cytosolic DAPI) by using immunostaining. HeLa cells were infected with *S. Typhimurium* and treated with or without 10  $\mu$ M YTK-A76 for 6 h. (B) Quantitative graph represents the average percentage of *S. Typhimurium* co-localize with p62 puncta per HeLa cells (n = 12).

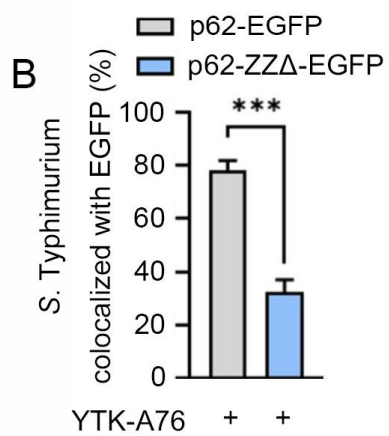
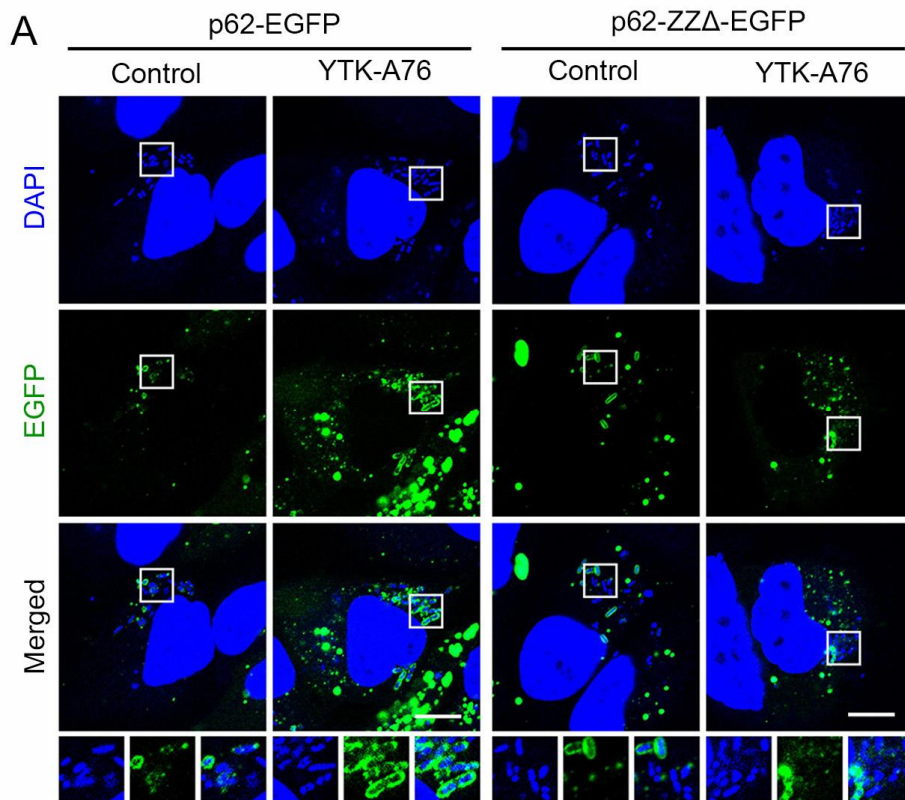


**Figure 29. p62 agonist YTK-A76 facilitates the association of p62 with intracellular *S. Typhimurium* via the ZZ domain of p62.**

(A) HeLa cells were knockdown by 3'UTR si*SQSTM1* for 24 h and then p62-EGFP or p62-ZZΔ-EGFP was rescued for 24 h. The cells were infected with *S. Typhimurium* and incubated with or without YTK-A76 10 μM for 5 h. (B) A Quantitative graph that shows the percentage of intracellular bacteria (DAPI) co-localize with EGFP puncta per HeLa cells (n = 15).



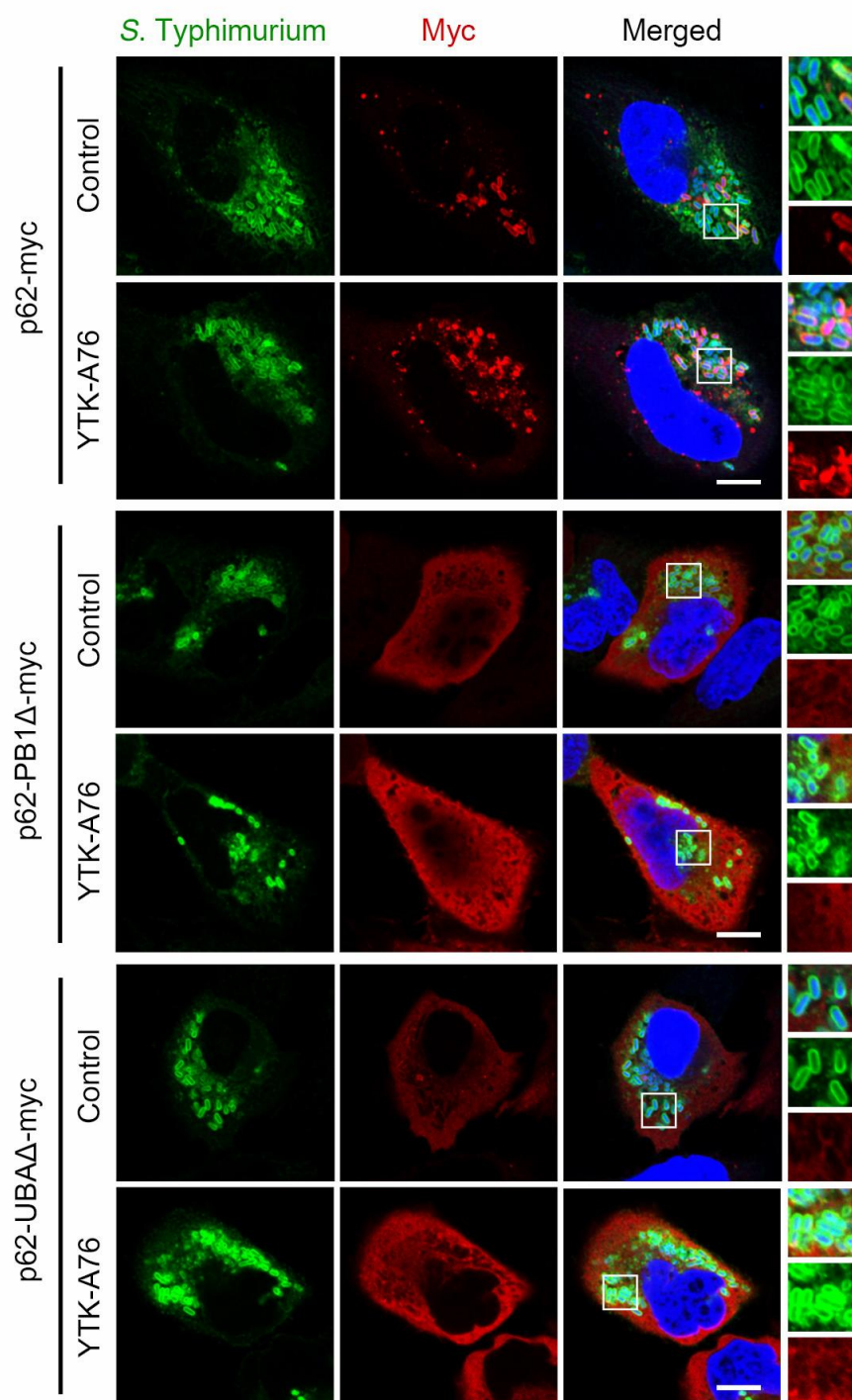


**Figure 30. p62 agonist-induced p62 association with intracellular *S. Typhimurium* requires PB1 and UBA domain.**

HeLa cells were knockdown by 3'UTR si*SQSTM* for 24 h and then p62-myc, p62-PB1Δ-myc, or p62-UBAΔ-myc was rescued for 24 h. The cells were infected with *S. Typhimurium* and incubated with or without YTK-A76 10 μM for 5 h. Transiently overexpressed cells were immunostained with anti-Salmonella (green) and anti-myc (red). Scale bars: 10 μm. When p62-myc overexpressing cells were treated with p62 agonist, the number of p62-associated intracellular *S. Typhimurium* increased, but there was no difference in the number in p62-PB1Δ-myc or p62-UBAΔ-myc expressing cells.

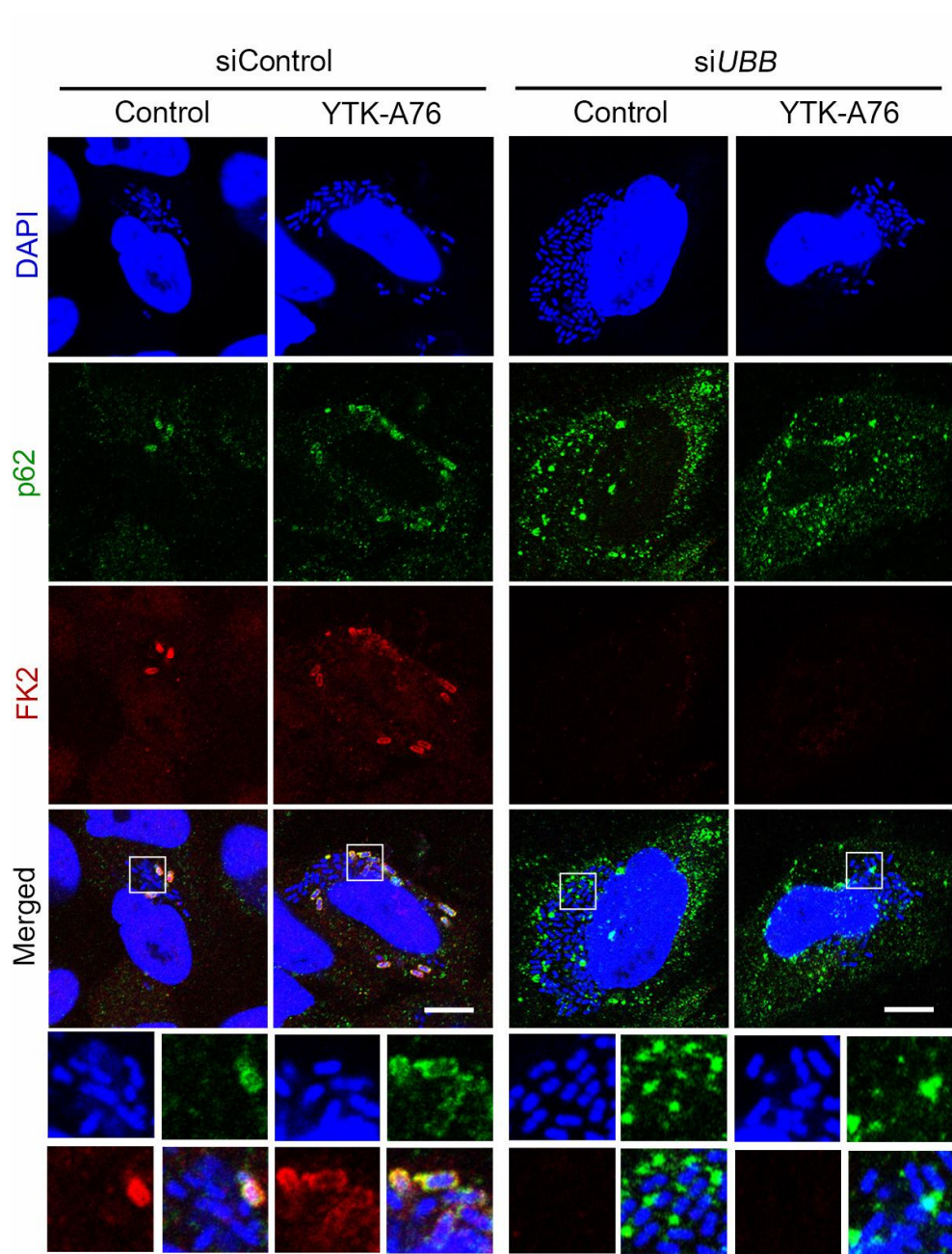


**Figure 31. Association of p62 with intracellular *S. Typhimurium* requires ubiquitination of the pathogen.**

HeLa cells were transfected with siControl or si*UBB* followed by *S. Typhimurium* infection (MOI 10). After 30 min of *S. Typhimurium* infection, cells were treated with or without YTK-A76 at 10  $\mu$ M for 5 h. After fixation, the cells were immunostained with anti-FK2 (red) and anti-p62 (green), and *S. Typhimurium* is stained with DAPI (blue).

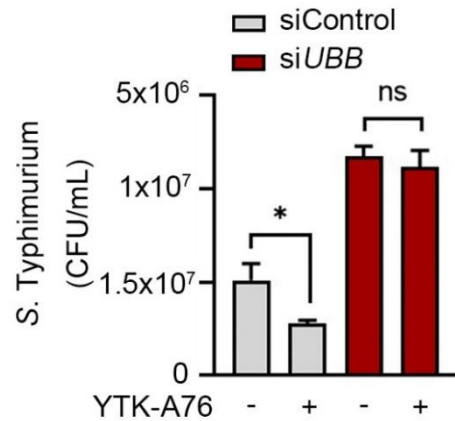


**Figure 32. The antimicrobial effect of p62 agonist YTK-A76 requires ubiquitination of intracellular *S. Typhimurium*.**

HeLa cells were transfected with control or *UBB* siRNA for 48 h, followed by *S. Typhimurium* infection for 5 h. The cells were incubated with or without YTK-A76 for 5 h at 2 hpi.

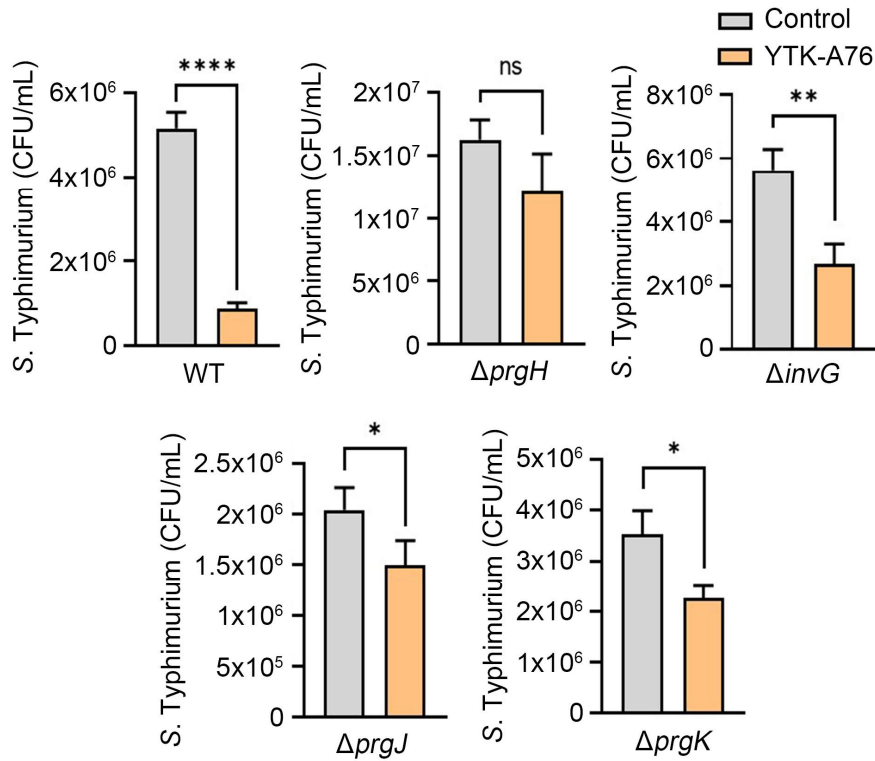


**Figure 33. The antimicrobial effect of p62 agonist against *S. Typhimurium* strains with mutations in SPI-1.**

Quantitative graphs that show the number of intracellular WT and mutant *S. Typhimurium* in RAW264.7 cells. The cells were infected with *S. Typhimurium* WT or mutant strains MOI of 10 for 30 min followed by incubation with or without YTK-A76 at 2  $\mu$ M for 6 h. Cell lysates were diluted and subjected to colony-forming unit assay.

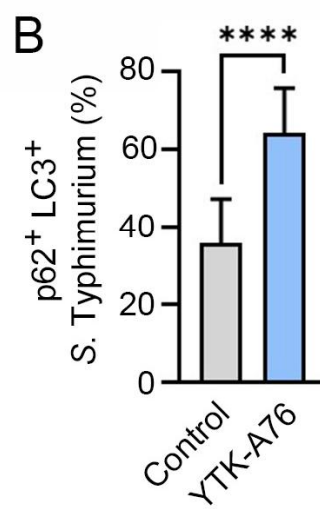
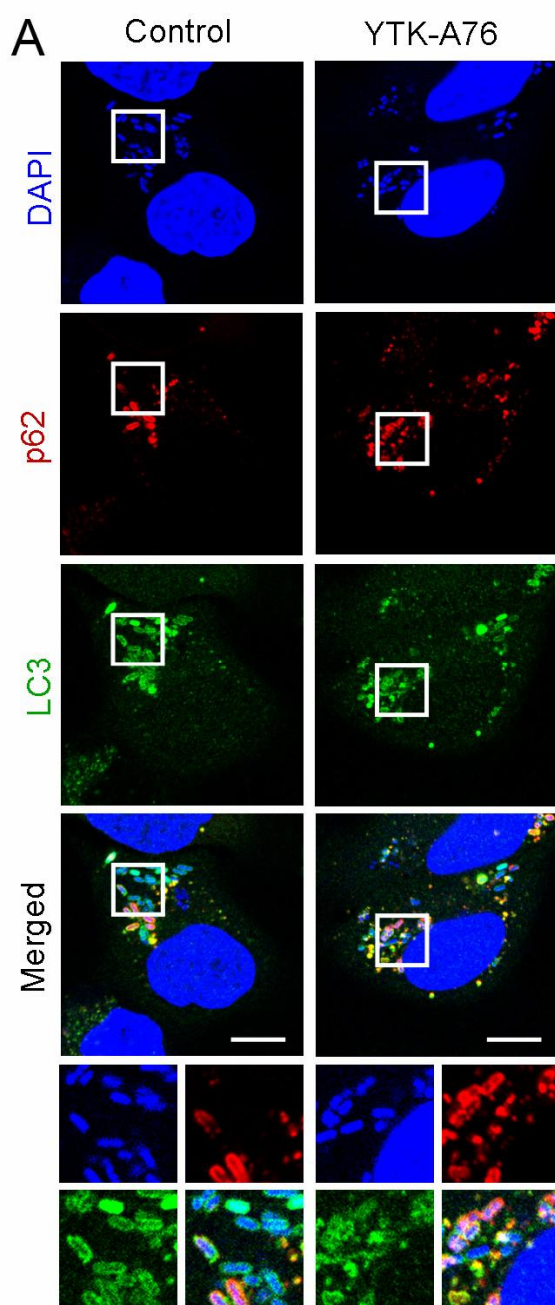


**Figure 34. p62 agonist increases the association of LC3B with intracellular *S. Typhimurium*.**

(A) Co-localization analysis of LC3 (Green) and *S. Typhimurium* (cytosolic DAPI) by immunofluorescence analyses. Representative images (left panel) of *S. Typhimurium*-infected HeLa cells treated with 10  $\mu$ M YTK-A76 for 6 h. (B) Quantitative graph represents the average percentage of *S. Typhimurium* colocalized with LC3 puncta per cells ( $n = 15$ ). Scale bar: 10  $\mu$ m.



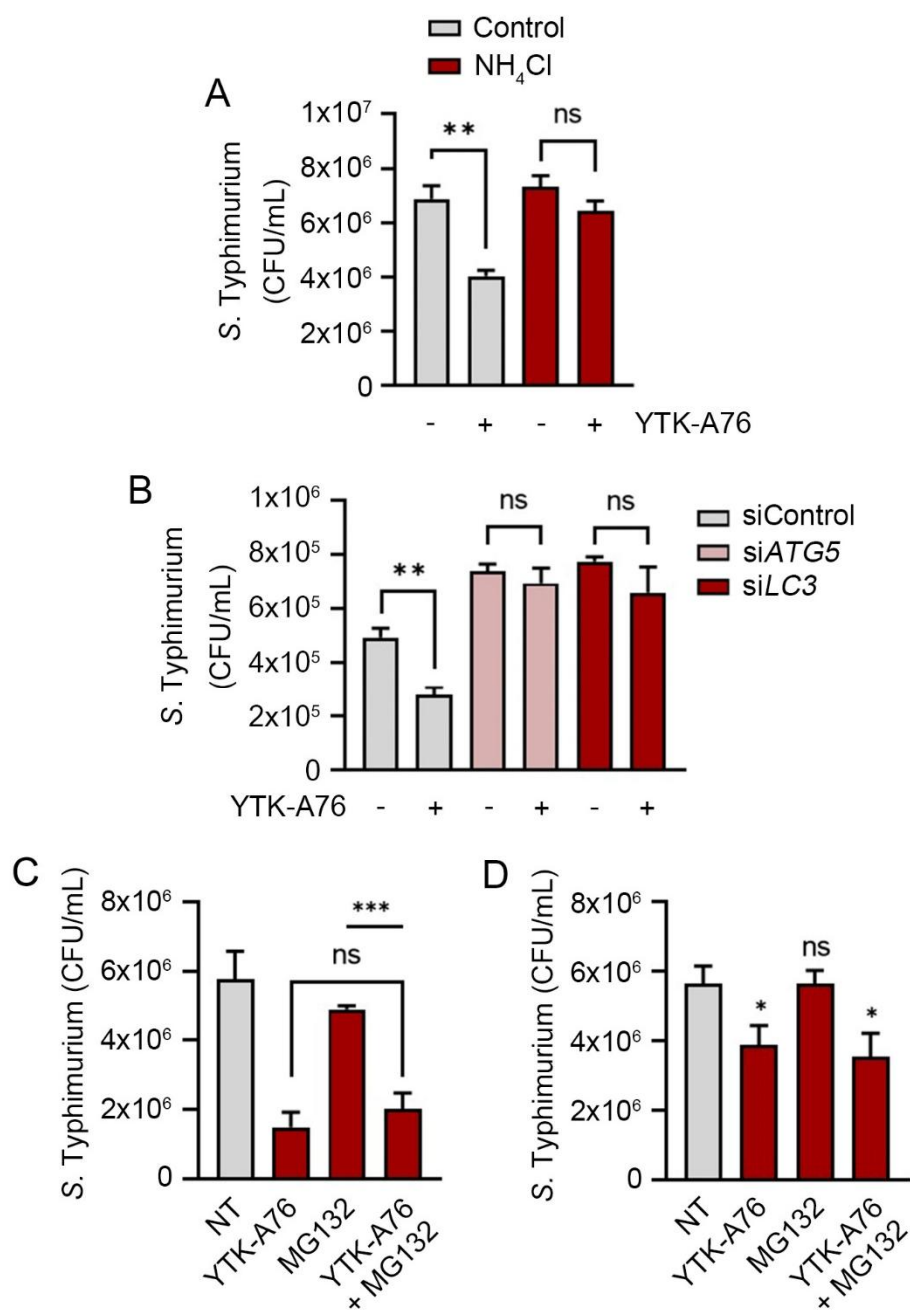


**Figure 35. The antimicrobial effect of the p62 agonist YTK-A76 requires autophagic activity.**

(A) A graph of CFU indicating intracellular *S. Typhimurium* in HeLa cells treated with p62 ligand for validation of autophagic degradation of *S. Typhimurium*. HeLa cells were transfected with control, ATG5, or LC3B targeting siRNA for 48 h followed by 30 min infection of *S. Typhimurium* (MOI 10). The cells were treated with or without YTK-A76 10  $\mu$ M for 5 h. The number of intracellular *S. Typhimurium* increased in *ATG5* or *LC3* knockdown cells compared to those in control cells. When siControl cells were treated with p62 agonist, the number of intracellular *S. Typhimurium* was reduced, whereas there was no difference in the number of those in si*ATG5* or si*LC3* cells. (B) A graph of CFU indicating intracellular *S. Typhimurium* in HeLa cells treated with p62 agonists in the presence or absence of NH<sub>4</sub>Cl. HeLa cells were infected with *S. Typhimurium* for 30 min. After washing out with DPBS, cells were treated with 10  $\mu$ M YTK-A76 and 20 mM NH<sub>4</sub>Cl for 4 h. When cells are incubated with p62 agonist, the number of intracellular *S. Typhimurium* decreased, whereas there was no difference in the number of those in NH<sub>4</sub>Cl treated cells. (C) RAW264.7 cells were infected with *S. Typhimurium* (MOI of 10) for 30 min followed by incubation with YTK-A76 (2  $\mu$ M) or MG132 (5  $\mu$ M) for 6 h. The number of intracellular bacteria was measured by a CFU assay. (D) *S. Typhimurium*-infected HeLa cells were incubated with YTK-A76 (10  $\mu$ M) or MG132 (5  $\mu$ M) for 6 h and the number of intracellular bacteria was measured by CFU assay.

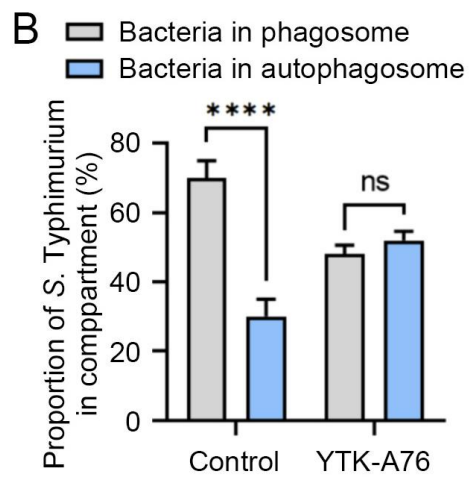
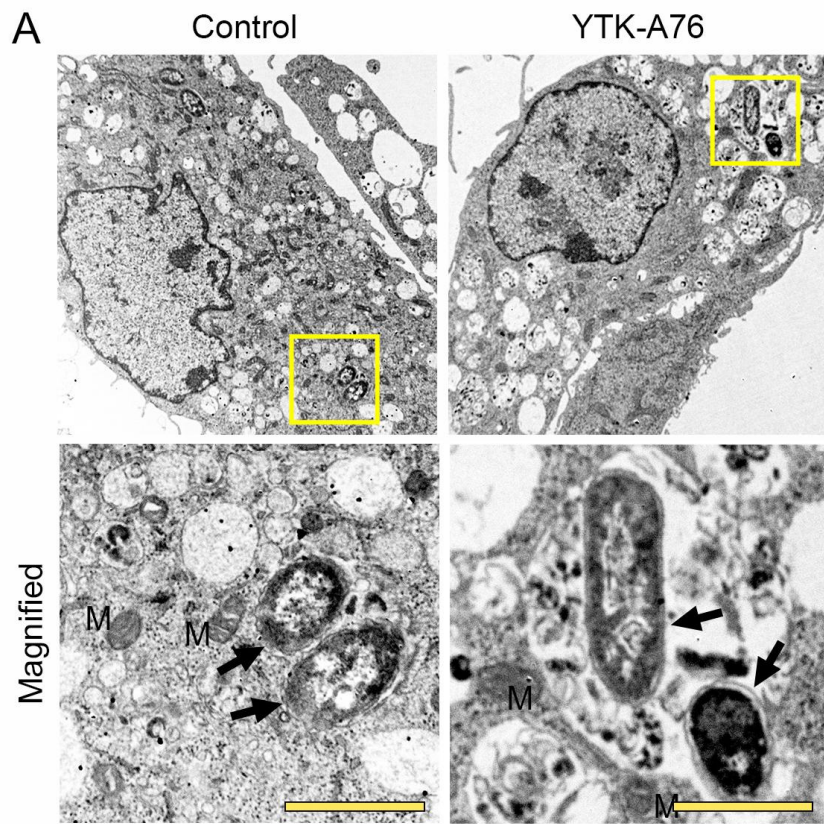


**Figure 36. The p62 agonist accelerate targeting of *S. Typhimurium* to autophagosomes.**

(A) Representative TEM (transmission electron microscopy) images of RAW264.7 cells treated with or without p62 ligand in the presence of intracellular *S. Typhimurium* (yellow boxes were magnified). Scale bar: 1  $\mu\text{m}$ . (B) Quantitative graph that shows a number of bacteria in phagosome and autophagosome in absence and presence of the p62 agonist in RAW264.7 cells.

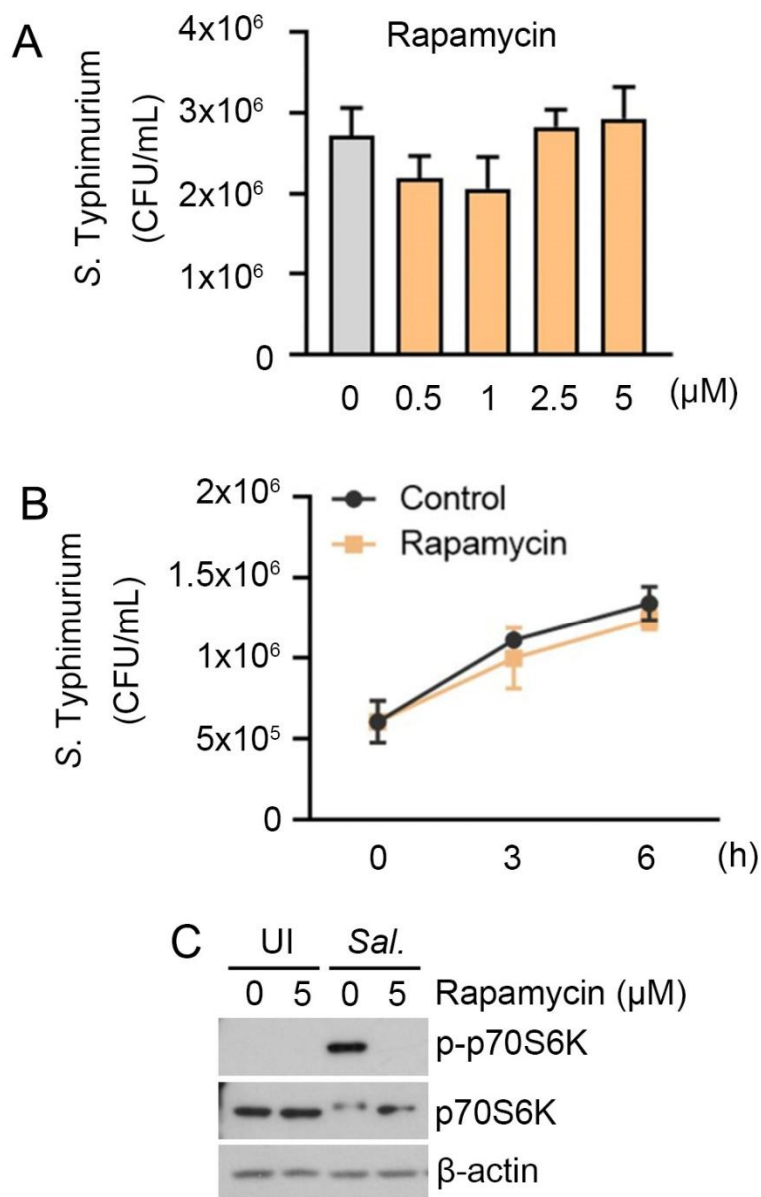


**Figure 37. Canonical autophagy inducer rapamycin has no antimicrobial effect against intracellular *S. Typhimurium*.**

(A) RAW264.7 cells were infected with *S. Typhimurium* (MOI 10) for 30 min and rapamycin was treated at indicated concentrations for 6 h. There were no differences in the number of *S. Typhimurium* between cells treated with or without rapamycin.

(B) *S. Typhimurium*- (MOI 10) infected RAW264.7 cells treated with rapamycin at 5  $\mu$ M for indicated time points and the number of intracellular bacteria was measured by CFU analyses. (C) Inhibition of mTOR activity by rapamycin in RAW264.7 cells.

Phosphorylation of P70S6K is dramatically inhibited in presence of 5  $\mu$ M of rapamycin for 6 h.

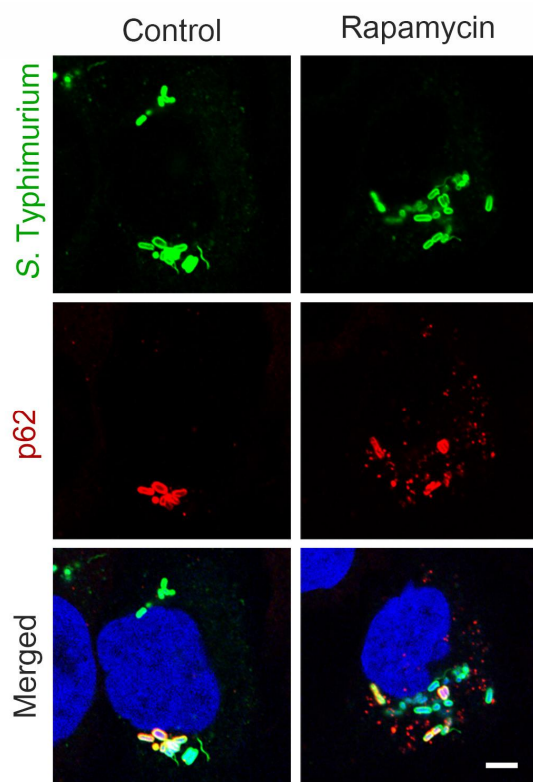


**Figure 38. Rapamycin does not induce targeting of *S. Typhimurium* to autophagosomes.**

Co-localization analysis of *S. Typhimurium* (green) and p62 (red) in HeLa cells with the presence or absence of 10  $\mu$ M rapamycin for 6 h. Scale bar: 5  $\mu$ m.

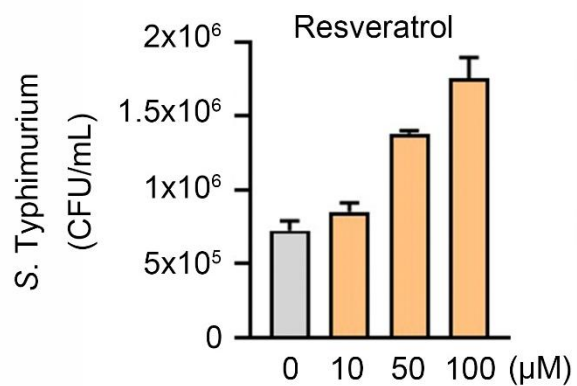


**Figure 39. Resveratrol does not inhibit the growth of intracellular bacteria.**

*S. Typhimurium*-infected RAW264.7 cells were treated with resveratrol at indicated concentrations for 6 h and the number of intracellular bacteria was measured by CFU assay.



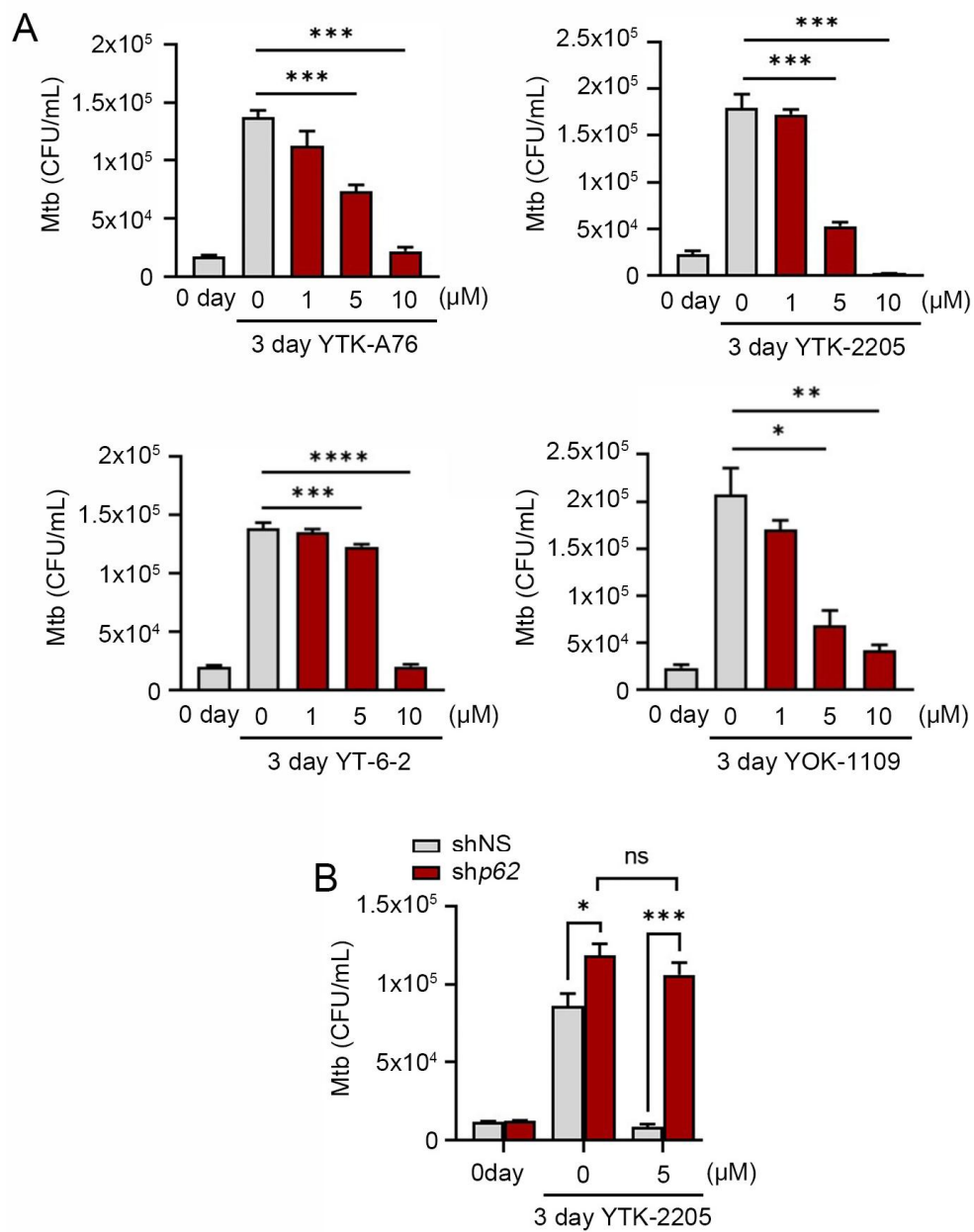


**Figure 40. Antimicrobial effect of p62 agonists against intracellular *Mycobacterium tuberculosis*.**

(A) Intracellular survival of Mtb assessed in BMDMs treated with YTK-A76 (1, 5, or 10  $\mu$ M) and YTK-2205 (1, 5, or 10  $\mu$ M) for 3 days. (B) BMDMs were transduced with lentivirus expressing shNS or shp62, and then treated with YTK-2205 (5  $\mu$ M) for 3 days. Intracellular survival of Mtb measured by CFU assay.

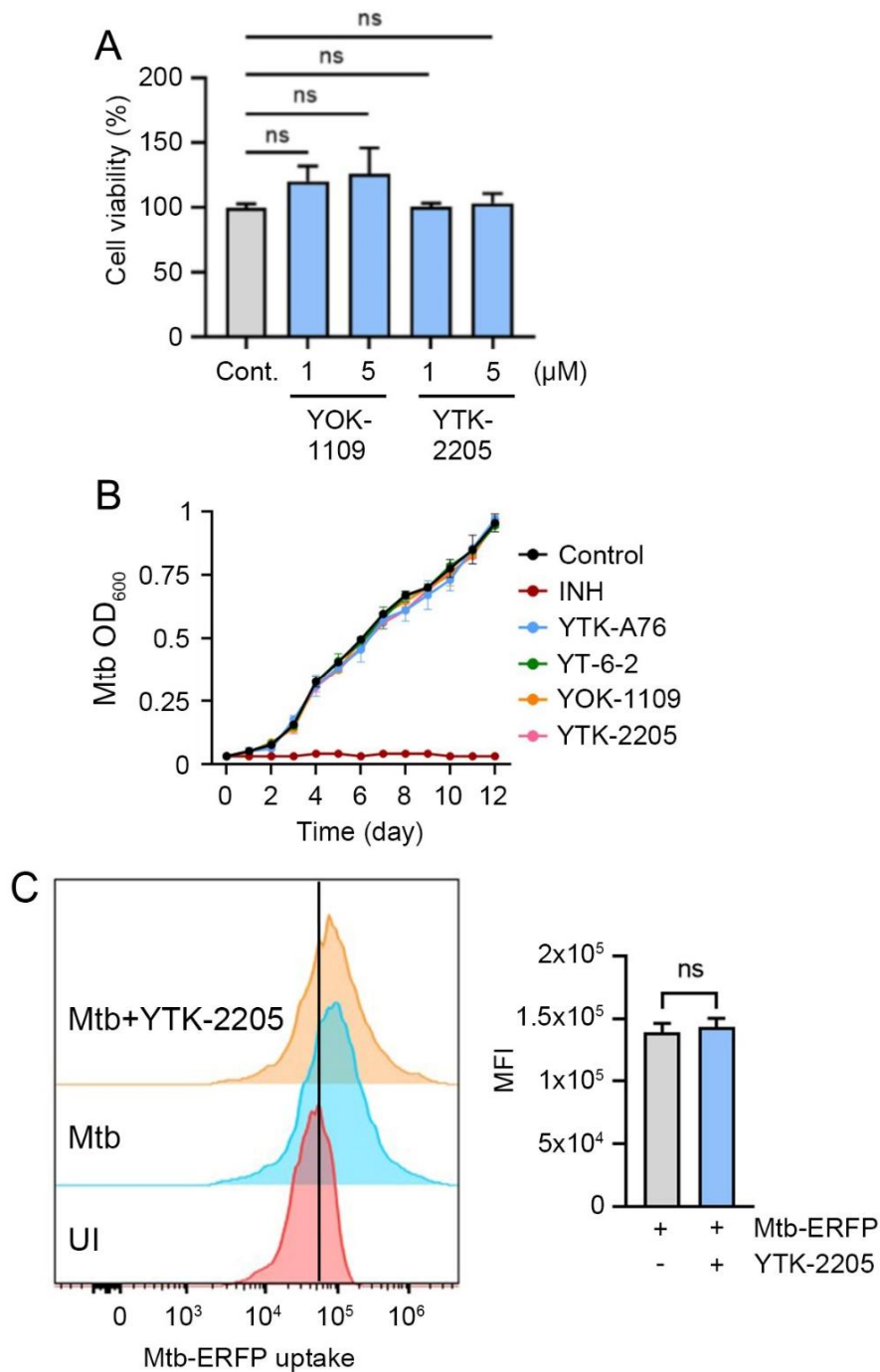


**Figure 41. p62 agonists do not show host or bacterial cell toxicity and do not affect bacterial entry.**

(A) BMDMs were treated with YOK-1109 or YTK-2205 at indicated concentrations for 72 h. Cell viability was measured by MTT assay. (B) The growth curve of Mtb in media containing 10  $\mu$ M of p62 agonists. OD<sub>600</sub> was measured daily for Mtb growth curve. (C) BMDMs were infected with Mtb-ERFP for 2 h in the absence or presence of YTK-2205 (10  $\mu$ M). Phagocytosis was measured by FACS analysis and analyzed the mean fluorescence intensity (MFI) by subtracting the value of the uninfected condition.

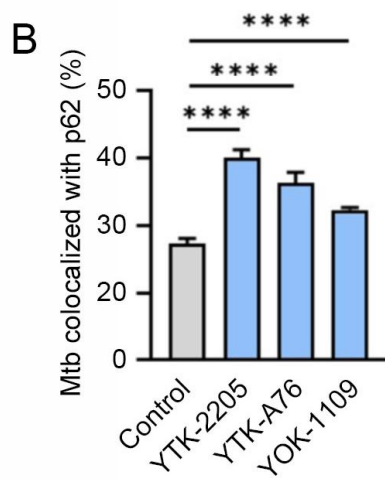
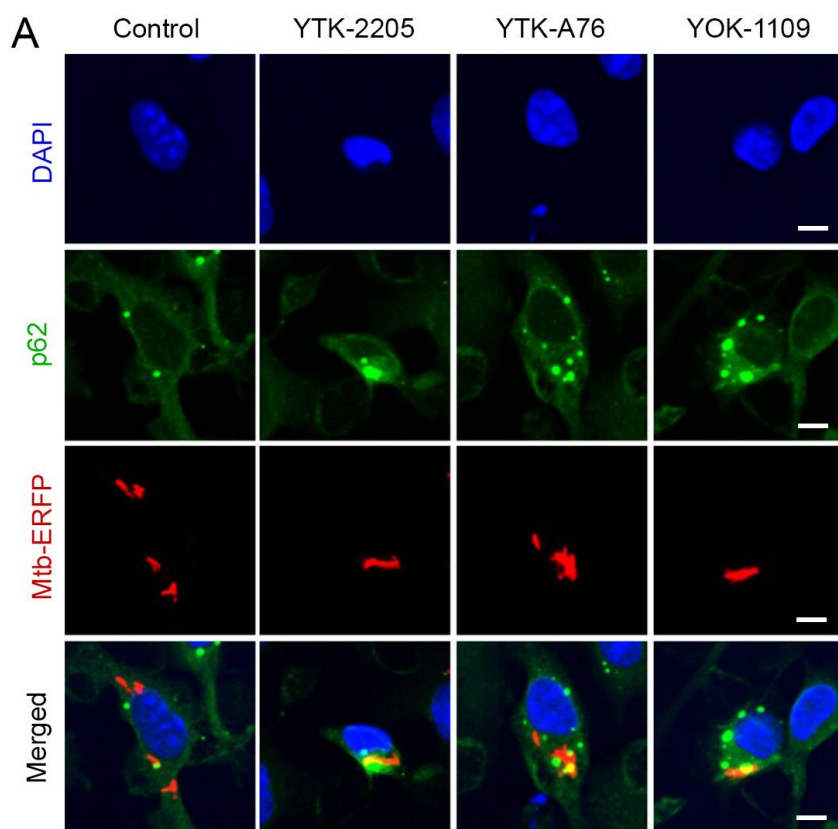


**Figure 42. p62 agonists facilitate the association of p62 with intracellular Mtb-ERFP.**

(A) BMDMs were infected with Mtb-ERFP (MOI of 5) for 2 h and then cells were treated with YTK-2205, YTK-A76, or YOK-1109 at 5  $\mu$ M for 18 h. Co-localization analysis of p62 (green) and Mtb-ERFP by immunofluorescence analysis. Scale bar, 5  $\mu$ m. (B) Quantitative data of the number of Mtb-ERFP (MOI of 5) co-localized with p62 (green) in BMDMs incubated with or without p62 agonists.

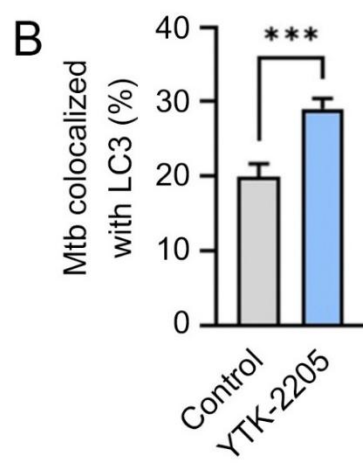
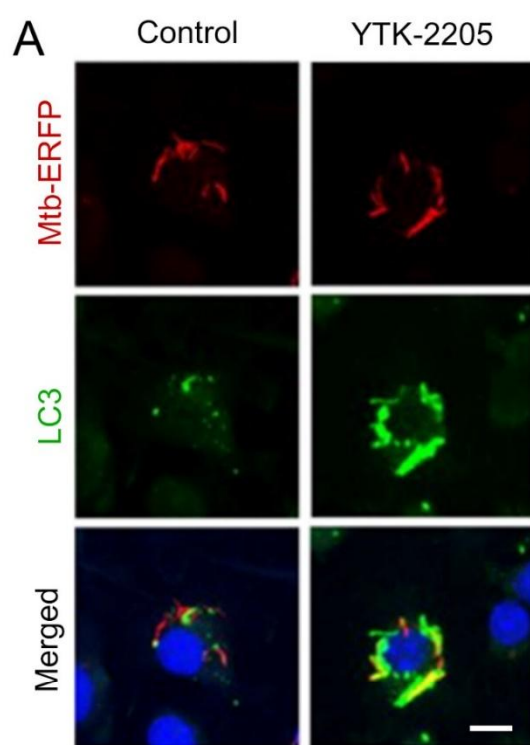


**Figure 43. p62 agonist YTK-2205 accelerates the targeting of intracellular *M. tuberculosis* to autophagosomes.**

(A) BMDMs were infected with Mtb-ERFP (MOI of 5) and treated with YTK-2205 (5  $\mu$ M). Co-localization analysis of LC3 (green) and Mtb-ERFP in BMDMs by using immunostaining analyses. Scale bar, 8  $\mu$ m. (B) A quantitative graph represents the average percentage of Mtb-ERFP colocalized with LC3 puncta per cell (n = 11).



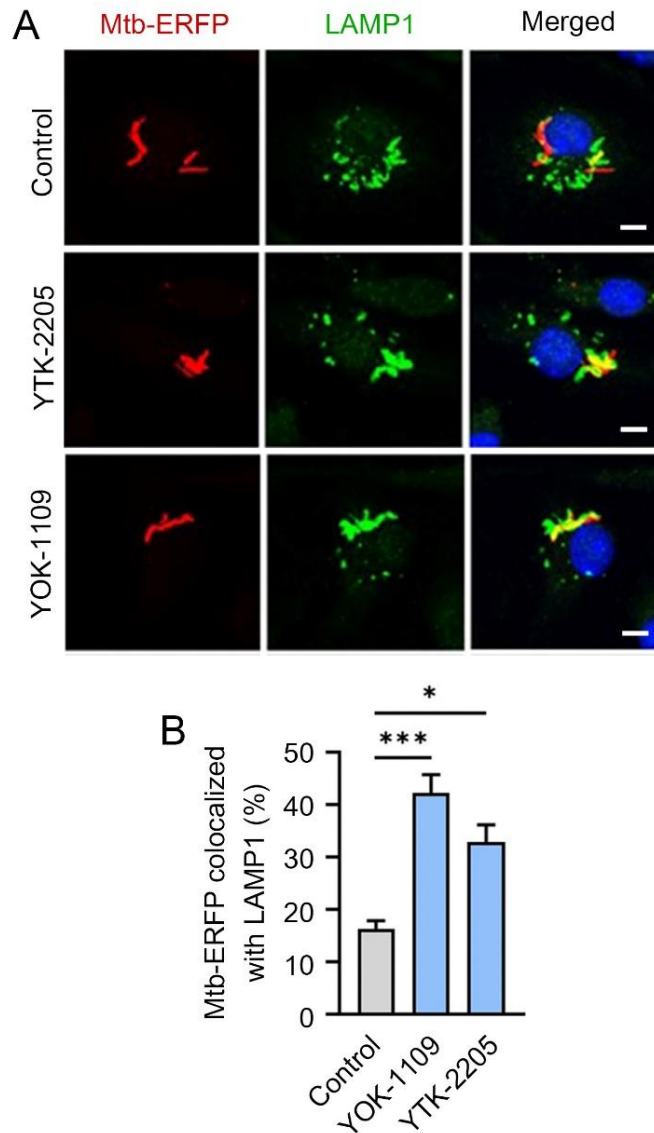


**Figure 44. p62 agonists increase lysosome targeted intracellular *M. tuberculosis*.**

(A) BMDMs were infected with Mtb-ERFP (MOI of 5) and treated with YTK-2205 (5  $\mu$ M) or YTK-A76 (5  $\mu$ M). Co-localization analysis of LAMP1 (green) and Mtb-ERFP by immunofluorescence analysis. Representative images. Scale bar, 5  $\mu$ m. (B) Quantitative data represents the average percentage of Mtb-ERFP colocalized with LAMP1 (n = 7).

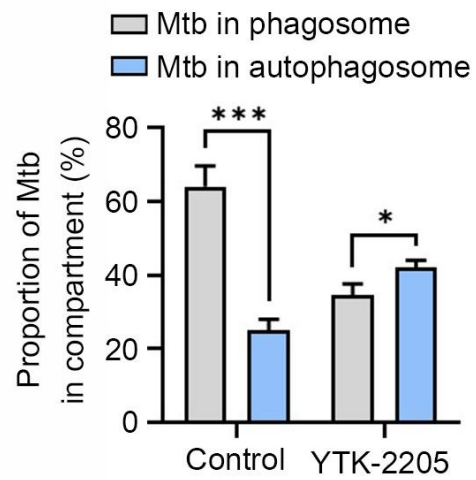
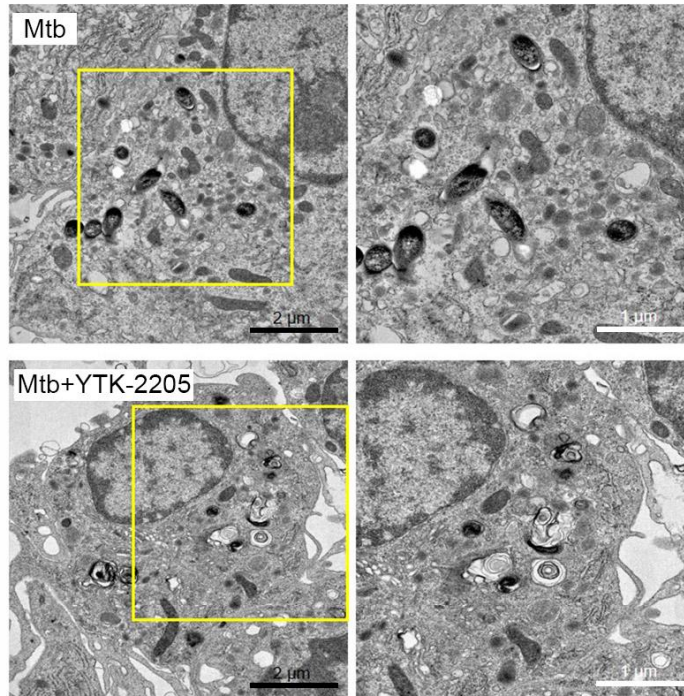


**Figure 45. p62 agonist YTK-2205 accelerates the targeting of intracellular *M. tuberculosis* to autophagosomes.**

(A) Representative TEM images of BMDMs treated with YTK-2205 (5  $\mu$ M) under uninfected or Mtb-infected conditions. Scale bars, 2  $\mu$ m and 1  $\mu$ m (left panel). (B) A quantitative graph represents the proportion of Mtb in the compartment of autophagosomes or phagosomes in BMDMs (right panel).

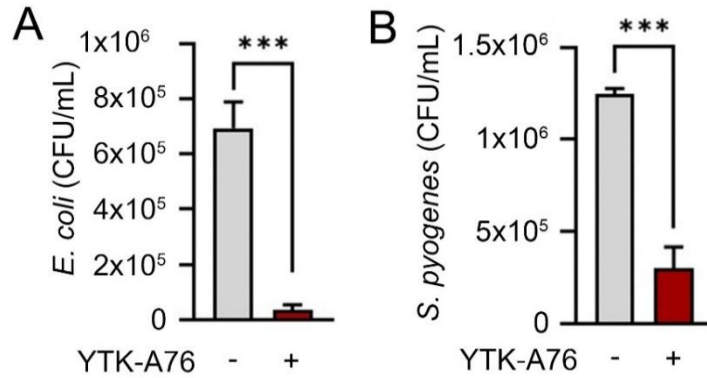


**Figure 46. Antimicrobial effect of YTK-A76 against intracellular *E. coli* and *S. pyogenes*.**

(A) RAW264.7 cells infected with *E. coli* for 30 min followed by incubation with p62 agonist at 10  $\mu$ M for 6 h. (B) J774A.1 infected with *S. pyogenes* and treated with p62 agonist at 10  $\mu$ M for 6 h. The number of intracellular bacteria was measured by a CFU assay.

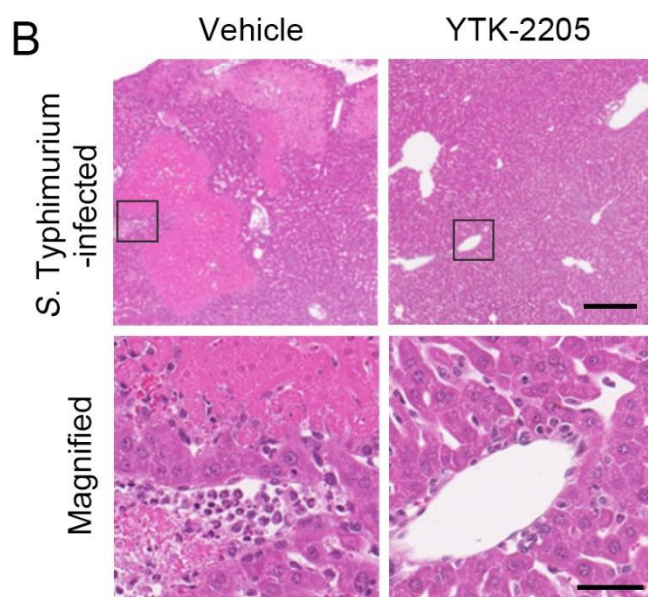
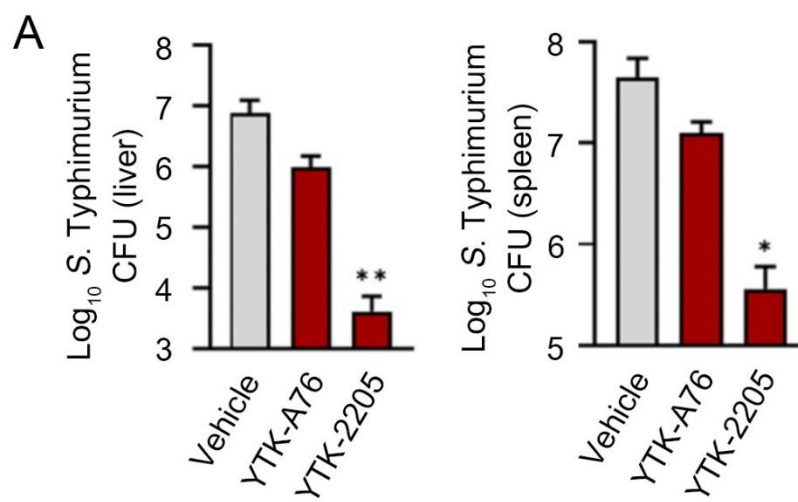


**Figure 47. p62 agonists reduce bacterial burden and inflammation in the liver and spleen of *S. Typhimurium*-infected mice.**

(A) Mice were injected p.o. with  $1 \times 10^6$  *S. Typhimurium* in PBS, followed by administration of p62 agonist (20 mg/kg) by i.p. once daily (n = 4 per group). Bacterial burdens in the liver (upper panel) and spleen (lower panel) were analyzed by CFU assay after 6 dpi. (B) Representative H&E staining images of liver from *S. Typhimurium* infection model injected i.p. with vehicle (Control) or 20 mg/kg YTK-2205.

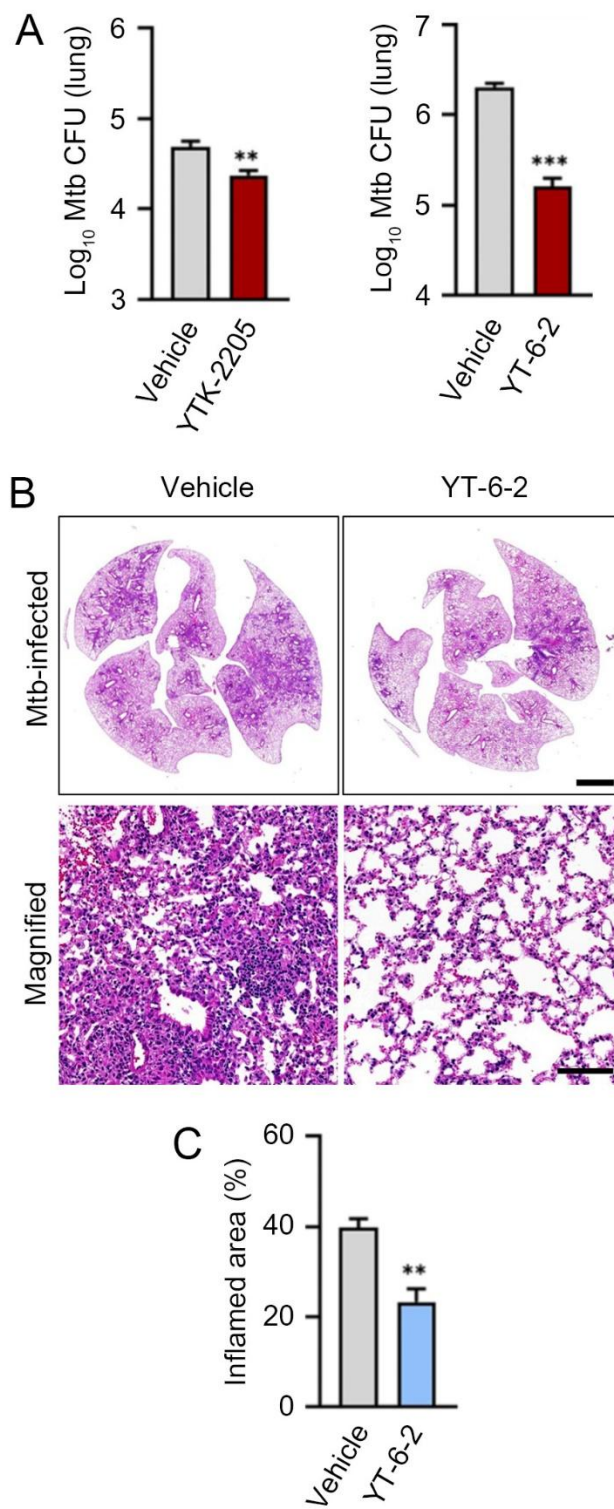


**Figure 48. p62 agonist YT-6-2 reduces bacterial burden and inflammation in lung of *M. tuberculosis*-infected mice.**

(A) Bacterial burdens in mouse lung tissues. Mice were infected i.n. with Mtb ( $5 \times 10^4$  CFU) intranasally. After infection, mice were treated with vehicle, YTK-2205 (i.p. 10 mg/kg; n = 7 per group, left), or YT-6-2 (i.p. 20 mg/kg; n = 5 per group, right). (B) Representative H&E-stained images in lung tissue of mice treated as in c. Scale bars: 2000  $\mu$ m and 100  $\mu$ m. (left panel). (C) A quantitative graph represents the average percentage of the inflamed area of the tissue section (right panel). (E and F) Mice (n = 4 per group) were infected i.n. with BCG ( $1 \times 10^7$  CFU), and treated with vehicle or YTK-2205 (i.p. 20 mg/kg) at 3-6 dpi.



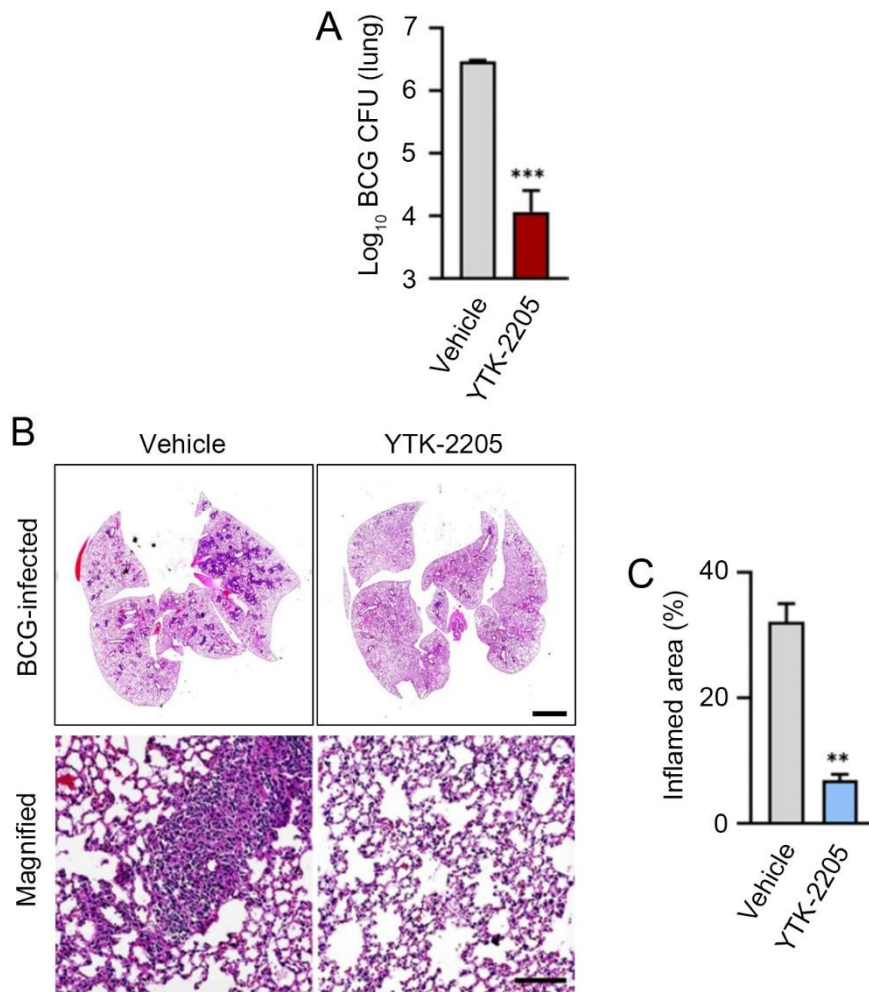


**Figure 49. YTK-2205 reduces bacterial burden and inflammation in the lung of BCG-infected mouse.**

(A) Bacterial loads determined by CFU analysis. (B) H&E staining of the BCG-infected lung tissue and representative images are shown. Scale bars, 2000  $\mu$ m, and 100  $\mu$ m. (C) A quantitative graph represents the average percentage of the inflamed area of tissue section.

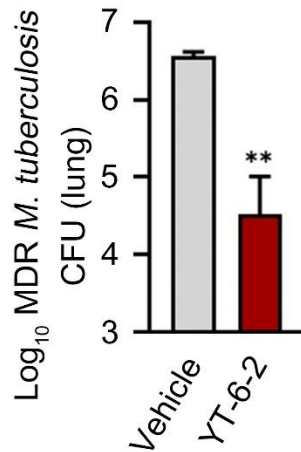


**Figure 50. YT-6-2 reduces bacterial burden in the lung of multidrug-resistant *M. tuberculosis*-infected mice.**

Bacterial loads in mouse lung tissues. Mice (n = 4 per group) were infected i.n. with MDR-Mtb ( $5 \times 10^3$  CFU) intranasally and treated with vehicle or YT-6-2 (i.p. 20 mg/kg).

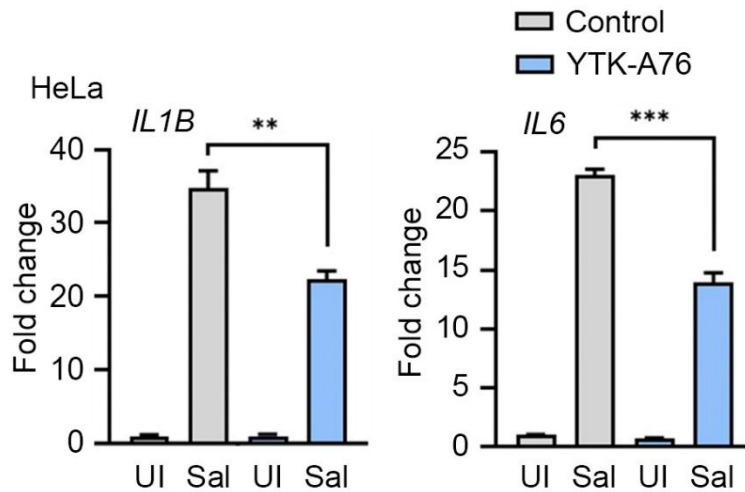


**Figure 51. YTK-A76 reduces mRNA expression of inflammatory cytokines that are induced by *S. Typhimurium* infection.**

Relative fold change in mRNA level of *IL1B* and *IL6* in HeLa cells treated with or without YTK-A76 under *S. Typhimurium* infection was analyzed by RT-qPCR.

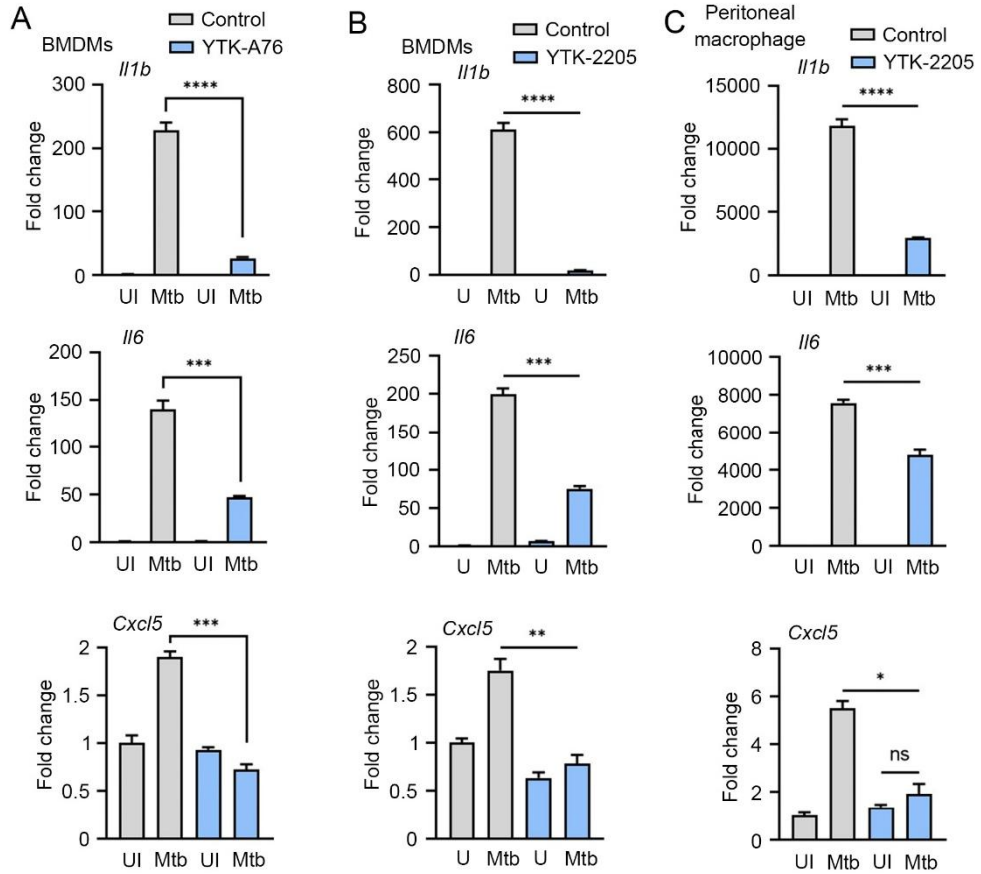


**Figure 52. p62 agonists reduce mRNA expression of inflammatory cytokines that are induced by *M. tuberculosis* infection.**

BMDMs (A) or PMs (B) were infected with Mtb (MOI of 5) and treated with YTK-A76 (5  $\mu$ M; A) or YTK-2205 (5  $\mu$ M; B) for 6 h. Relative fold change in mRNA level of *Il1b*, *Il6*, and *Cxcl5* was determined using qRT-PCR.

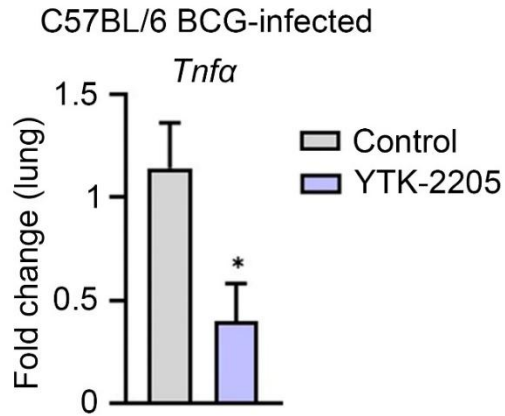


**Figure 53. YTK-2205 reduces inflammatory cytokine *Tnfa* in the lung of BCG-infected mice.**

Mice were infected i.n. with BCG ( $1 \times 10^7$  CFU) intranasally and treated with vehicle or YTK-2205 (i.p. 20 mg/kg) at 3-6 dpi. Relative fold change in mRNA level of *Tnfa* from lung tissues was measured by qRT-PCR. UI, uninfected.

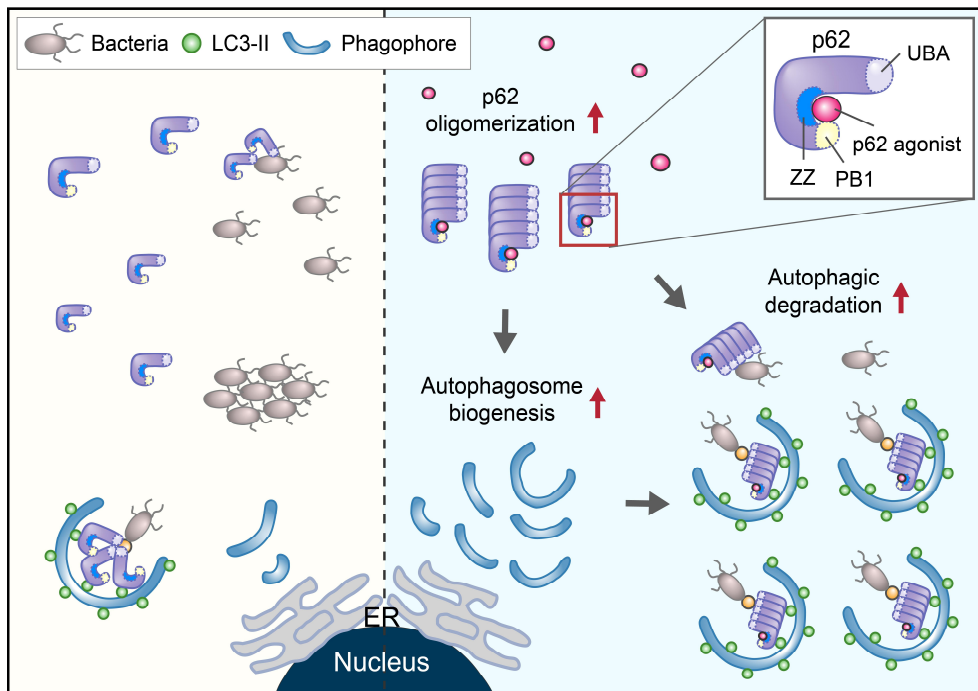


**Figure 54. Graphical overview of the activation of p62-mediated xenophagy by p62 agonists.**

## Discussion

In this thesis, I observed counteractive crosstalk between invading bacteria and selective autophagy. Upon bacterial infection, while mRNA and protein levels of autophagy receptors including p62 and Optineurin were upregulated, autophagosome biogenesis was downregulated. Consistently, the protein level of p62 increased in response to LPS treatment. In contrast to bacterial infection, LPS induced the expression of autophagy-related genes including WIPI1, UVRAG, MAP1LC3A, and DRAM1, and the protein level of p62. Furthermore, to boost up the selective autophagy against intracellular bacteria, I utilized Nt-Arg synthesized chemical mimetics. Upon bacterial infection, chemical mimetics of Nt-Arg that bind to the ZZ domain of p62 activated and induced self-oligomerization of the protein, and accelerated autophagosome biogenesis through the non-canonical autophagy pathway. Also, I demonstrate the antimicrobial effect of chemical p62 ligands by promoting the association of intracellular bacteria such as *S. Typhimurium* and *M. tuberculosis* with p62 and targeting the bacteria-associated p62 to autophagosomes.

Humans live in a symbiotic relationship with a variety of species, from multicellular organisms including animals and plants to unicellular organisms such as bacteria and fungi in various environments. Bacterial strains such as *Lactobacilli* and *Bifidobacteria* are known to provide health benefits, while *S. Typhimurium*, *E. coli* as well as *M. tuberculosis* have detrimental effects on the host [84, 85]. However,

any bacterium that invades the cell is detrimental rather than beneficial to the host. Cells recognize the surface of invading pathogens outside the cell through receptors, drag them into the cell in the form of phagosomes, and break them down directly in lysosomes. Also, bacteria-infected cells produce high reactive oxidants such as ROS and NO to incapacitate pathogens and make them die [9, 86]. In addition, pathogens exposed to the cytosol by directly infiltrating the cell or escaping the phagosome can be degraded by the autophagy-lysosomal pathway. Furthermore, cells suppress the growth of pathogens by sequestration of the bacteria with ions such as  $Zn^{2+}$ ,  $Cu^{2+}$ ,  $Fe^{2+}$ , and  $Fe^{3+}$  into specific compartments, and secretion of antimicrobial peptides to weaken the membrane integrity of pathogens and remove them [87]. Among these various antimicrobial mechanisms, autophagy is not a mechanism limited to immune cells, but a general degradation mechanism in all types of cells. Therefore, pathogen clearance through autophagy is a cellular self-defense system that occurs not only in immune cells but also in non-immune cells. Here, I show that intracellular bacteria can be eradicated by boosting the activity of selective autophagy in immune and non-immune cells.

Pathogens have evolved to gain unique strategies to evade the host defense system or even hijack the autophagy machinery to survive and proliferate within host cells [28]. However, exactly how the bacteria evade cellular host defense system have not been fully investigated. In this study, I found that p62 mostly participated in xenophagy compared to the other autophagy receptors. Upon *S. Typhimurium* infection, the mRNA expression and protein level of p62 increased and the protein was associated with the intracellular bacteria. Consistently, LPS induced an increase in the protein level of p62 and autophagosome biogenesis. These results indicate that



cells activate autophagy as a host defense system against foreign substances whereas intracellular bacteria inhibit autophagy to survive within cells. Furthermore, p62, LC3, and ATG5 knockdown cells were not able to inhibit the growth of intracellular *S. Typhimurium* indicating the importance of autophagy as a cellular host defense system.

As a host-directed therapeutic, I utilized chemical mimetics Nt-Arg that bind to the ZZ domain of p62 to promote selective autophagy against intracellular bacteria. The synthesized compounds exhibited an antimicrobial effect against *S. Typhimurium* through the ZZ domain of p62. The antimicrobial efficacy involved no detectible activity to directly kill bacteria, further supporting the selective role of p62-mediated autophagy in host innate immunity. p62, whose ZZ domain was occupied with compounds, required PB1 and UBA domains and ubiquitination of the intracellular bacteria to recognize the invading bacteria. Consistently, the p62 agonists facilitated the targeting of the intracellular bacteria-associated p62 to autophagosomes for lysosomal degradation. In contrast, well-known canonical autophagy inducer rapamycin did not promote the targeting of the intracellular bacteria to autophagosomes and had no antimicrobial effect. From these results, it was confirmed that the antimicrobial efficacy of the p62 agonists was due to the activation of mTOR independent xenophagy.

In addition, p62 agonists showed an antimicrobial effect against intracellular Mtb by enhancing the ability of host cells to recognize and target cytosolic Mtb to autophagic membranes via p62. Moreover, during bacterial infection, these xenophagy inducers did not activate inflammatory immune responses but suppressed several pro-inflammatory cytokines, such as IL1B/IL-1 $\beta$  and TNF/TNF- $\alpha$ . Such an

activity to downregulate proinflammatory responses may represent the function of selective autophagy as a regulator of excessive inflammatory responses. Importantly, I also found the antimicrobial effects of p62 agonists upon MDR-Mtb infection *in vivo*, highlighting the potential use of p62 agonists as host-directed therapeutics against drug-resistant TB. p62 agonists were effective against infection with BCG, which lacks genes encoding ESX-1 to promote cytosolic translocation and xenophagy [37, 87]. Although remaining question concerns whether p62 agonists facilitate the targeting of Mtb containing phagosome or cytosolic Mtb to autophagosome, the results of my study suggest that p62-dependent xenophagy may provide a therapeutic strategy for antibiotic-resistant bacteria.

One remaining question involves the molecular mechanism by which p62 is recruited to bacterial membranes. Previous studies show that p62 agonists facilitated the autophagic degradation of protein aggregates as well as the ER along with its luminal contents [77, 78], with differential preference and selectivity depending on the chemical structures. While further investigations are needed to correlate the chemical structures to the intramolecular conformational changes and the spatiotemporal arrangement of p62 associated with its cargoes, one could speculate that the oligomerization of p62 may be a common step for various cargo types. Nonetheless, it should be noted that where p62 oligomers, during aggrephagy, grow into large aggregates via uncontrolled formation of disulfide bond formation between p62 [77], p62 forms oligomers in an organized topology during the ER-phagy [78]. I, therefore, suggest that p62 during xenophagy is associated with an unknown receptor(s) on the bacterial membrane in a manner similar to that in the ER-phagy. The ubiquitin coat on *S. Typhimurium* that invade the cytosol is formed

through the ubiquitination of outer membrane proteins [88] or a non-proteinaceous substrate, the lipid A moiety of bacterial lipopolysaccharide (LPS) [89]. Therefore, the unknown receptor(s) on the bacterial membrane may not only be a ubiquitinated protein but also other ubiquitinated bacterial membrane components, and the screening of such bacterial receptors is underway.

To eradicate invading pathogens, several generations of antibiotics such as penicillins, cephalosporins, and fluoroquinolones have been developed [52, 53]. However, the fast-growing bacterial nature allowed the pathogens to evolve to gain resistance to the antibiotics and still threaten our lives. As multidrug-resistant pathogenic bacteria are rapidly rising, it is increasingly urgent to develop novel strategies fundamentally different from conventional antibiotics. Host-directed therapy aims to enhance host defense mechanisms or modulate excessive inflammation [57], such as autophagy. Several chemical modulators of autophagy have been used to induce targeted degradation of intracellular bacteria, including rapamycin, metformin, resveratrol, AR-12, and D61 [48, 90]. Despite rather extensive research on molecules confirmed to inhibit the growth of intracellular bacteria by activating autophagy, there are no generally applicable therapeutic molecules whose mode of action is clearly defined with satisfactory efficacy in various cell lines and *in vivo*. The results of my study shows that the chemical activation of p62-dependent selective autophagy is generally applicable to various bacterial strains. It should be noted that whereas the conventional antibiotics strictly depend on molecular interactions, the mode-of-action of p62-dependent xenophagy involves the recognition of (universally conserved) ubiquitin chains on bacterial membranes by p62, which in turn recruits autophagic membranes to the site of

degradation. Since p62 agonists do not exert an antimicrobial effect directly on the bacteria, there is a low possibility of the generation of resistant bacteria to the p62 agonists. Furthermore, in contrast to the conventional antibiotics, p62 agonists do not affect extracellular bacteria that are beneficial to the host, but only target the detrimental intracellular bacteria for degradation. Therefore, in principle, p62 may be a potential drug target in host-directed therapy against a broad range of multi-drug resistant bacteria.

## References

1. Levine B, Mizushima N, Virgin HW. Autophagy in immunity and inflammation. *Nature* 2011; 469:323-35.
2. Iwasaki A, Medzhitov R. Control of adaptive immunity by the innate immune system. *Nat Immunol* 2015; 16:343-53.
3. Iwasaki A, Medzhitov R. Regulation of adaptive immunity by the innate immune system. *Science* 2010; 327:291-5.
4. Hiam-Galvez KJ, Allen BM, Spitzer MH. Systemic immunity in cancer. *Nat Rev Cancer* 2021; 21:345-59.
5. Mihret A. The role of dendritic cells in *Mycobacterium tuberculosis* infection. *Virulence* 2012; 3:654-9.
6. Liu CH, Liu H, Ge B. Innate immunity in tuberculosis: host defense vs pathogen evasion. *Cell Mol Immunol* 2017; 14:963-75.
7. Zhu LL, Zhao XQ, Jiang C, *et al.* C-type lectin receptors Dectin-3 and Dectin-2 form a heterodimeric pattern-recognition receptor for host defense against fungal infection. *Immunity* 2013; 39:324-34.
8. Nau GJ, Richmond JF, Schlesinger A, *et al.* Human macrophage activation programs induced by bacterial pathogens. *Proc Natl Acad Sci U S A* 2002; 99:1503-8.
9. Weiss G, Schaible UE. Macrophage defense mechanisms against

intracellular bacteria. *Immunol Rev* 2015; 264:182-203.

10. Anding AL, Baehrecke EH. Cleaning House: Selective Autophagy of Organelles. *Dev Cell* 2017; 41:10-22.
11. Glick D, Barth S, Macleod KF. Autophagy: cellular and molecular mechanisms. *J Pathol* 2010; 221:3-12.
12. Bhattacharyya S, Yu H, Mim C, *et al.* Regulated protein turnover: snapshots of the proteasome in action. *Nat Rev Mol Cell Biol* 2014; 15:122-33.
13. Finley D. Recognition and processing of ubiquitin-protein conjugates by the proteasome. *Annu Rev Biochem* 2009; 78:477-513.
14. Rubinsztein DC. The roles of intracellular protein-degradation pathways in neurodegeneration. *Nature* 2006; 443:780-6.
15. Mizushima N. Autophagy: process and function. *Genes Dev* 2007; 21:2861-73.
16. Mizushima N, Komatsu M. Autophagy: renovation of cells and tissues. *Cell* 2011; 147:728-41.
17. Kaushik S, Cuervo AM. Chaperone-mediated autophagy: a unique way to enter the lysosome world. *Trends Cell Biol* 2012; 22:407-17.
18. Li WW, Li J, Bao JK. Microautophagy: lesser-known self-eating. *Cell Mol Life Sci* 2012; 69:1125-36.
19. Schmid D, Pypaert M, Munz C. Antigen-loading compartments for major histocompatibility complex class II molecules continuously receive input from autophagosomes. *Immunity* 2007; 26:79-92.
20. Mizushima N, Klionsky DJ. Protein turnover via autophagy: implications for metabolism. *Annu Rev Nutr* 2007; 27:19-40.

21. Zaffagnini G, Martens S. Mechanisms of Selective Autophagy. *J Mol Biol* 2016; 428:1714-24.
22. Gatica D, Lahiri V, Klionsky DJ. Cargo recognition and degradation by selective autophagy. *Nat Cell Biol* 2018; 20:233-42.
23. Ciuffa R, Lamark T, Tarafder AK, *et al.* The selective autophagy receptor p62 forms a flexible filamentous helical scaffold. *Cell Rep* 2015; 11:748-58.
24. Shaid S, Brandts CH, Serve H, *et al.* Ubiquitination and selective autophagy. *Cell Death Differ* 2013; 20:21-30.
25. Kraft C, Peter M, Hofmann K. Selective autophagy: ubiquitin-mediated recognition and beyond. *Nat Cell Biol* 2010; 12:836-41.
26. Birgisdottir AB, Lamark T, Johansen T. The LIR motif - crucial for selective autophagy. *J Cell Sci* 2013; 126:3237-47.
27. Levine B, Deretic V. Unveiling the roles of autophagy in innate and adaptive immunity. *Nat Rev Immunol* 2007; 7:767-77.
28. Sorbara MT, Girardin SE. Emerging themes in bacterial autophagy. *Curr Opin Microbiol* 2015; 23:163-70.
29. Pareja ME, Colombo MI. Autophagic clearance of bacterial pathogens: molecular recognition of intracellular microorganisms. *Front Cell Infect Microbiol* 2013; 3:54.
30. Ishimura R, Tanaka K, Komatsu M. Dissection of the role of p62/Sqstm1 in activation of Nrf2 during xenophagy. *FEBS Lett* 2014; 588:822-8.
31. Deretic V, Levine B. Autophagy, immunity, and microbial adaptations. *Cell Host Microbe* 2009; 5:527-49.
32. Vergne I, Singh S, Roberts E, *et al.* Autophagy in immune defense against

- Mycobacterium tuberculosis. Autophagy 2006; 2:175-8.
33. Cemma M, Kim PK, Brumell JH. The ubiquitin-binding adaptor proteins p62/p62 and NDP52 are recruited independently to bacteria-associated microdomains to target Salmonella to the autophagy pathway. Autophagy 2011; 7:341-5.
  34. Escoll P, Rolando M, Buchrieser C. Modulation of Host Autophagy during Bacterial Infection: Sabotaging Host Munitions for Pathogen Nutrition. Front Immunol 2016; 7:81.
  35. Xie Z, Zhang Y, Huang X. Evidence and speculation: the response of Salmonella confronted by autophagy in macrophages. Future Microbiol 2020; 15:1277-86.
  36. Ganesan R, Hos NJ, Gutierrez S, *et al.* Salmonella Typhimurium disrupts Sirt1/AMPK checkpoint control of mTOR to impair autophagy. PLoS Pathog 2017; 13:e1006227.
  37. Augenstreich J, Briken V. Host Cell Targets of Released Lipid and Secreted Protein Effectors of Mycobacterium tuberculosis. Front Cell Infect Microbiol 2020; 10:595029.
  38. Manzanillo PS, Ayres JS, Watson RO, *et al.* The ubiquitin ligase parkin mediates resistance to intracellular pathogens. Nature 2013; 501:512-6.
  39. Franco LH, Nair VR, Scharn CR, *et al.* The Ubiquitin Ligase Smurf1 Functions in Selective Autophagy of Mycobacterium tuberculosis and Anti-tuberculous Host Defense. Cell Host Microbe 2017; 22:421-3.
  40. Polajnar M, Dietz MS, Heilemann M, *et al.* Expanding the host cell ubiquitylation machinery targeting cytosolic Salmonella. EMBO Rep 2017;



18:1572-85.

41. Huett A, Heath RJ, Begun J, *et al.* The LRR and RING domain protein LRSAM1 is an E3 ligase crucial for ubiquitin-dependent autophagy of intracellular Salmonella Typhimurium. *Cell Host Microbe* 2012; 12:778-90.
42. Noad J, von der Malsburg A, Pathe C, *et al.* LUBAC-synthesized linear ubiquitin chains restrict cytosol-invading bacteria by activating autophagy and NF-kappaB. *Nat Microbiol* 2017; 2:17063.
43. Slowicka K, van Loo G. Optineurin Functions for Optimal Immunity. *Front Immunol* 2018; 9:769.
44. Wild P, Farhan H, McEwan DG, *et al.* Phosphorylation of the autophagy receptor Optineurin restricts Salmonella growth. *Science* 2011; 333:228-33.
45. Huang J, Brumell JH. Bacteria-autophagy interplay: a battle for survival. *Nat Rev Microbiol* 2014; 12:101-14.
46. Wu YW, Li F. Bacterial interaction with host autophagy. *Virulence* 2019; 10:352-62.
47. Xiong Q, Yang M, Li P, *et al.* Bacteria Exploit Autophagy For Their Own Benefit. *Infect Drug Resist* 2019; 12:3205-15.
48. Kimmey JM, Stallings CL. Bacterial Pathogens versus Autophagy: Implications for Therapeutic Interventions. *Trends Mol Med* 2016; 22:1060-76.
49. Feng ZZ, Jiang AJ, Mao AW, *et al.* The Salmonella effectors SseF and SseG inhibit Rab1A-mediated autophagy to facilitate intracellular bacterial survival and replication. *J Biol Chem* 2018; 293:9662-73.
50. Kim KH, An DR, Song J, *et al.* Mycobacterium tuberculosis Eis protein

- initiates suppression of host immune responses by acetylation of DUSP16/MKP-7. *Proc Natl Acad Sci U S A* 2012; 109:7729-34.
51. Puri RV, Reddy PV, Tyagi AK. Secreted acid phosphatase (SapM) of *Mycobacterium tuberculosis* is indispensable for arresting phagosomal maturation and growth of the pathogen in guinea pig tissues. *PLoS One* 2013; 8:e70514.
  52. Lopez Romo A, Quiros R. Appropriate use of antibiotics: an unmet need. *Ther Adv Urol* 2019; 11:1756287219832174.
  53. Fair RJ, Tor Y. Antibiotics and bacterial resistance in the 21st century. *Perspect Medicin Chem* 2014; 6:25-64.
  54. Aslam B, Wang W, Arshad MI, *et al.* Antibiotic resistance: a rundown of a global crisis. *Infect Drug Resist* 2018; 11:1645-58.
  55. Fauconnier A, Nagel TE, Fauconnier C, *et al.* The Unique Role That WHO Could Play in Implementing Phage Therapy to Combat the Global Antibiotic Resistance Crisis. *Front Microbiol* 2020; 11:1982.
  56. Mendelson M. Practical solutions to the antibiotic resistance crisis. *S Afr Med J* 2015; 105:413.
  57. Kaufmann SHE, Dorhoi A, Hotchkiss RS, *et al.* Host-directed therapies for bacterial and viral infections. *Nat Rev Drug Discov* 2018; 17:35-56.
  58. Tobin DM. Host-Directed Therapies for Tuberculosis. *Csh Perspect Med* 2015; 5.
  59. Andersson AM, Andersson B, Lorell C, *et al.* Autophagy induction targeting mTORC1 enhances *Mycobacterium tuberculosis* replication in HIV co-infected human macrophages. *Sci Rep* 2016; 6:28171.

60. Zullo AJ, Jurcic Smith KL, Lee S. Mammalian target of Rapamycin inhibition and mycobacterial survival are uncoupled in murine macrophages. *BMC Biochem* 2014; 15:4.
61. Singhal A, Jie L, Kumar P, *et al.* Metformin as adjunct antituberculosis therapy. *Sci Transl Med* 2014; 6:263ra159.
62. Yang CS, Kim JJ, Lee HM, *et al.* The AMPK-PPARGC1A pathway is required for antimicrobial host defense through activation of autophagy. *Autophagy* 2014; 10:785-802.
63. Cheng CY, Gutierrez NM, Marzuki MB, *et al.* Host sirtuin 1 regulates mycobacterial immunopathogenesis and represents a therapeutic target against tuberculosis. *Sci Immunol* 2017; 2.
64. Chiu HC, Kulp SK, Soni S, *et al.* Eradication of intracellular *Salmonella enterica* serovar Typhimurium with a small-molecule, host cell-directed agent. *Antimicrob Agents Chemother* 2009; 53:5236-44.
65. Nagy TA, Quintana JLJ, Reens AL, *et al.* Autophagy Induction by a Small Molecule Inhibits *Salmonella* Survival in Macrophages and Mice. *Antimicrob Agents Chemother* 2019.
66. Tasaki T, Sriram SM, Park KS, *et al.* The N-end rule pathway. *Annu Rev Biochem* 2012; 81:261-89.
67. Varshavsky A. N-degron and C-degron pathways of protein degradation. *Proc Natl Acad Sci U S A* 2019; 116:358-66.
68. Kwon YT, Kashina AS, Davydov IV, *et al.* An essential role of N-terminal arginylation in cardiovascular development. *Science* 2002; 297:96-9.
69. Sriram SM, Kwon YT. The molecular principles of N-end rule recognition.

Nat Struct Mol Biol 2010; 17:1164-5.

70. Finley D, Chen X, Walters KJ. Gates, Channels, and Switches: Elements of the Proteasome Machine. Trends Biochem Sci 2016; 41:77-93.
71. Lee MJ, Tasaki T, Moroi K, *et al.* RGS4 and RGS5 are in vivo substrates of the N-end rule pathway. Proc Natl Acad Sci U S A 2005; 102:15030-5.
72. Ditzel M, Wilson R, Tenev T, *et al.* Degradation of DIAP1 by the N-end rule pathway is essential for regulating apoptosis. Nat Cell Biol 2003; 5:467-73.
73. Rao H, Uhlmann F, Nasmyth K, *et al.* Degradation of a cohesin subunit by the N-end rule pathway is essential for chromosome stability. Nature 2001; 410:955-9.
74. Hu RG, Sheng J, Qi X, *et al.* The N-end rule pathway as a nitric oxide sensor controlling the levels of multiple regulators. Nature 2005; 437:981-6.
75. Yoo YD, Mun SR, Ji CH, *et al.* N-terminal arginylation generates a bimodal degron that modulates autophagic proteolysis. Proc Natl Acad Sci U S A 2018; 115:E2716-E24.
76. Cha-Molstad H, Sung KS, Hwang J, *et al.* Amino-terminal arginylation targets endoplasmic reticulum chaperone BiP for autophagy through p62 binding. Nat Cell Biol 2015; 17:917-29.
77. Cha-Molstad H, Yu JE, Feng Z, *et al.* p62/p62/Sequestosome-1 is an N-recognin of the N-end rule pathway which modulates autophagosome biogenesis. Nat Commun 2017; 8:102.
78. Ji CH, Kim HY, Heo AJ, *et al.* The N-Degron Pathway Mediates ER-phagy. Mol Cell 2019; 75:1058-72 e9.
79. Birmingham CL, Smith AC, Bakowski MA, *et al.* Autophagy controls

- Salmonella infection in response to damage to the Salmonella-containing vacuole. *J Biol Chem* 2006; 281:11374-83.
80. Rangaraju S, Verrier JD, Madorsky I, *et al.* Rapamycin activates autophagy and improves myelination in explant cultures from neuropathic mice. *J Neurosci* 2010; 30:11388-97.
  81. Rubinsztein DC, Nixon RA. Rapamycin induces autophagic flux in neurons. *Proc Natl Acad Sci U S A* 2010; 107:E181; author reply E2.
  82. Mayer-Barber KD, Barber DL. Innate and Adaptive Cellular Immune Responses to Mycobacterium tuberculosis Infection. *Cold Spring Harb Perspect Med* 2015; 5.
  83. Yoshikai Y. Immunological protection against mycobacterium tuberculosis infection. *Crit Rev Immunol* 2006; 26:515-26.
  84. Smith I. Mycobacterium tuberculosis pathogenesis and molecular determinants of virulence. *Clin Microbiol Rev* 2003; 16:463-96.
  85. Deriu E, Liu JZ, Pezeshki M, *et al.* Probiotic bacteria reduce salmonella typhimurium intestinal colonization by competing for iron. *Cell Host Microbe* 2013; 14:26-37.
  86. Paiva CN, Bozza MT. Are reactive oxygen species always detrimental to pathogens? *Antioxid Redox Signal* 2014; 20:1000-37.
  87. Mahairas GG, Sabo PJ, Hickey MJ, *et al.* Molecular analysis of genetic differences between Mycobacterium bovis BCG and virulent M. bovis. *J Bacteriol* 1996; 178:1274-82.
  88. Fiskin E, Bionda T, Dikic I, *et al.* Global Analysis of Host and Bacterial Ubiquitinome in Response to Salmonella Typhimurium Infection. *Mol Cell*

2016; 62:967-981.

89. Otten EG, Werner E, Crespillo-Casado A, *et al.* Ubiquitylation of lipopolysaccharide by RNF213 during bacterial infection. *Nature* 2021; 594:111-116.
90. Wu S, Shen Y, Zhang S, *et al.* Salmonella Interacts With Autophagy to Offense or Defense. *Front Microbiol* 2020; 11:721.

## 국문초록

# N-데그론 경로가 세포 내 세균에 대한 선택적 자가포식에서 작용하는 기전 및 생화학적 조절

서울대학교 대학원

의과학과 의과학 전공

이 윤 지

대자가포식(이하 자가포식)은 다양한 스트레스에 반응하는 세포 내 숙주 방어 시스템이다. 박테리아 감염 시, 세포는 병원체 관련 분자 패턴(PAMP)을 통하여 수용체 단백질에 의해 박테리아를 인식하고 신호 전달 캐스케이드를 통해 선택적 자가포식을 활성화한다. 세포 내 일부 박테리아는 그들의 고유한 전략으로 숙주의 메커니즘을 조종하여 자가포식 분해 경로를 탈출한다. 광범위한 연구가 진행되었음에도 박테리아가 자가포식을 회피하는 방법에 대한 구체적인 메커니즘은 완전히 해명되지 않았다. 또한, 세포 내 세균에 대한 선택적 자가포식

조절을 통하여 약리학적으로 만족스러운 항균 효과를 나타내는 분자는 충분히 조사되지 않았다.

본 논문은 세포 내 박테리아와 숙주 자가포식 사이의 상호작용과 박테리아 감염 시 선택적 자가포식에서 아르기닌/N-데그론 경로의 생화학적 조절을 통한 항균 효능에 대하여 기술하였다. 숙주세포와 박테리아간의 Counteractive crosstalk 동안 p62/SQSTM1 (Sequestosome 1) 및 Optineurin 을 포함한 자가포식 수용체의 발현이 증가했으며 p62 은 세포 내 살모넬라균과 함께 자가포식소체로 표적 되었다. 세포 내 박테리아의 표적 분해를 촉진하기 위한 숙주 지향적 치료제로 p62 의 ZZ 도메인에 결합하는 Nt-아르기닌의 화학적 모방 체들을 활용하였다. p62 리간드는 p62 을 활성화하여 세포 내 살모넬라균에 의해 착취 및 억제되었던 자가포식소체의 생합성을 촉진하였다. 또한, p62 리간드는 mTOR 를 매개하는 자가포식 경로와는 독립적인 선택적 자가포식을 통해 살모넬라균, 대장균, 연쇄상 구균 및 결핵균(Mtb)과 같은 세포 내 박테리아에 대해 항균 효과를 나타내었다. 화합물들은 앞선 효능과 일관되게 감염 마우스 모델에서도 살모넬라균, BCG(Bacillus Calmette-Guérin), 결핵균 및 다제내성 결핵균에 대해 항균 효능을 보였고 염증성 사이토카인 생성을 억제하였다. 제노파지와 염증에서의 이중 작용은 실험한 모든 박테리아 균주에 의해 유발된 폐 또는 다른 조직의 염증성 병변으로부터 마우스를 상당히 보호하였다. 따라서 본 연구는 아르기닌/N-데그론 경로가 p62 를 매개하는 제노파지를 통하여 다양한 박테리아에



대한 선천 면역 반응에서 중추적인 역할을 함을 시사하고, 이 기전은 다제내성균을 포함하여 광범위한 병원체에 의해 유발되는 감염성 질환에 대한 새로운 치료 표적을 제공한다.

\* 본 연구는 “Chemical modulation of SQSTM1/p62-mediated xenophagy that targets a broad range of pathogenic bacteria. *Autophagy*, 2022.”에 게재되었다.

-----

**주요어** : 아르기닌/N-데그론 경로, 숙주 유도 요법, 염증, 선천 면역 반응, 선택적 자가포식, 살모넬라균, 결핵균, 제노파지.

**학 번** : 2014-21995